



POLITECNICO
MILANO 1863

SCUOLA DI INGEGNERIA INDUSTRIALE
E DELL'INFORMAZIONE

Design of a lattice-based cooling jacket for electric in-wheel motors manufactured by Laser Powder Bed Fusion

TESI DI LAUREA MAGISTRALE IN
MECHANICAL ENGINEERING - INGEGNERIA MECCANICA

Author: **Lorenzo Serventi**

Student ID: 951252

Advisor: Prof. Stefano Foletti

Co-advisors: Prof. Ali Gökhan Demir

Academic Year: 2021-2022

Abstract

This thesis work studies the application of strut-based lattice structures to enhance the thermo-hydraulic performances of a cooling jacket for electric in-wheel motors previously designed by Politecnico di Milano Dynamis team. A cooling jacket is a component of the cooling system dedicated to dissipate the thermal power produced by the motor. The main design areas of the component are the internal channel that guides a liquid coolant directly in touch with the motor and the external fin arrangement that dissipates heat to the environment. Different types, arrangements and dimensions of lattice structures have been embedded to the starting cooling jacket to increase its performances. The evaluated structures have been spherical dimples and tetrahedral cells for the internal channel and tetrahedral, octet and diamond cells for the external fin geometry. The different proposed configurations have been evaluated and compared through Computational Fluid Dynamic (CFD) analyses. Final results have been compared to those of Dynamis team. Mayor advantages have been found on the external fin arrangement. By applying lattice structure and a diverting wing it is possible to convey the air flow on the rear part of the component, enhancing heat exchange effectiveness and strongly reduce total weight. The component is designed following manufacturability constraints given by Laser Powder Bed Fusion process. Samples regarding the diamond lattice structure external geometry have been modelled to understand the component processability.

Keywords: cooling jacket, lattice structure, LPBF

Abstract in lingua italiana

Questo lavoro di tesi studia l'applicazione di strutture reticolari ad una camicia di raffreddamento per motori elettrici in-wheel, precedentemente progettata dal team Dynamis del Politecnico di Milano, per migliorarne le prestazioni termo-idrauliche. Una camicia di raffreddamento è un componente del sistema di raffreddamento dedicato a dissipare la potenza termica prodotta dal motore. Le principali aree di progettazione del componente sono il canale interno che guida un liquido refrigerante direttamente a contatto con il motore e l'alettatura esterna che dissipa il calore all'ambiente. Diversi tipi, disposizioni e dimensioni di strutture reticolari sono state incorporate alla camicia di raffreddamento di partenza per aumentarne le prestazioni. Le strutture valutate sono state: dimples sferici e celle tetraedriche per il canale interno e celle tetraedriche, octet e diamond per la geometria dell'alettatura esterna. Le diverse configurazioni proposte sono state valutate e confrontate attraverso analisi CFD (Computational Fluid Dynamic). I risultati finali sono stati confrontati con quelli del team Dynamis. I vantaggi maggiori sono stati riscontrati nella alettatura esterna. Applicando la struttura reticolare e un'ala deviatrice è possibile convogliare il flusso d'aria nella parte posteriore del componente, migliorando l'efficacia dello scambio termico e riducendone il peso totale. Il componente è progettato seguendo i vincoli di fabbricazione imposti dal processo di Laser Powder Bed Fusion (LPBF). Campioni riguardanti la geometria esterna con struttura diamond sono stati modellati per capire la fattibilità del componente.

Keywords: camicia di raffreddamento, strutture reticolari, LPBF

Contents

Abstract	i
Abstract in lingua italiana	iii
Contents	v
Introduction	1
1 State of the art	5
1.1 Classification of cooling jackets	6
1.2 Laser Powder Bed Fusion	7
1.2.1 Process	7
1.2.2 LPBF geometric defects	10
1.2.3 Mechanical properties of Aluminium alloy manufactured by LPBF .	14
1.3 Heat exchangers and Additive Manufacturing	15
1.4 Strut-based lattice structures in heat transfer applications	17
2 Cooling Jacketed Design - Introduction	23
3 Internal geometry design	25
3.1 Introduction	25
3.2 Numerical model	25
3.3 Planar sector assumption	28
3.4 Influence of channel thickness on empty channel	30
3.5 Implementation of enhancing techniques for the internal channel	31
3.5.1 Spherical dimples	32
Effect of dimple arrangement	33
Effect of dimple dimension	33
Comparison with empty channel	36
3.5.2 Tetrahedral cells	38

3 mm high cells in 3 rows	41
3 mm high cells in 6 rows	43
2 mm high cells in 6 rows	45
3.6 Final comparison	47
3.7 Re-design for LPBF	48
4 External geometry design	51
4.1 Introduction	51
4.2 Numerical model	51
4.3 Jacket with no external fins	54
4.4 Implementation of enhancing techniques for the external geometry	56
4.4.1 Tetrahedral cells	57
CFD analyses of entire model	57
Comparison with Dynamis results	58
Fluid mechanic analysis	60
4.4.2 Octet cells	64
Geometry definition	65
Planar sector comparison with tetrahedral cells	65
Axial sector comparison with tetrahedral cells	68
4.4.3 Diamond cells	71
Geometry definition	71
Planar sectors simulations	72
Results discussion and final comparison	74
4.5 Re-design for LPBF	75
4.6 Final component	78
5 LPBF samples design	83
5.1 Process parameters	85
6 Conclusions and future developments	87
Bibliography	89
List of Figures	93
List of Tables	97
Acknowledgements	99

Introduction

This thesis project was born from the desire to explore and develop an activity related to the Motorsport world. Politecnico di Milano participates in many student competitions, both in motorcycle and racing car fields. The Dynamis PRC team is the racing car division of the Politecnico of Milano. The team competes in a specific championship called Formula SAE, alongside with universities from all over the world. Formula SAE is an international car design competition where students are challenged to design and build winning racing car prototypes, powered by combustion engines or electric motors. The evaluation of the whole project does not consider only track performance, but also design quality and innovation. In 2019 – 2020 season, Dynamis team decided to leave the competition dedicated to internal combustion engine vehicles and begin the development of its first electric vehicle. The team decided to adopt four different electric motors placed outside the car body, directly placed on the wheel hubs. This configuration, known as in-wheel motors, is beneficial for acceleration, efficiency and drivability of the vehicle compared to a single motor placed in the car body. However, due to possible interference with suspension elements, this solution suffers from space limitation and challenging thermal management. Motor cooling is crucial to maintain high efficiency and to avoid problems as rotor demagnetization. The cooling system component in charge to keep the motor in optimal working conditions is an external cooling jacket placed around each motor, which is the main focus of this thesis work. This project in fact tries to further develop the design of this specific component for the Dynamis racing car. The cooling jacket envelops a single electric motor and favours the transfer of heat from the electric motor itself to a fluid, which is then sent and cooled in a liquid – air radiator and back to a pump placed on the car body. The coolant fluid is pumped back to the jacket and flows in the gap between the external surface of the motor and the internal surface of the cooling jacket itself. Moreover, this component can also reject thermal power to the surrounding environment due to the interaction with the external air stream. This further heat dissipation will help keeping the internal fluid cooler, improving heat transfer from the motor and relieving workload from liquid - air radiator. A proper external fin arrangement can be designed to improve this additional thermal exchange. Due to space limitation, the

design of this component is still a challenge and offers different possibilities to further developments. During the 2019-2020 season, Dynamis team decided to take advantage of the intrinsic versatility of Laser Powder Bed Fusion (LPBF) manufacturing technique to design its complex cooling jackets. In this technique, a high power laser selectively melts small metal particles into a 3-dimensional shape. LPBF recreates a part layer by layer along a growth direction. Aluminium powder is usually used for this component due to its high heat conduction capabilities and its good mechanical properties.



Figure 1: Dynamis cooling jacket for season 2019-2020 mounted on front left motor.

In a previous thesis work on this component [1], an innovative water jacket optimized for the LPBF process was presented. It studied and implemented an emerging solution in heat exchangers produced by LPBF, the gyroid structure. It is a particular kind of Triply Periodic Minimal Surface structures. It divides the volume in two separated regions maximizing the interaction surface and thus heat transfer. Its geometrical complexity requires additive manufacturing techniques such as LPBF. An example of the gyroid structure developed in the thesis is reported in Figure 2a. In this particular application, cold water enters on the top of the cooling jacket, uniformly distributed along the axial direction. The TPMS structure is placed all around the electric motor, filling the blue volume in Figure 2b, and guides water around it. Water runs in both separated domains of the gyroid structure while it absorbs heat from the motor. Heated water is collected on

the bottom of the cooling jacket and sent to the water – air radiator to be cooled down before re-entering the cooling jacket.

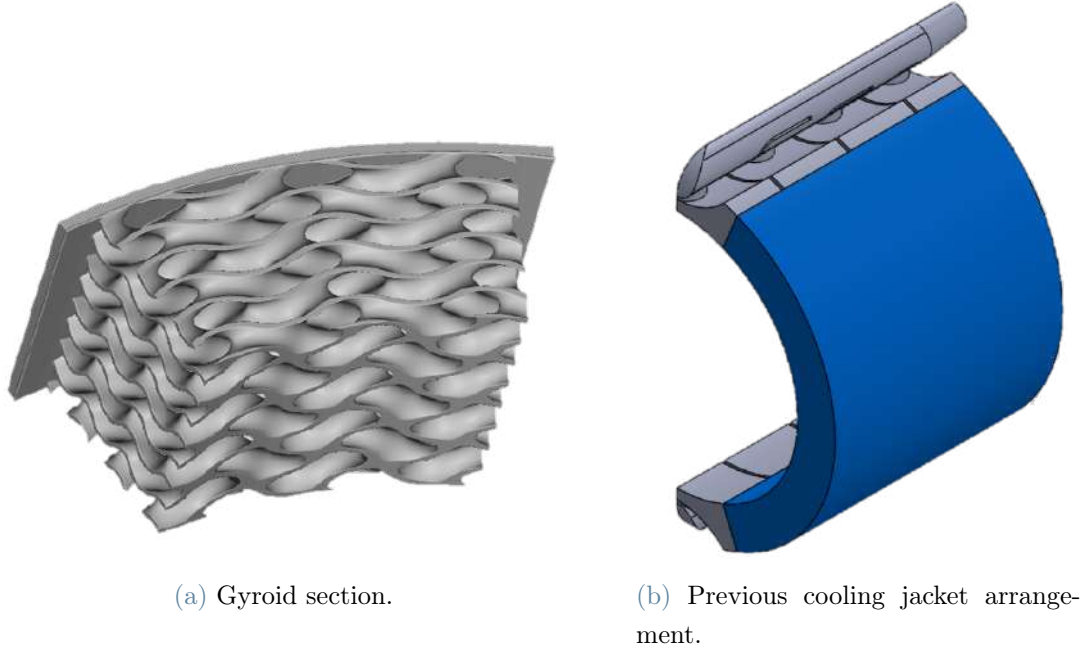


Figure 2: Previous thesis gyroid solution [1].

This solution was assessed with Computational Fluid Dynamics (CFD) analysis and compared to Dynamis' solution in terms of heat exchange and pressure loss of the fluid flowing in the jacket. It turned out that the gyroid solution, mainly due to much lower water velocity with respect to Dynamis one at the same flow rate, has much better performances in terms of pressure loss, but the motor surface temperature was generally higher. Since the surface temperature is a determinant factor for the electric motor performance and safety conditions, this solution required further developments and was not adopted by the team.

This thesis project aims at improving the cooling jacket design taking advantage of LPBF potentiality to increase the overall performances. Different kind of heat transfer enhancement techniques for heat exchangers applications have been studied in literature and applied in the cooling jacket. Both the internal water channel and the external structure interacting with ambient air have been analysed. CFD studies have been carried out to assess fluid dynamic performances of the component. This kind of analyses are time consuming and suffer from available computational capability, but can lead to quite accurate results. The proposed solution is then compared to the Dynamis current component to

understand possible advantages of adopting such technologies in cooling jacket application. Nonetheless, the LPBF fabrication of the cooling jacket must be assessed in terms of alloy and lattice structures processability. Manufacturability constraint of LPBF process are explained and considered during design stage.

1 | State of the art

The cooling jacket is a fundamental element when dealing with high power electric motors. During intense use, these motors can reach high temperatures, leading to loss of efficiency and even de-magnetization. Motors need then to be cooled down to operate in optimal conditions. The cooling jacket helps to achieve the goal. This component is applied externally around the in-wheel motor to contain and guide a forced flow of cooling liquid, which removes heat from motor surface. Thanks to gaskets, it is possible to run a coolant fluid in the free space left between the motor and the cooling jacket itself. The refrigerant fluid forced flow allows to remove the heat produced by the motor and transfer it to ambient air through a water – air radiator. A pump is responsible for the fluid circulation in the cooling system. A schematic representation of the cooling circuit is reported in Figure 1.1, where blue arrows represent cold water flows and red arrows represent hot water flows.

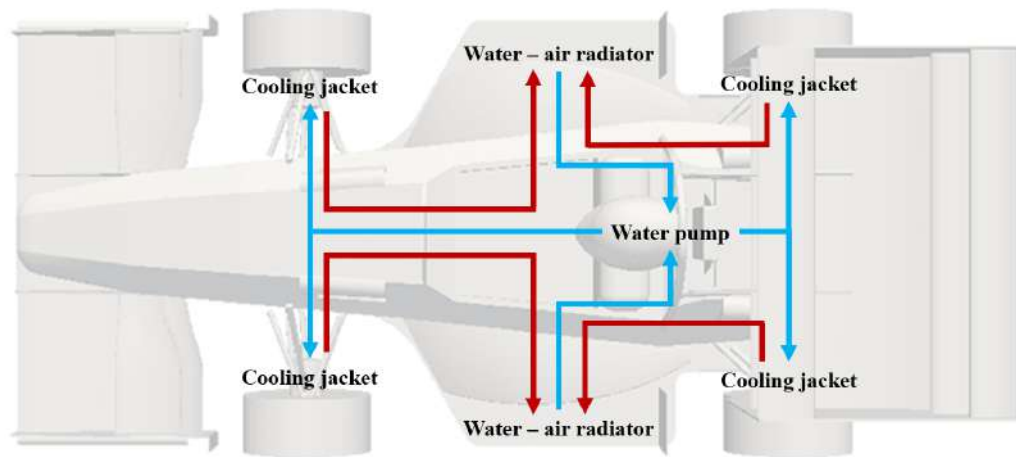


Figure 1.1: Schematic representation of cooling circuit.

The performances of a cooling jacket are mainly expressed by its pressure loss and the heat transfer capability. Pressure loss can be qualitatively seen as the resistance that the fluid encounters while flowing through the jacket. The more the fluid is obstructed or is subjected to quick changes in direction, the higher the pressure losses. The higher flow

resistance, the higher is the pumping force needed to push the water through the heat exchanger. Higher power would be absorbed by the pump, reducing the electric power that can be delivered to the motors. On the other hand, fluid direction change and mixing are beneficial for heat transfer, as will be explained in section 1.4. An efficient design must consider both these performance indicators and balance their effects.

1.1. Classification of cooling jackets

This cooling technique involving forced fluid flow around the motor is called liquid cooling and it is the most used for in-wheel motors cooling [2]. In literature it is possible to find various jacket designs that adopt this technique that can be classified according to the internal channel geometry [3]. One possible classification considers how fluid flows around the motor in relation to motor axial direction. Jacket flow can be circumferential or axial, as reported in Figure 1.2.

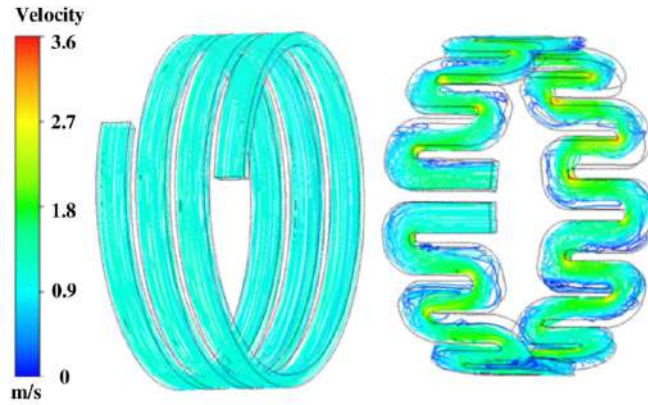


Figure 1.2: Velocity streamlines of the circumferential (left) and axial (right) water jackets [3].

The circumferential configuration, also called helical, results to be very efficient from the pressure losses point of view since it does not excessively disturb the flow, while the axial one is better for the thermal aspect due to the increase of flow turbulence. In general, the most adopted solution is the helical one as it offers a good performance compromise between heat removal capability and pressure drop. This thesis will exploit this configuration and try to improve its performances.

Cooling jackets can also be divided in double shell and single shell. Double concentric shell configuration means that the cooling liquid flows between an inner and an outer shell. The inner shell is in direct contact with the motor, separating the cooling liquid

from it. Despite the prevention of any fluid leakage, this solution will increase dimensions and weight of the cooling jacket. Instead, in the single shell jacket solution the motor surface is directly in contact with the coolant flow. This solution eliminates the conduction resistance through an inner shell and saves weight. However, gaskets are required between the jacket and the motor to keep the coolant sealed. Due to lightweight and direct contact of fluid with the motor, the single shell solution is the one developed in this project.

1.2. Laser Powder Bed Fusion

1.2.1. Process

The term Additive Manufacturing (AM) indicates the manufacturing technologies that are able to directly produce a three-dimensional object starting from its CAD model. AM allows the production of lightweight structures with complex geometries, unachievable by traditional manufacturing methods [4]. Laser Powder Bed Fusion (LPBF) technology starts from a 3D CAD representation of the desired part, divides it into layers and sends the file to the machine. LPBF machine uses a laser source and a scanning head to selectively melt the metal powder for the current layer geometry, fusing it with the layer below. The new melted layer rapidly cools down and solidifies. After a layer has been totally scanned, the build platform is then lowered by one layer thickness and a roller redistributes a thin layer of new powder on the partially built object. The cycle repeats with the scanning laser melting the new layer of powder. Each laser cycle produces a new subsequent slice of the object. The old and new layers are fused together during the process until the product growth is completed. The final part then consists of a sequence of melted and bonded metal layers. The process is shown in Figure 1.3. The excess recyclable metal powder is then removed and the object is de-tatched from the build platform.

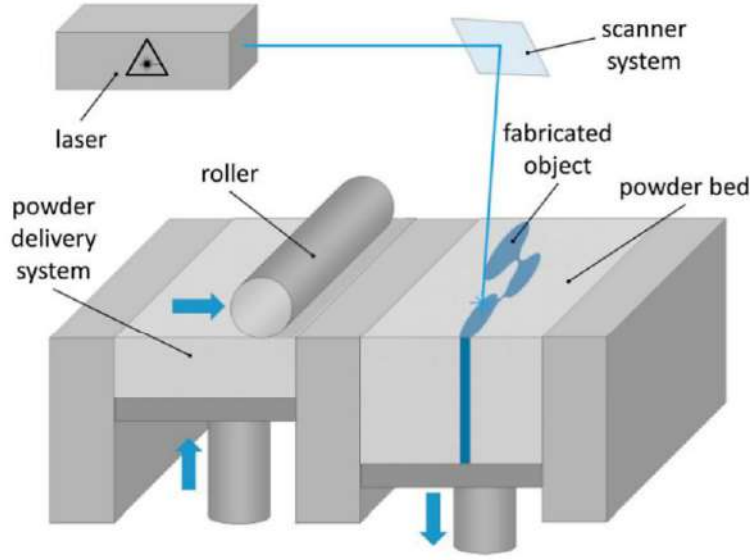


Figure 1.3: LPBF process [5].

The powder can be pre-heated by infrared or by heating the build platform to reduce the thermal shock during fusion and solidification and thus reducing residual stresses and thermal distortion of the part. To limit the interaction and contamination with oxygen, the entire process takes place in a closed chamber filled with an inert gas like N₂ or Ar. The chamber is also subjected to over pressure conditions to minimize the entry of ambient air during the process [6].

Some of the main process parameters are laser power and scan speed, dimension of focal spot, hatch distance and overlaps, layer thickness and powder dimension. The combination of laser power and laser speed will highly affect the final quality of the part since they determine the amount of melted material per cycle. A low power laser with high scanning speed will generate a weak component, with partial fusion of the desired material. On the other hand, a high power laser with low scanning speed will determine an abundance of molten material and excessive undesired particle adhesion [7]. An example of these two opposite conditions on a lattice structure part is reported in Figure 1.4.

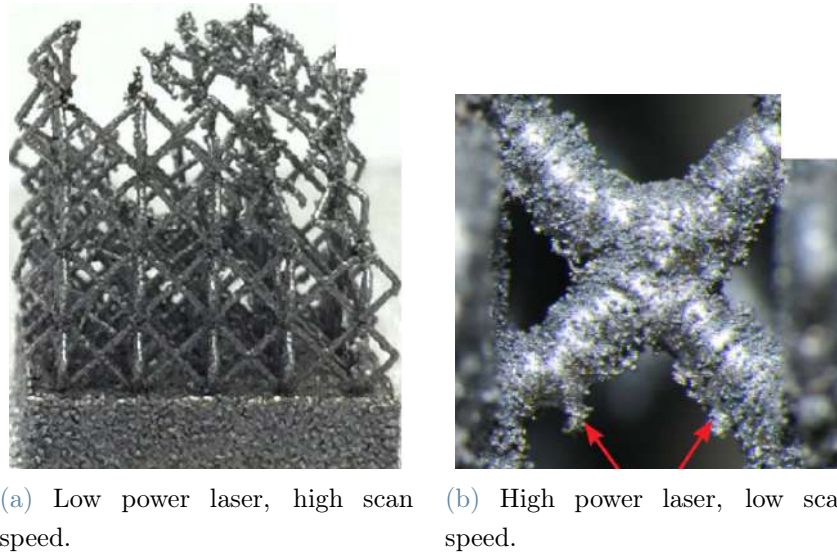


Figure 1.4: Effect of laser power and scan speed on lattice structure [7].

The dimension of the laser focal spot on the powder bed is usually in the range of 10 - 100 μm and will determine the minimum features size that can be produced [4]. The hatch spacing is the distance between two adjacent scan tracks in the same scanned layer. A representation is reported in Figure 1.5, where the semi-elliptical blue regions are the melt pool cross sections of the scan tracks. If the hatch spacing is too high, there is the risk of having unmelted loose powder and porosities between the adjacent scan tracks. However, if the overlap of the two scanning tracks is too high, an already scanned region melts again and could end up in a non-uniform metallurgical structure in the component [8].

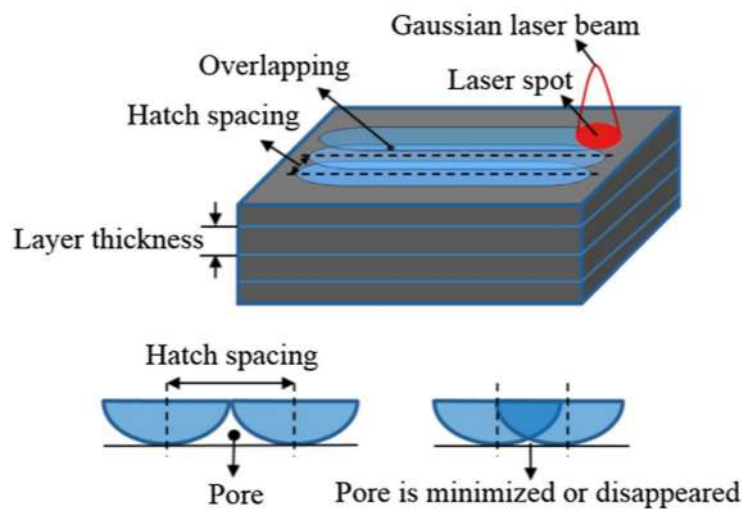


Figure 1.5: Hatch spacing of adjacent scan tracks.

The combination of these process parameters will determine the final result of the manufacturing process. Their value will affect the component quality and even its mechanical and thermal properties. The optimal combination of these parameters highly depends on the application and on the LPBF machine used. Optimization studies are a hot topic in AM literature since there are limited robust models or rules yet.

Some advantages of the LPBF manufacturing process are:

- the possibility to use a wide range of materials such as Aluminium, Titanium, Iron and Nickel based alloys [8].
- the production of complex near-net-shaped components ready to use, if the surface roughness levels are acceptable for the application.
- the ability to tune mechanical, electrical, thermal and acoustic properties of the component by acting on the process parameters, which have influence on the final micro-structure of the part [4].

On the other hand, some disadvantages are:

- the relatively slowness of the process with high power usage and low volume capabilities.
- high initial costs of the machine.
- discrepancies between the desired CAD model and the actual produced part as the features size gets lower. Moreover, the minimum feature size is constrained by the laser beam spot size [4].
- the presence of micro-structural and metallurgical defects such as unmelted powder adhesion, porosities, cracks, residual stresses, thermal distortion and anisotropic micro-structure.
- not all the geometries are feasible in a near-net shape. Components are subjected to manufacturability constraints, as it will be explained in section 1.2.2.

1.2.2. LPBF geometric defects

In this section are listed some of the main constraint and defects relative to the LPBF technology.

Manufacturability constraints Not all the geometries can be directly manufactured using LPBF. According to the studies [9–11], one of the most limiting constraint is the

maximum inclination angle for overhanging structures in relation to the vertical growth direction. If a feature is inclined more than this critical angle, the manufacturing quality will highly reduce and geometrical distortion will happen. This critical angle is commonly adopted as 45° . Moreover, also the length of overhanging structures is a technical challenge for LPBF technology. The allowable overhang distance however with no supports is highly dependent on part geometry, material and process parameters and there are no generally adopted rules. It is typically in the order of magnitude of millimeters.

Both these constraints could be partially relaxed by including support structures in the desired part. These components will help stabilizing the structure during the process, allowing more design freedom. However, post processing would be necessary to remove these extra supports. This could not be an easy task for certain complex geometries and would highly affect final costs. The need of support structures could not only depend on geometry, but also on build direction. In some cases, the need of supports could be eliminated only by changing the orientation of the part in relation to the growth direction. An example is reported in Figure 1.6 from the study of Jiang et al. [12]. In the first two images, some features of the T-shaped component overcome the 45° critical angle and need the support structures, represented in green. The optimal part orientation of the last image shows how the part could be produced without the use of supports.

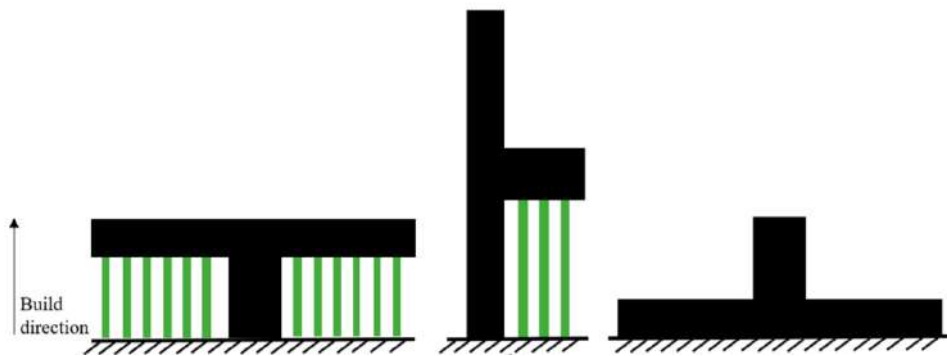


Figure 1.6: Support structures in LPBF.

The dimension of the minimum feature that can be reliably manufactured depends on laser spot size and process parameters. Maconachie et al. [4] reports values of $300\ \mu\text{m}$ feature size found in literature.

Dimensional accuracy and surface roughness As studied by Maconachie et al. [4], another strong limitation of LPBF regards the discrepancies between the nominal intended geometry and the actual produced component. These differences are more severe as the desired feature size gets smaller and geometry is close to technical constraints of

the AM machine. These differences may be due to shrinkage during cooling, adhesion of unmelted particles to the structure, waviness and roughness of slender components. All these distortions could highly affect the expected mechanical behaviour of the components in terms of strength, stiffness and could lead to premature failure. In Figure 1.7 are reported examples of a distorted manufactured lattice structure from the study of Grosmann et al. [7].

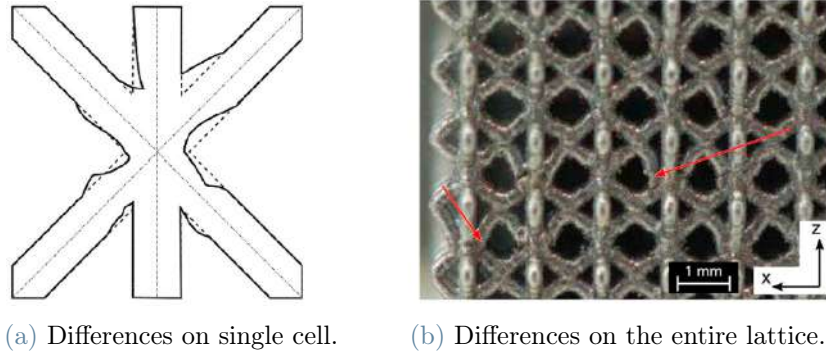


Figure 1.7: Geometrical discrepancies between desired and produced geometry.

The staircase effect is another problem related to LPBF manufacturing procedure. As shown in Figure 1.8, it is due to the discretization of the as-designed component into finite thickness layers. The inclined structures are manufactured with a segmented profile which highly increases surface roughness. Moreover, on the downward-facing surfaces in direct contact with the powder bed there is adhesion of undesired unmelted particles due to melting pool depth and possible overheating in these regions. These particles, absent on the upward-facing surfaces of the component, severely contribute to dimensional inaccuracy and to surface roughness of the final part. The less inclined the structure, the less acute the staircase effect would be.

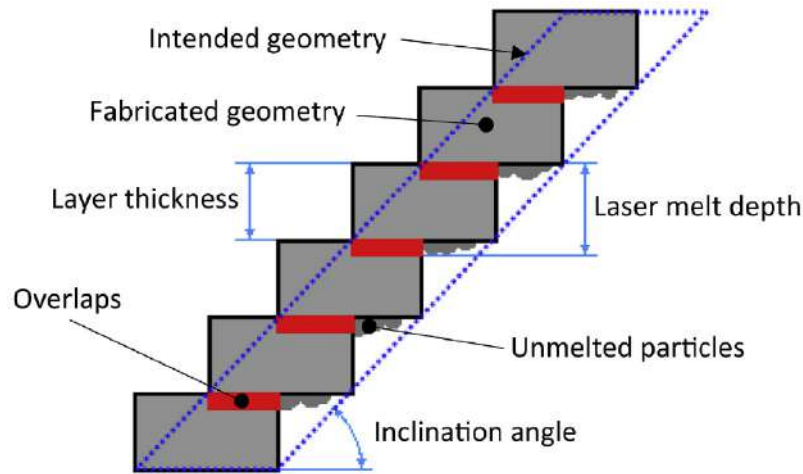


Figure 1.8: Staircase effect in LPBF.

Metallurgical defects As stated by Galy et al. [13] one of the main metallurgical defect that affects LPBF are porosities. Pores in the components can originate from a particular choice of process parameters that determine lack of fusion (mainly laser power and scan speed, but also hatch distance as shown in Figure 1.5) or from the interaction and absorption of surrounding gas. These porosities, in particular the non-spherical one, can lead to the formation of internal cracks in the component. Relative density of the component compared to that of bulk material can be used to understand the amount of porosities. An example of pores in a component is reported in Figure 1.9a.

Another phenomenon investigated is hot cracking. These cracks are due to the large residual stresses that generate during fast cooling of the melted metal pool. Olakanmi et al. [14] affirms that this phenomenon could be explained by the large solidification temperature range of Aluminium alloys, high coefficient of thermal expansion and large solidification shrinkage. Besides the influence of process parameters, the formation of hot cracks is sensible on metal powder chemical composition. The addition of alloying elements like Silicon or Nickel can reduce this problem. An example of cracks in a component is reported in Figure 1.9b.

The presence of Oxygen in the chamber is highly reduced by adopting inert gases, but it is still present in low quantities. This leads to the formation of oxides on metal powder and on melted pool surface. The formation of oxides, especially for the reactive aluminium alloys, constitutes a problem for mechanical performance of the component as well. These oxides could enter the melted material and become inclusions in the component. Hard inclusions often induce crack initiation, lowering the mechanical properties of the part [15].

Lastly, LPBF manufacturing process causes micro-structural anisotropy in the component. The partial melting of previous layers during fabrication, coupled with large temperature gradients and complex heat transfer due to the cyclic processing, leads to elongation of grains [4, 15]. Their preferential growth direction is determined by laser scanning path and component geometry. The anisotropy of micro-structure influences mechanical properties of the component. Properties like strength, stiffness and hardness depend then on grain elongation direction in relation to the component. Moreover, rapid solidification can lead to grain refinement, which results in enhanced deformation resistance, but may also induce segregation phenomena or non-equilibrium phases [4]. Heat treatments offer the chance to alter the obtained micro-structure, which indirectly modifies the mechanical response of the component.

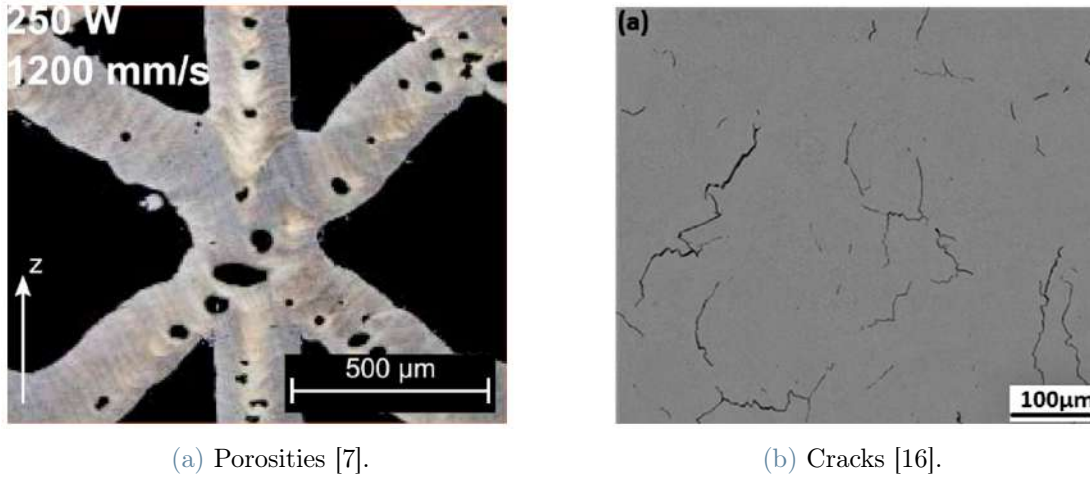


Figure 1.9: Examples of metallurgical defects.

1.2.3. Mechanical properties of Aluminium alloy manufactured by LPBF

A characteristic of LPBF process is the fast cooling of the laser melted material. The high solidification rate of the metal leads to the formation of finer grains compared to those obtained with conventional casting process. This different micro-structure influences the mechanical response of the components. General values of mechanical properties of aluminium alloy manufactured with the two processes have been found in different studies [15, 17] and are reported in Table 1.1.

Process	Yield strength [MPa]	UTS [MPa]	Hardness [HV]
Casting	276	300 - 317	86
LPBF	270 - 320	360 - 430	133 - 146

Table 1.1: Mechanical properties of Aluminium alloy.

The finer grains of the parts produced by LPBF confer higher strength and hardness to the components.

1.3. Heat exchangers and Additive Manufacturing

A literature research has been carried out to disclose possible techniques to enhance heat exchangers performances exploiting Additive Manufacturing potentialities. Kaur et al. [18] performed a comprehensive review of the main types of heat exchangers produced by AM. The influence of different implemented features on the thermo-hydraulic performances of the component are analysed. Some of the most interesting conclusions are related to the effects of surface roughness, to the presence of features in channels that disrupt the flow and to the adoption of cellular materials in the component. These topics are analysed in the following paragraphs.

Surface roughness High surface roughness is an intrinsic characteristic of most parts produced by LPBF. In LPBF, the surface roughness is mainly determined by the unmelted metal particles that stay attached to the main structure. Surface roughness turns out to be a key parameter in heat exchanger performances since it helps promoting turbulence and mixing near the walls, disturbing the near-wall viscous layer, and so facilitating heat transfer. However, high roughness is detrimental to the pressure drop, especially if the channels in which the fluid must flow through are narrow [19].

Turbulence promoters In the study of Alam et al. [20], it is introduced the concept of artificial roughness. The idea is to design small repeated features in fluid channels to disturb the fluid flow, promoting turbulence so to enhance heat transfer. The performances of the heat exchanger, in terms of heat transfer and pressure drop, strongly depend on the type, dimension and arrangement of the implemented features. Ligrani et al. [21] and Shen et al. [22] analysed different types of features such as pin fins, rib turbulators, Kagomé strut-based lattice structure and spherical dimples applied inside turbine blades internal cooling channels. The cooling of such components is essential since they work in extremely hot conditions. Pressure loss in these channels should be limited to avoid

power losses. These additional elements promote turbulent motion of compressed air flow in blades' cooling channel to keep temperature down. An example of flow mixing is reported in Figure 1.10a. Vortex formation in the channel increases heat transfer at the expense of additional pressure losses. From these experiments, the solution with the best heat transfer performance with lowest pressure drop appears to be adoption of dimples only on one channel wall and smooth surface on the other sides. Their presence does not obstruct the flow as much as the other features, but it is enough to induce significant vortices beneficial for heat transfer. Figure ?? represents the profile of a single spherical dimple with exemplary dimensions. This solution seemed interesting for the internal channel of the cooling jacket and was then assessed with CFD analysis in section 3.5.1. Kagomé strut-based lattice structure, shown in Figure 1.12b, offers as well an interesting solution. The combination of high flow perturbation and increased heat transfer area makes this structure an interesting solution for thermal management applications. It will be investigated in section 1.4.

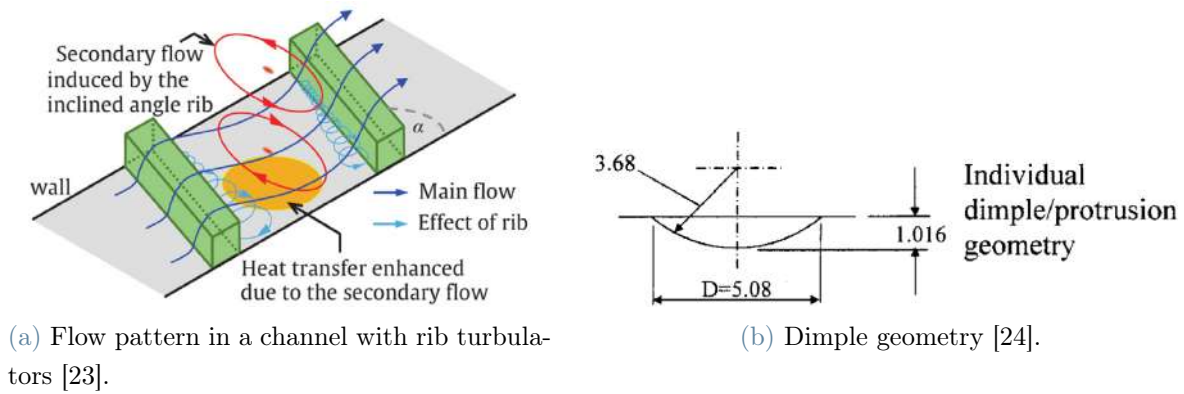


Figure 1.10: Examples of turbulence promoters.

Rastan et al. [25] studied the influence of rectangular winglets produced by AM on a flow in a narrow channel, heated from the bottom face. The purpose is again to generate vortices and turbulence in the fluid flow. Different winglets dimensions and orientations have been studied. The best configuration led to a heat transfer 3 times higher than the empty channel, but with a significant increase of pressure loss up to 9 times the empty channel one. Moreover, a similar solution with small wings in the internal channel was previously studied for the cooling jacket by Dynamis team. It was rejected due to excessive pumping power required and non-homogeneity of motor surface temperature.

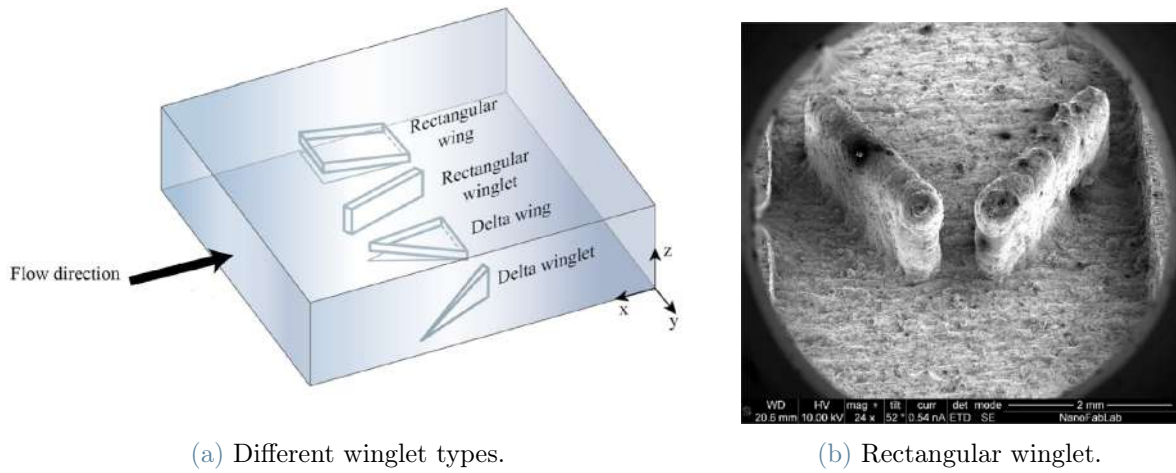


Figure 1.11: Winglets in a narrow channel [25]

Cellular materials Various types of cellular materials are investigated in the study [18], including metal foams, strut-based lattice structures and TPMS materials. The characteristic of a general cellular material is that in the metallic body contains any kind of gaseous voids are dispersed [26]. Metallic foams are made of a stochastic distribution of open and closed metal cells. The interconnections between internal voids allow a fluid to flow through the metallic structure of open-cell foams. They are typically manufactured by powder metal sintering on a polymeric foam substrate or gas injection in molten metal. They offer many advantages in thermal management application and have been widely used in heat exchangers. However, this solution has been discarded for the cooling jacket application due to the known difficulty in bonding these structures on the heated solid part which is to be cooled and massive pressure drops of fluid flowing through them [27].

Studies on TPMS structures applied in heat exchangers are growing due to their great heat transfer capabilities combined with low volume consumption. However, their application in the cooling jacket has already been studied by the previous thesis with the gyroid structure. Finally, strut-based lattice structures are a valuable option to be implemented in heat exchangers and deserve a dedicated section in this chapter.

1.4. Strut-based lattice structures in heat transfer applications

Strut-based lattice structures are "topologically ordered, three-dimensional open-celled structures composed of one or more repeating unit cells. These cells are defined by the dimensions and connectivity of their constituent strut elements, which are connected

at specific nodes." [4]. Thanks to LPBF capabilities, the interest of strut-based lattice structures application in heat exchangers is rapidly increasing and they are already deeply investigated in literature. These structures' attractiveness comes from their lightness and high surface area, while keeping an overall simple design. In Figure 1.12 are reported some examples of the most common strut-based lattice structures that can be studied and adopted to enhance heat transfer performances.

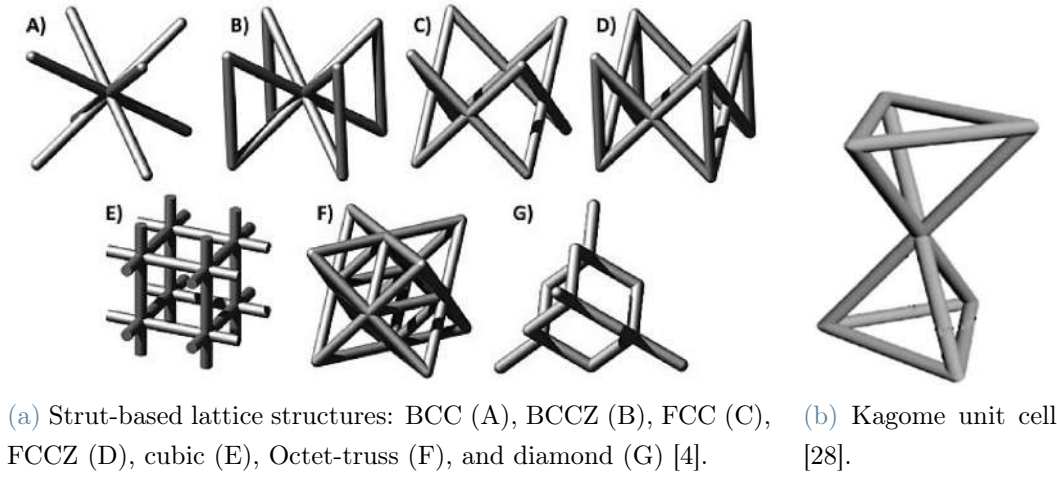


Figure 1.12: Strut-based lattice frame material.

Another important structure, derived from the Kagome shown in Figure 1.12b, is the simpler tetrahedral cell reported in Figure 1.13a. It consists of 3 struts forming a pyramid with equilateral triangular base. This structure is of particular interest due to extensive experimental and numerical research of its application as a mean to enhance heat transfer performance. Kim et al. [29–32] studied the interaction of forced air flow through a regular set of tetrahedral cells. The aluminium cells are built on a flat metallic plate, which is heated from the bottom face. Heat is driven in the struts by conduction and transfers to air by convection. Results of the experiments are expressed in terms of heat transferred and pressure loss for different flow velocities. Results are then compared to the performance of an empty channel with same dimensions to understand possible advantages of using these cells.

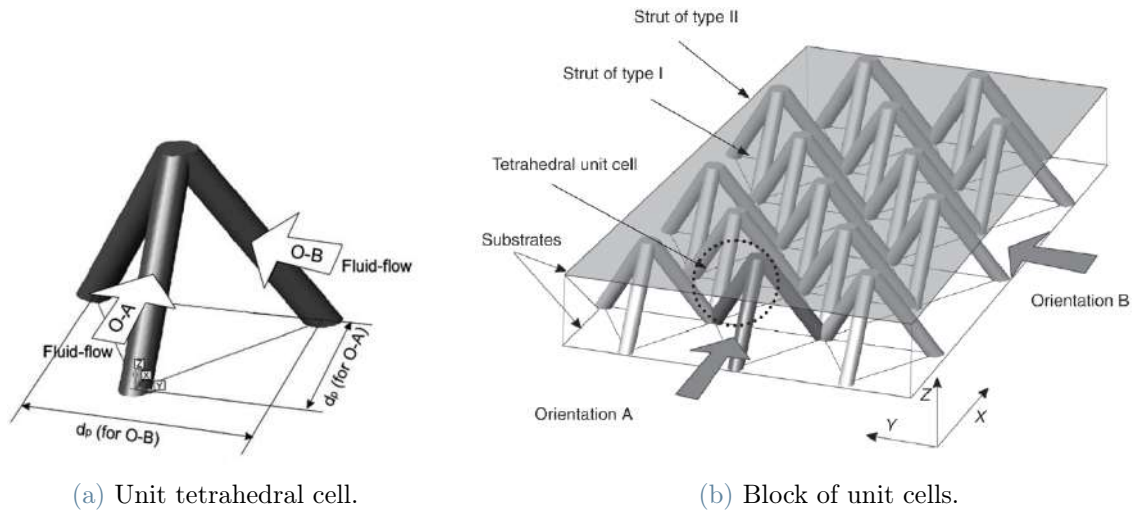


Figure 1.13: Tetrahedral lattice frame material. [29]

By adopting this geometry in a channel, numerical and experimental results highlight a significant increase of heat transfer compared to empty channel. This enhancement can be associated to two distinct phenomena that are valid for all the strut-based lattice structures:

- Flow mixing, due to the turbulence generated in the flow by the lattice structure. Vortexes formation around struts and on the heated plate disturbs the flow boundary layer and appears to be a relevant element to enhance heat transfer performance. Turbulence by itself can increase heat transfer up to 3 times compared to empty channel. This conclusion will be a key aspect to keep in mind during the internal channel design stage of this thesis. A material with poor thermal conductivity has been used to isolate this turbulence phenomenon, so to limit conduction through the cells.

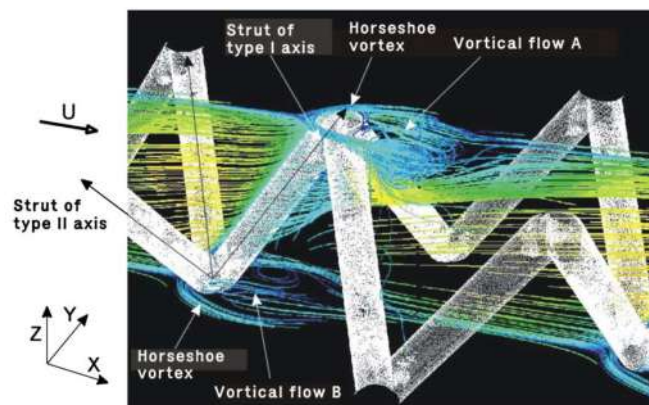


Figure 1.14: Vortex structures around a cell. [30]

- Increase of heat transfer surface, due to conduction from the heated plate to struts and then convection from struts to fluid flow. This phenomenon further increases heat transfer compared to empty channel up to 7 times.

Regarding pressure loss, due to cell anisotropy, the orientation of the fluid flow through the cells appears to be a crucial aspect for the general performance of the lattice structure. Referring to Figure 1.15, when the flow impacts the cells along orientation A it propagates in a symmetrical way, but it encounters a higher resistance due to high passage blockage. On the other hand, an incoming flow along orientation B will propagate in an asymmetrical way, but the flow resistance will be much less since the cell frontal area is more open to the flow. Pressure drop of the flow in orientation B is approximately half the one along direction A since it leaves a more open passage to the refrigerant flow.

Surprisingly, it turns out that heat exchange is independent from the flow orientation.

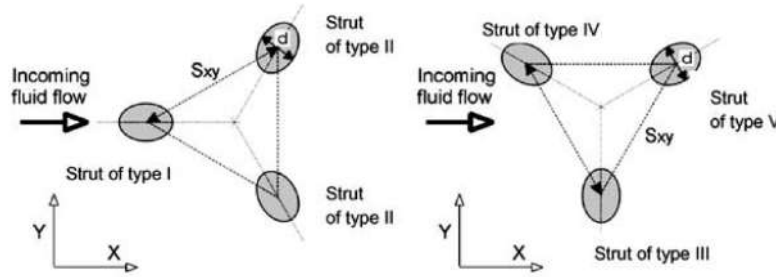


Figure 1.15: Anisotropy of the tetrahedral cell. [29]

The last parameter studied is cell porosity, calculated as the empty volume in a cell over the total cell volume. It is the complementary parameter to relative density, and it depends on cell dimension and strut diameter. Experiments show that, considering only heat transfer, the optimum porosity is about 0,8. In fact, a higher strut diameter is desired to have a good conduction through all strut length. When pressure loss is taken into account, thinner struts are preferred to have less flow blockage. The optimal porosity becomes 0,938.

Tian et al. [33] studied a comparison between the tetrahedral unit cells lattice structure (also presented as Lattice Frame Material LFM), Kagome and other structures like metal foams and aluminium fin arrays applied in heat exchangers.

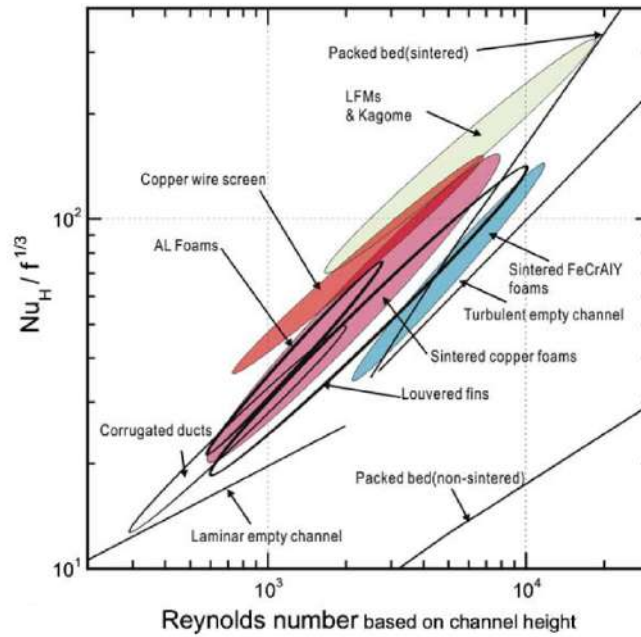


Figure 1.16: Performance chart of different heat dissipation media [33].

The graph in Figure 1.16 shows the thermal efficiency index. It classifies the heat transfer capabilities of different types of heat exchangers for the same pumping power. At high Reynolds (where the resistance given by shape is prevalent on viscosity) the periodic structures have a higher thermal efficiency. LFM and Kagomè show the best overall performance between the different structures considered.

Kaur et al. [34] studies the main defects in additively manufactured strut-based lattice structures. One of the most common defects observed in lattices produced by LPBF is the surface roughness. As investigated in section 1.2.2, it is mainly due to the unmelted metal particles that adhere on the struts. High surface roughness would be positive from heat transfer perspective, but it would be detrimental for flow pressure loss. Moreover, the discrepancies of the manufactured part compared to the as-designed component will affect the final porosity value of the lattice structure. This would be particularly negative from thermo-hydraulic point of view if the unit cell dimension of the lattice is small.

2 | Cooling Jacket Design - Introduction

The starting point of this cooling jacket design is the solution adopted by Dynamis Team during season 2019 – 2020. Main design areas are the internal water channel with relative inlet and outlet manifolds and external fins to increase thermal power transfer from the heated jacket to ambient air. This is eased by the fact that wheels are not covered and a good amount of air flows in the cooling jacket region. The complex fins arrangement is visible in Figure 2.1. In this picture however, the internal geometry was deleted as a matter of project secrecy. Axial fixing is guaranteed by a flange fastened to motor group.

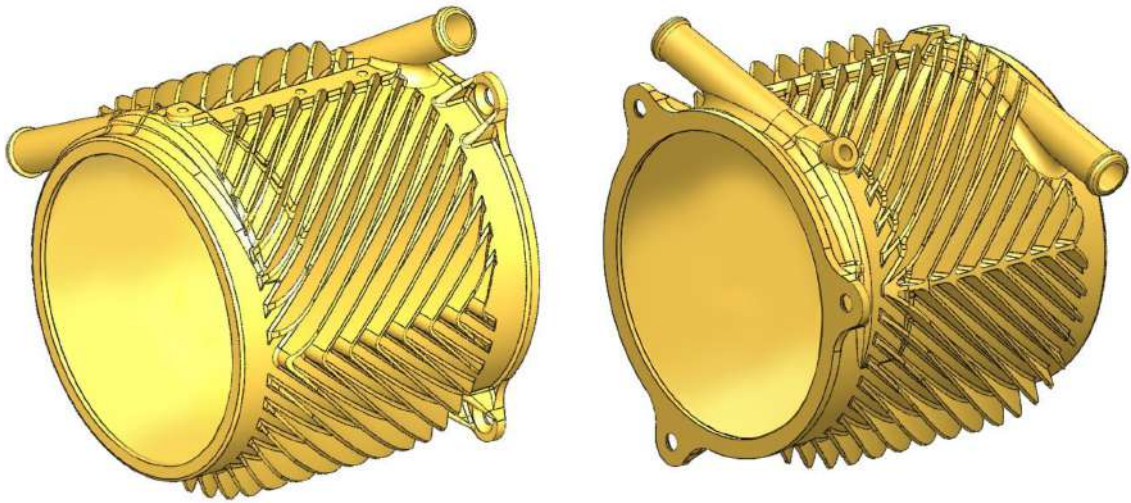


Figure 2.1: 2019 - 2020 design of Dynamis cooling jacket.

Starting from this solution, this project studies the implementation and influence of some features reported in the previous chapter to enhance the component performance. The design phase can be divided into two distinguished areas: the internal channel and the external fins. The final solution is considered to be the combination of the best performing internal and external configurations. Indexes of a good solution are high heat transfer, low pressure drop (mainly for the internal channel), limited volume and lightness to enhance

overall performances.

The conceptual map in Figure 2.2 sums up all the tested solutions and could be a useful tool to better follow the discussion.

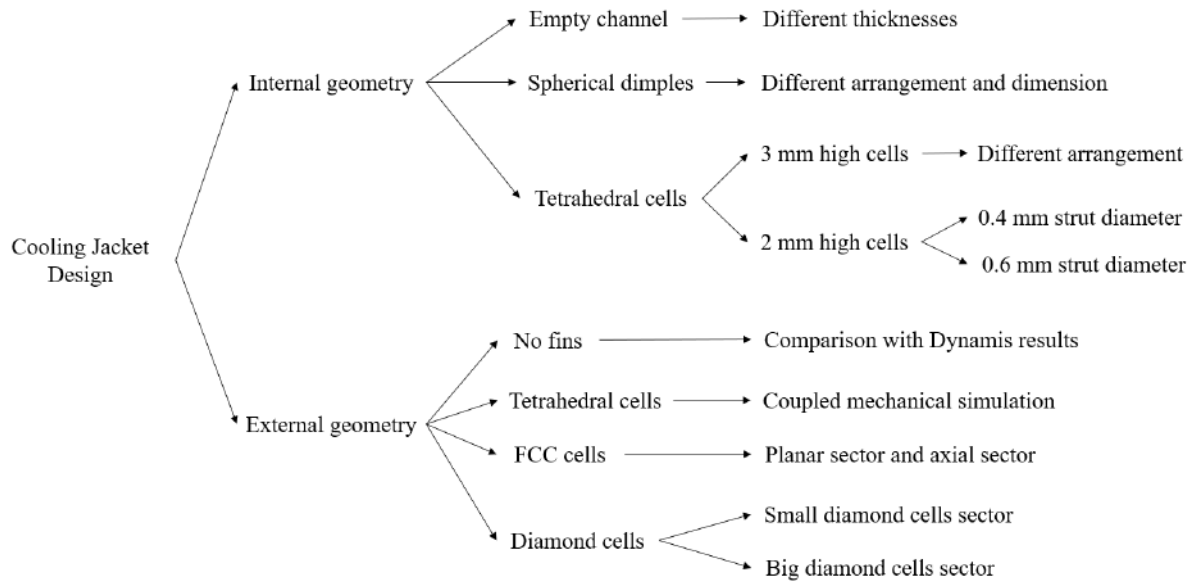


Figure 2.2: Conceptual map of studied solutions.

3 | Internal geometry design

3.1. Introduction

As discussed in Chapter 1, the cooling jacket will adopt the single shell configuration with circumferential water flow around the motor since this is one of the best compromises in terms of thermal management, performance and design complexity. The helical pattern of the water flow is guaranteed by internally manufactured thin walls that develop helically on the inside part of the cooling jacket. Their height determines the distance between the single shell of the component and the surface motor, which is the water channel height. The internal geometry of the water channel is then determined by these internal guiding walls. The mass flow rate delivered by the pump is considered fixed at 5 l/min for any assessed configuration. The model considers a constant heat flux from the electric motor at full power, generating 2200 W. The inlet water is at 40°C (about 313 K) and it is directly heated from the motor external surface until it reaches the outlet manifold. The initial simulations consider an empty channel with different thicknesses of fluid but fixed width. Once the general performances of these configurations are determined, different structures are designed in the channel and studied in terms of additional pressure drop and heat transfer capabilities increase.

However, due to limited computational power availability and complexity of studied solutions, the helical water channel that envelops the electric motor has been divided into curved sectors that have been studied separately. To further simplify modelling procedure and analysis, the different internal channel configurations are compared using only the first sector encountered by the incoming cold water. A single curved sector is then considered to be representative of the whole internal channel, allowing to directly compare various solutions in an easier way.

3.2. Numerical model

For each analysed configuration, the curved sector consists then of a fluid channel and a solid aluminium structure that simulates the single jacket shell and the internal walls

that guide the flow. The fluid domain will have rectangular cross section and fixed width for all models. A constant heat flux, calculated as the peak thermal power generated over motor surface area, is introduced into the model from the water surface opposite to the aluminium shell wall. At this stage, external fins on the jacket and ambient air are not considered. The model of the empty channel with 4.5 mm of water height is reported in Figure 3.1. The blue part represents the solid aluminium walls, while the transparent part is the fluid domain. The wider solid wall is a section of the 1.5 mm thick single shell that constitutes the cooling jacket, while the shorter walls are those that direct the water in the component and determine the helical water path. The lower free face of the water is in direct contact with the motor surface, through which heat flux is provided. Being constant the mass flow rate and channel width, water inlet velocity depends only on water channel height. The sector width is 25 mm and the internal radius is 48 mm, as the external radius of the cylindrical electric motor. The sector spans 90° of the component circumference. Considering motor dimensions, a single curved sector is about $1/16$ of the length of the internal cooling channel.

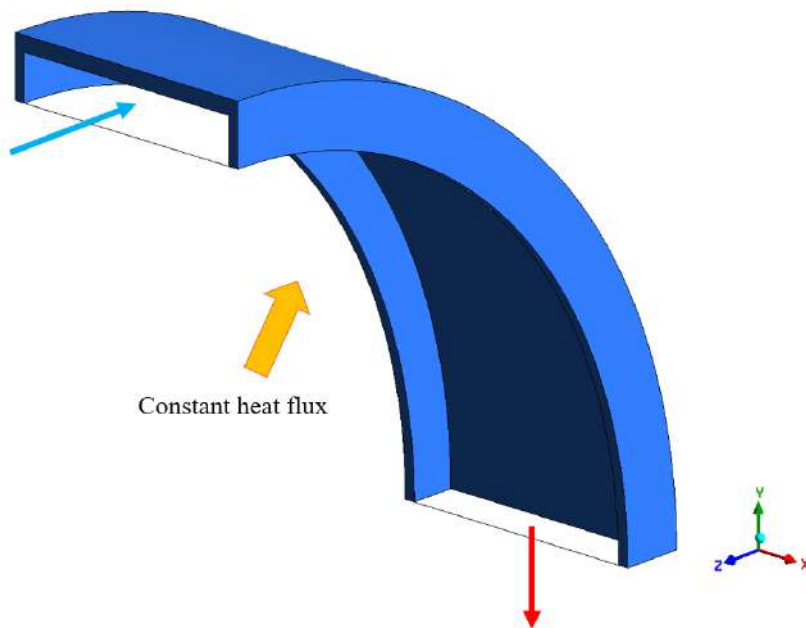


Figure 3.1: Model of the curved empty channel with 4.5 mm of water.

The solid parts have always been modelled using Inventor and exported as STEP files. The water domain was then added in Design Modeller module on Ansys Fluent from Workbench. Once fluid and solid domain are defined, the following step is meshing. Meshing is a crucial part of CFD analysis for good quality results. Solid mesh should be fine enough to correctly describe conduction, while fluid mesh must capture heat

convection and interaction with the solid part. Inflation layers were used to accurately describe the steep gradients of velocity, temperature and pressure at fluid - solid interface and better describe the heat transfer process. Inflation layers consist in a gradual mesh refinement on fluid side in correspondence of solid walls, where fluid boundary layer develops. To obtain good results, the entire boundary layer must be contained in the inflation layers used, which are characterised by number, thickness of the first layer and growth rate. Distant to the wall, where the effects of the boundary layer are no more present, a tetrahedral mesh is enough to describe the behaviour. A mesh quality index is the dimensionless wall distance y^+ . It is defined as:

$$y^+ = \frac{\rho y u_T}{\mu} \quad (3.1)$$

where ρ is the fluid density, u_T is the friction velocity which depends on fluid density and on the wall shear stress, μ is the dynamic viscosity of the fluid and y is the absolute distance of the mesh first layer element centroid from the wall. When this value is close to 1 at fluid - solid interface, inflation layers are thin enough to capture the behaviour in the viscous sublayers. In this case, no approximating empirical wall functions are needed to describe the behaviour in the boundary layer. However, it is possible to check this value only after having performed a full CFD analysis. If the y^+ appears to be much larger than 1 on most of the interfaces, the mesh must be refined reducing the first layer thickness and analysis must be run again. Especially in large scale models with complex geometries, this could lead to high computational demand.

Once the mesh is complete, it is passed to the solver. After checking mesh quality and scale correctness, solving models must be selected. The Energy model responsible for thermal calculations is set to On and SST k - ω model is activated. This model is a low-Reynolds turbulence model which can integrate the turbulence near the wall to correctly describe fluid behaviour. To do so, it needs to be used on a good quality mesh with the appropriate y^+ close to 1. Water and aluminium materials are assigned to respective zones and boundary conditions are set in terms of inlet velocity and constant heat flux from the water wall in contact with the motor. A surface roughness of 10 μm is assigned to solid walls in contact with the water flow. Solid - fluid interfaces must figure as "coupled walls" to correctly predict heat transfer. The analysis then is initialised and solution can be run.

Results can be analysed in the dedicated post processor, extracting information regarding pressure losses and thermal management. Having analysed only a sector instead of the whole water channel, the following statements are considered to choose the best performing

solution:

- The total pressure loss of the whole cooling jacket is obtained by applying the linearity assumption as the sum of the consecutive pressure drops of all the sectors in which the jacket is divided. All the sectors of the same cooling jacket have the same geometry and inlet velocity boundary condition, so the pressure drop is assumed to be the same for all of them. Since the objective is to compare different solutions, local losses due to inlet and outlet connections are neglected because they would be independent from internal channel geometry. From this point of view, the best channel design is the one with less pressure drop. The single channel pressure drop is the difference between the area-weighted average of pressure on inlet and on outlet faces.
- From heat transfer point of view, the convective heat transfer coefficient (CHTC) of the first sector encountered by incoming water is used as discriminant to select the best configuration among the tested one. It is defined as:

$$h = \frac{\dot{q}}{T_{surface} - T_{ref}} \quad (3.2)$$

It depends on the heat flux \dot{q} provided from the motor to the water and on the temperature difference between unperturbed fluid flow T_{ref} and the interface temperature $T_{surface}$. Since the first two values are assumed constant at their imposed values, the main variable leading the choice becomes the motor average surface temperature in the sector. The higher the motor temperature, the lower convective heat transfer coefficient, which means lower heat transfer capability of the channel geometry. Moreover, by looking at temperature maps, solutions that generate high local hot spots will be discarded since the motor surface temperature should be as uniform as possible.

3.3. Planar sector assumption

The first assumption made to simplify the study of the internal geometry was to consider a single curved sector to be representative for the whole internal channel, allowing the comparison of single sectors to study different configurations. Another important assumption can be made and numerically proved to further simplify the CFD analyses. The curved sectors can be converted to planar sectors having the same dimensions, assuming that their behaviour in terms of pressure drop and heat transfer capabilities will only slightly change. The modelling procedure would be highly simplified, still allowing direct com-

parison between different internal geometries. To demonstrate this assumption, a planar sector was modelled and tested under the same boundary conditions of the curved sector shown in Figure 3.1. The planar sector model of the empty channel with 4.5 mm of water is reported in Figure 3.2. Also in this case, the blue part represents the solid aluminium walls, while the transparent part is the fluid domain. The vertical shorter walls are those that guide the water in the component and determine the helical water path, while the wider wall is a section of the component single shell. The heat flux is provided from the lower free face of the water, which is in direct contact with the motor surface. Being constant the mass flow rate and channel width, water inlet velocity still depends only on water channel height. The sector width is 25 mm and it is 75 mm long. Considering motor dimensions, a single sector is again about 1/16 of the length of the internal cooling channel.

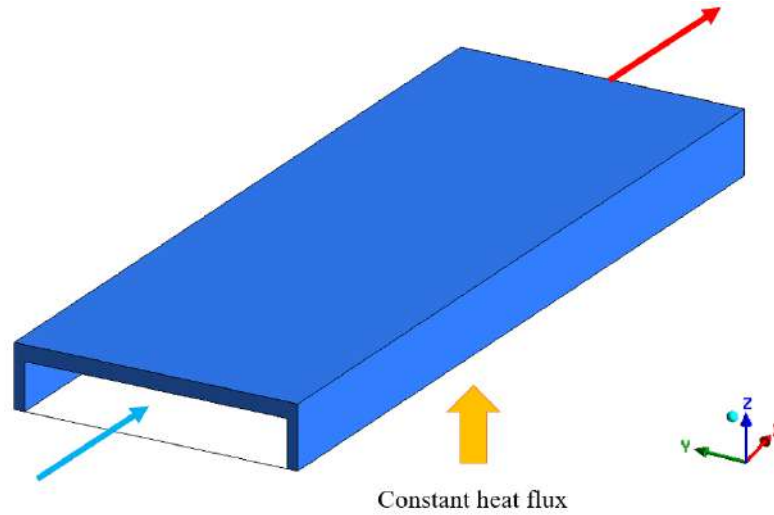


Figure 3.2: Model of the planar empty channel with 4.5 mm of water.

The CFD analyses set up steps are explained in section 3.2 and are the same for both models. Results for the 3 mm high empty water channel configuration are summarised in Table 3.1.

Model	Water velocity [m/s]	Sector ΔP [Pa]	h [W/m ² K]
3 mm curved empty sector	1	415.07	5777.10
3 mm planar empty sector	1	392.85	5787.18
Difference [%]		-5.4%	+0.2%

Table 3.1: Comparison of 3 mm curved and planar empty sectors.

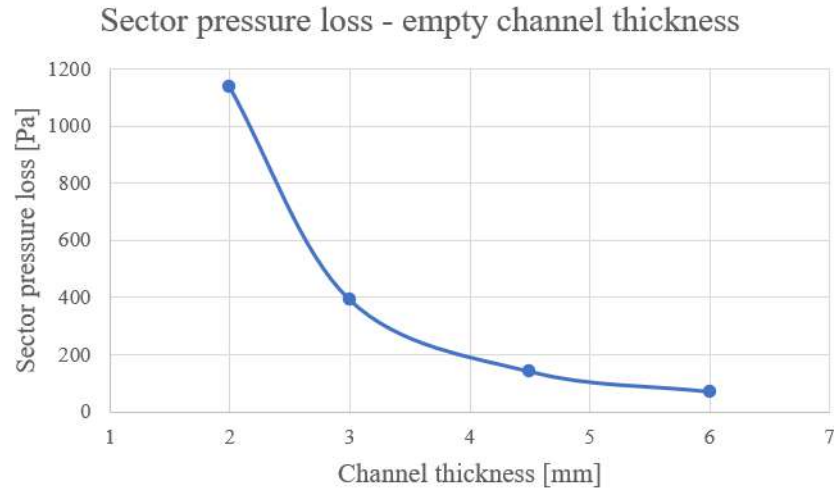
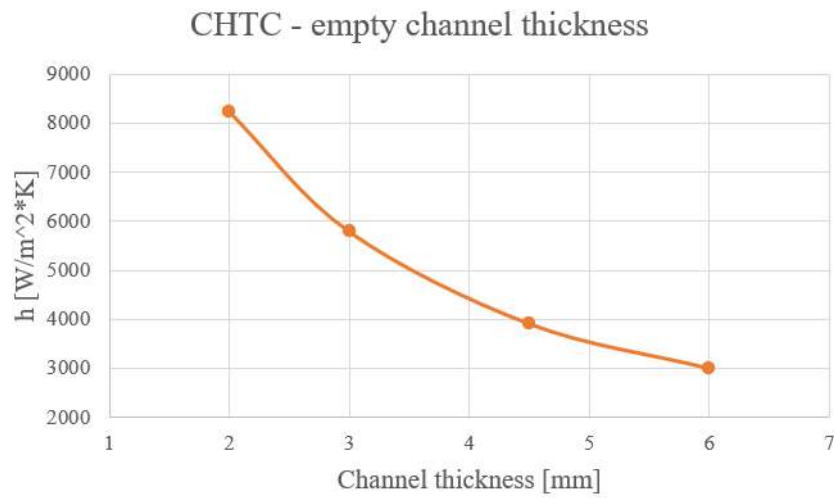
The difference between the two models is contained around 5%, especially in terms of convective heat transfer coefficient. Several other geometries have been tested for the comparison of curved and planar sector, leading to the same conclusions. A planar sector is then considered to be a valid and coherent substitute for a curved sector modelling the same configuration, hence to be representative of the whole internal channel. Therefore, all the following analyses of different internal configurations will refer to the planar sector model shown in Figure 3.2. The numerical procedure expressed in section 3.2 is still valid and needs no adaptation for the planar sectors geometries.

3.4. Influence of channel thickness on empty channel

As a starting point, the empty planar channel is analysed at varying channel thickness. Keeping fixed the water flow rate and channel width, water velocity decreases as channel height increases. In Table 3.2 are reported results in terms of pressure losses and CHTC for the different water channel thicknesses and their respective velocities. Figure 3.3a and Figure 3.3b respectively represent pressure loss and CHTC trend as function of water channel thickness. A slower flow in a thicker channel is significantly better from pressure drop point of view, but the thermal transfer effectiveness is lower and motor temperature is therefore higher. On the other hand, a fast flow in a narrow channel produces very high pressure drop but thermal performances improve. A trade-off velocity is then required to balance these two opposing objectives.

Channel thickness [mm]	Water velocity [m/s]	Sector ΔP [Pa]	h [W/m ² K]
2	1.5	1138.04	8240.19
3	1	392.85	5787.18
4,5	0.667	141.45	3906.16
6	0.5	71.15	2996.03

Table 3.2: Empty channel thickness effect.

(a) ΔP - channel thickness

(b) h - channel thickness

Figure 3.3: Performances trend for empty channel having different thicknesses.

3.5. Implementation of enhancing techniques for the internal channel

Starting from empty channel results, some of the previously exposed structures to enhance heat transfer are applied into the channel. As reported in various works [29–31], the main factors that increase thermal performance of a heated fluid channel are an increase of heat transfer surface and increase of turbulence in the flow. Unfortunately, due to the single external shell configuration of the cooling jacket, the first and most effective method

cannot be exploited. The additional structures that can be manufactured cannot be directly in contact with the hot motor surface to avoid any possible damage. Heat will not propagate by conduction through these structures and therefore there will not be an increase in heat transfer area. By adopting the single shell cooling jacket, it is not possible then to fully exploit the potentiality of these additional structures. Therefore, the main idea is to use new channel configurations to promote fluid mixing and turbulence. In this way, the thermal boundary layer that naturally forms on motor surface should be disturbed and convection from solid hot surface to fluid should increase.

A pre-requisite to select an additional turbulence promoting structure for the channel is to stimulate mixing with the minimum possible pressure drop. Hence, the fluid should be perturbed with less possible channel blockage. The most promising techniques found in literature to achieve a good fluid mixing with lowest possible pressure drop are mainly the tetrahedral strut-based LFM and the spherical dimples. They will be applied in channels with different heights to understand their effects on performances. At fixed channel height, the expected results are that the empty channel should have less pressure drop than the channel with embedded structure due to less fluid blockage and convective heat transfer coefficient should be lower due to lower fluid mixing.

3.5.1. Spherical dimples

A spherical dimple is a portion of a sphere that can be manufactured on the internal side of the single shell cooling jacket. The model used for geometry is the one reported in Figure 1.10b. For this thesis work, the ratio between dimple diameter "D" and dimple thickness is kept constant at 5, as in the study of Mahmood et al. [24].

Two sector configurations with six dimples with a diameter of 4 mm have been studied: one with alternated dimples on two rows along flow direction (Figure 3.4a) and one where dimples on the rows are paired along flow direction (Figure 3.4b). Both figures consist of a top view and a side view of the channel. The influence on channel performance of their relative position, paired or alternated, and their dimension are studied with CFD analyses. They have been applied in all the studied water channel heights to understand their influence compared to empty water channel, apart from the 2 mm channel due to its limited space availability. The CFD set up steps and boundary conditions are the same as those presented in section 3.2 for the empty channel.

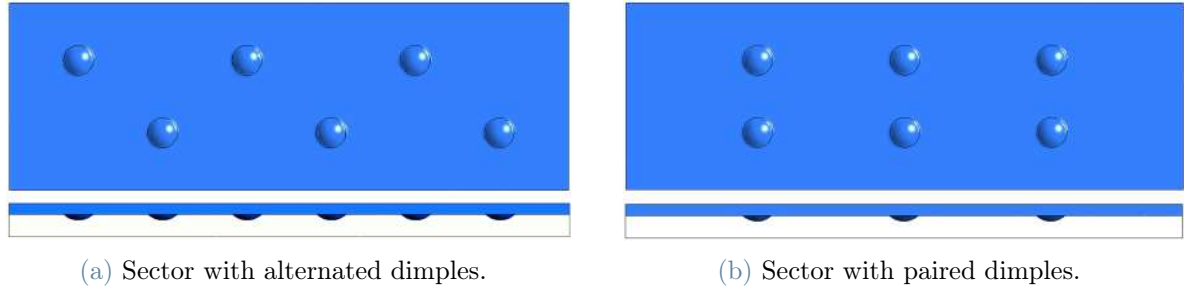


Figure 3.4: Geometry of sectors with 4 mm dimples.

Effect of dimple arrangement

The two presented configurations have been studied with various CFD analyses and, for a given channel thickness, their performances in terms of CHTC and pressure losses are extremely similar. The two geometries can be considered as equivalent and the dimples relative position as a non relevant parameter. For clarity reasons, the following discussion will only consider alternated dimples.

Effect of dimple dimension

The influence of dimple diameter has been studied for a fixed channel thickness of 4,5 mm. Dimples vary from the 4 mm diameter (as those shown in Figure 3.4) to 6 mm and 8 mm diameter. To preserve dimple shape, thickness must vary accordingly. Dimple thickness increases from 0.8 to 1.2 and 1.6 mm respectively for the different diameters. Figure 3.5 shows temperature maps at the interface between the water channel and motor surface, compared to the relative empty channel sector. They represent the motor surface temperature distribution of the first internal channel sector. This is the surface through which the heat flux is introduced into the model. The three maps are plotted with the same temperature scale to have a direct qualitative comparison. The higher dimple diameter, the less uniform temperature distribution on motor surface. The map for the 8 mm diameter in Figure 3.5d highlights the formation of colder spots in correspondence of dimples and hot spots where water velocity decreases. On the other hand, map for the 4 mm diameter in Figure 3.5b shows a more uniform temperature distribution without hot spots, but dimples influence is less effective in terms of decreasing average surface temperature.

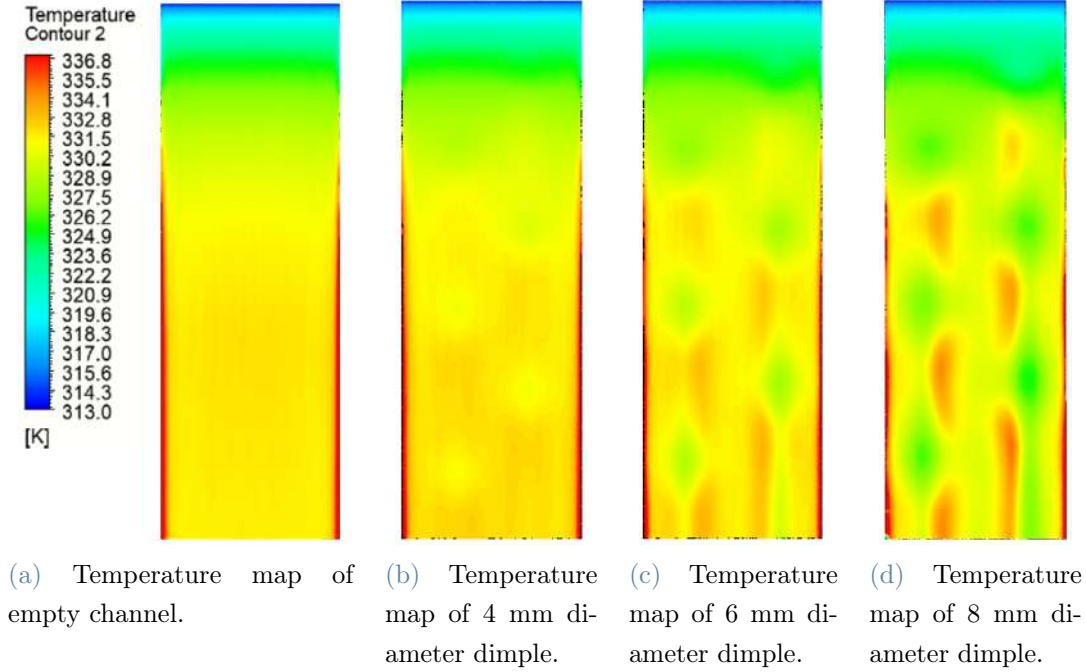


Figure 3.5: Influence of dimple diameter in 4.5 mm channel.

To further motivate the formation of cold spots in correspondence dimples, in Figure 3.6 is reported a velocity map in a section of the channel including a row of dimples. The presence of a dimple acts like a channel restriction and the flow speeds up. A local faster flow is beneficial for heat removal from motor surface. Behind the dimples there is low velocity region with formation of vortexes as disclosed in section 1.3.

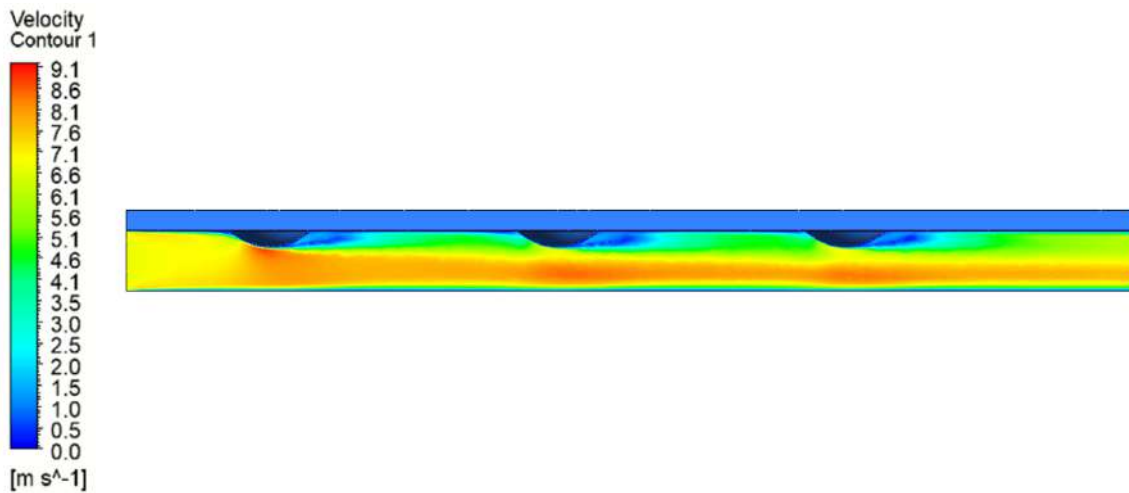
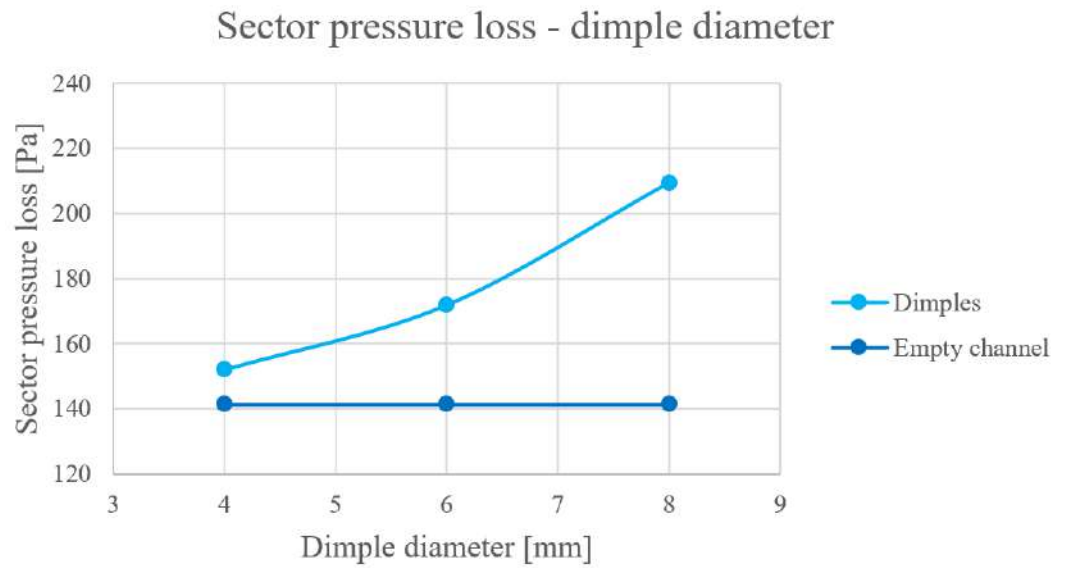


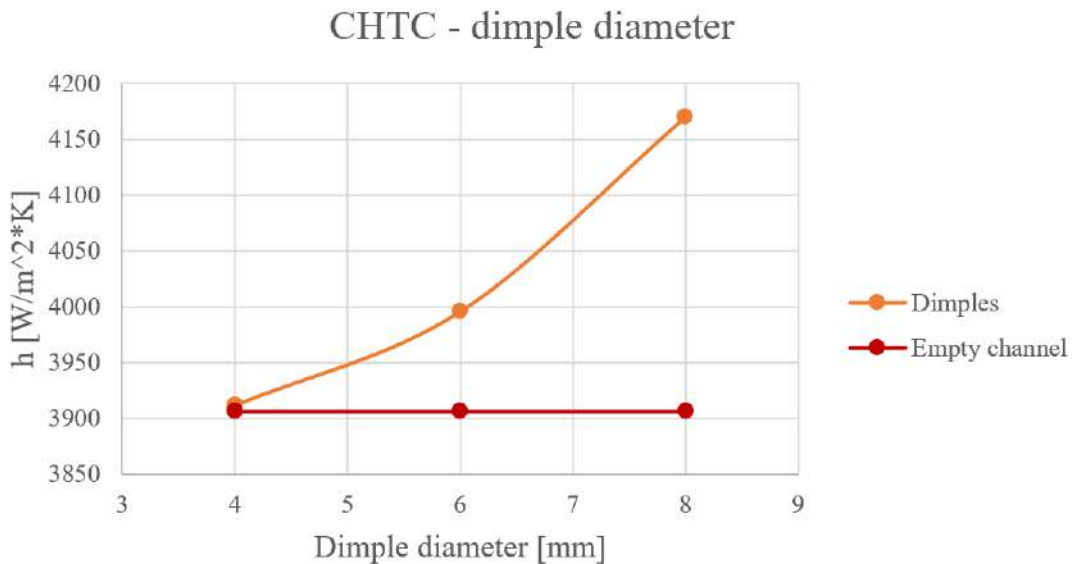
Figure 3.6: Water velocity profile in correspondence of dimples.

The graphs in Figure 3.7 show pressure losses and convective heat transfer coefficient

trends at varying dimple diameters. The higher dimple diameter, the higher fluid blockage and so the pressure loss. However, a bigger dimple helps in lowering the average surface temperature and thus increasing the CHTC. Comparing these results with performances of the respective 4,5 mm empty channel reported in Table 3.2, both pressure loss and CHTC are higher due the presence of dimples. This means that dimples help the fluid mixing and heat removal, at the cost of additional pressure losses.



(a) ΔP - dimple diameter.



(b) h - dimple diameter.

Figure 3.7: Effect of dimple diameter on performances.

The choice of the dimple dimension to be applied to other channel thicknesses was made

according to qualitative and quantitative results reported above. Despite the higher pressure loss, the 8 mm diameter dimples managed to keep lower the average surface temperature of the motor. However, they cause a non negligible formation of hot spots which are detrimental for motor performance and safety. Due to better motor temperature homogeneity, the solution that has been further studied is the one with 4 mm diameter alternated dimples.

Comparison with empty channel

After choosing the 4 mm diameter dimple, it has been applied to different channel thicknesses to understand their effect compared to the empty channel. In Figure 3.8 are reported the temperature maps of the 3 mm water channel thickness for the empty channel on the left and for the alternate dimples channel on the right. It is evident how dimples strongly influence surface temperature distribution, generating colder spots in correspondence of the protrusions.

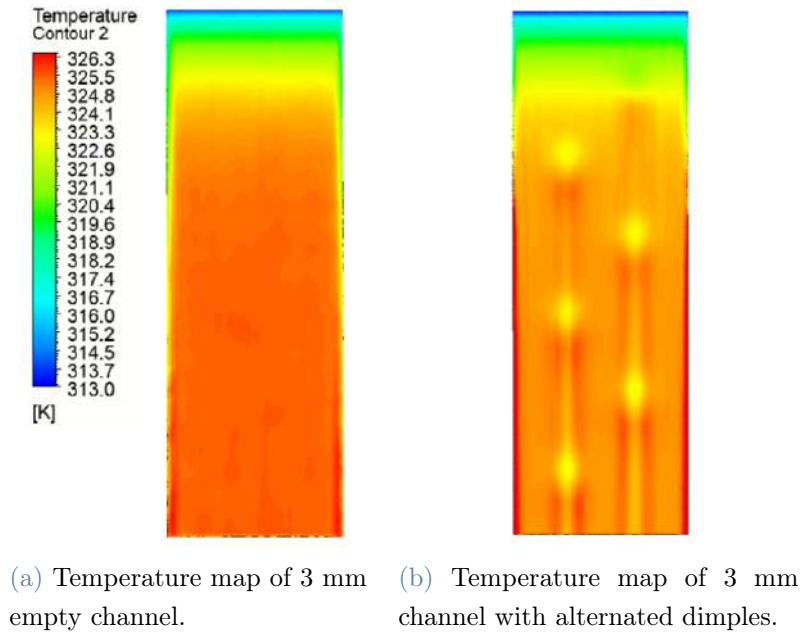


Figure 3.8: Influence of dimples on temperature map.

The channel thicknesses studied are 3, 4.5 and 6 mm. The performances of these channels are reported in Table 3.3. Dimples were not applied in the 2 mm water channel due to very limited space availability.

Channel thickness [mm]	Water velocity [m/s]	Sector ΔP [Pa]	h [W/m^2K]
3	1	436.143	5932.58
4.5	0.667	151.997	3958.36
6	0.5	74.656	3034.11

Table 3.3: Performances of channel with alternated dimples.

The graphs in Figure 3.9 show the trends of pressure loss and CHTC of the dimple geometry at different water channel thicknesses compared to empty channel performances. Dimples are able to slightly increase the thermal exchange by promoting fluid mixing, but there is also an higher pressure loss in the channel. The effect of dimples is less evident at higher channel thicknesses due to the higher gap between motor surface and dimples.

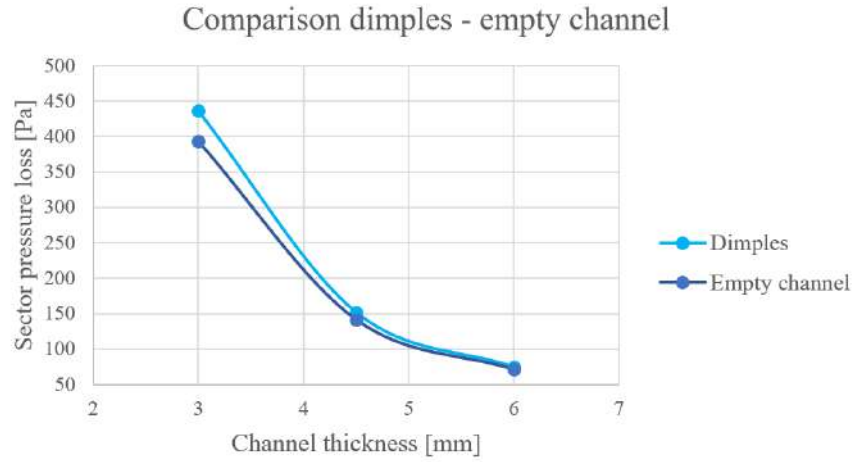
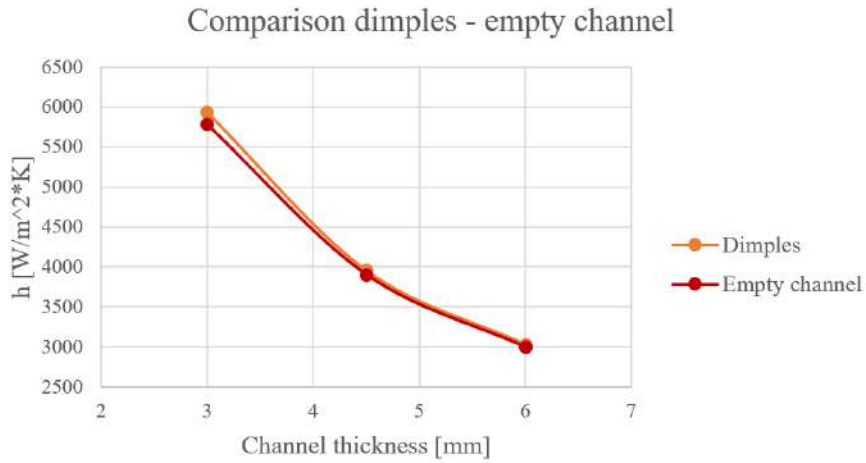
(a) ΔP - channel thickness.(b) h - channel thickness.

Figure 3.9: Comparison of empty channel and dimple channel

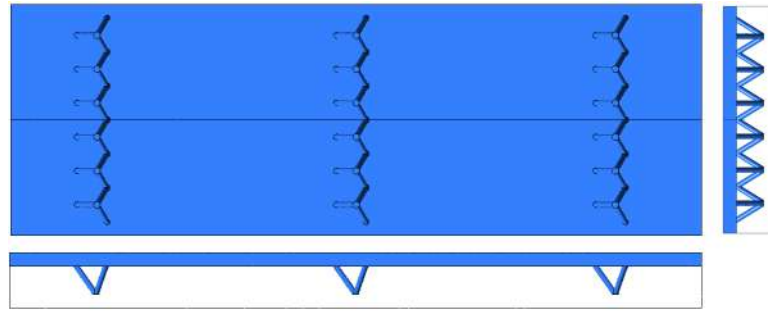
In conclusion, dimples can slightly increase thermal performance in the narrower channels at the price of a higher pressure drop. However, the adoption of this solution seems to be only marginally beneficial for the cooling jacket application.

3.5.2. Tetrahedral cells

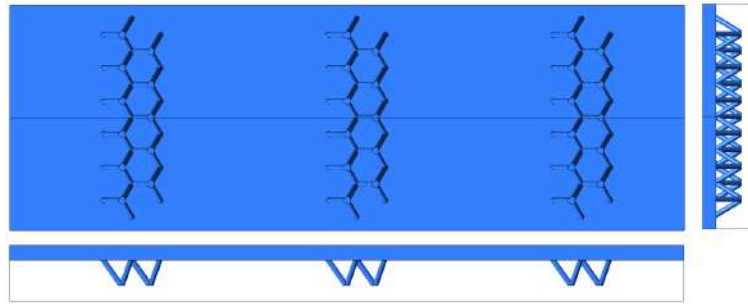
The other structure implemented in the channel to increase fluid mixing so to enhance the cooling jacket performance is the tetrahedral cell, shown in Figure 1.13a. Being an anisotropic cell, the fluid flow behaviour depends on the direction along which it encounters the cell. Referring to flow orientation nomenclature of Figure 1.13, fluid along direction B will generate a cleaner flow through the cells since there is less frontal area

blockage for the flow. On the other hand, flow along direction A will have higher pressure losses due to higher flow blockage. The fluid will be highly perturbed and favoured to flow over the cell. This greater flow perturbation could be used to increase thermal exchange in the water internal channel. For this reason, all the studied geometries will use cells along orientation A, symmetric to water flow.

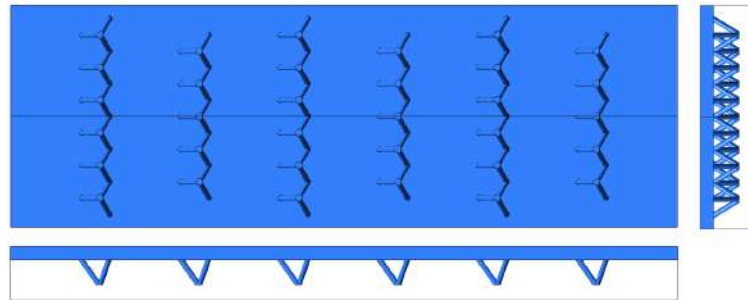
The studied geometries are reported in Figure 3.10 and Figure 3.11. In each picture is reported a top view showing cell arrangement in the channel, a side view and a front view of the channel to better see flow blockage. Figure 3.10 collects the channel configurations implementing 3 mm high cells applied in the 4,5 mm water channel thickness. Figure 3.10a shows a sector with 3 rows of cells. Its frontal area is the one offering less fluid blockage among all the studied geometries. Figure 3.10b involves 3 additional rows, half-cell offset from the original 3 rows. In this case, the frontal area blockage results higher than previous configuration. 3.10c considers again 6 rows, but now they are equally spaced.



(a) 3 mm cells in 3 rows.



(b) 3 mm cells in 6 paired rows.



(c) 3 mm cells in 6 separated rows.

Figure 3.10: 3 mm cells geometries in 4.5 mm channel.

Figure 3.11 instead refers to channel configurations having only 2 mm high cells applied in the 3 mm water channel thickness. In fact, cell dimensions have been scaled down to fit the cell rows also in the already well performing 3 mm thick water channel. Both configurations have 6 rows of cells, offset and paired two by two. Figure 3.11a is relative to cells that have the same shape, and thus relative density, of the 3 mm high cell. The scaled diameter for the 2 mm high cell is 0,4 mm. Figure 3.11b instead adopts a 0,6 mm diameter for the 2 mm high cell due to an easier AM processability. With this dimension, cell relative density increases from about 0,1 to 0,2. In the frontal view it is clearly visible how this increase in cell diameter produces a stronger flow blockage.

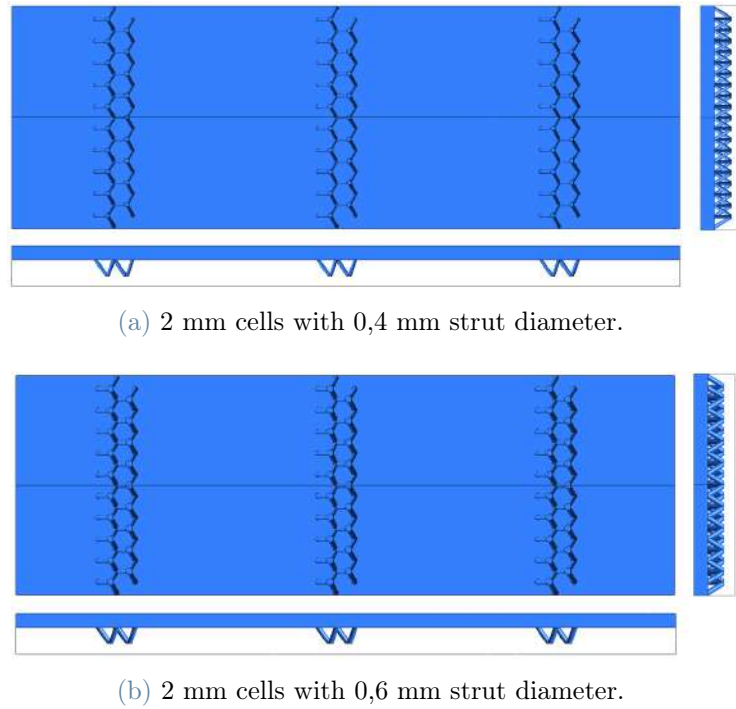


Figure 3.11: 2 mm cells geometries in 3 mm channel.

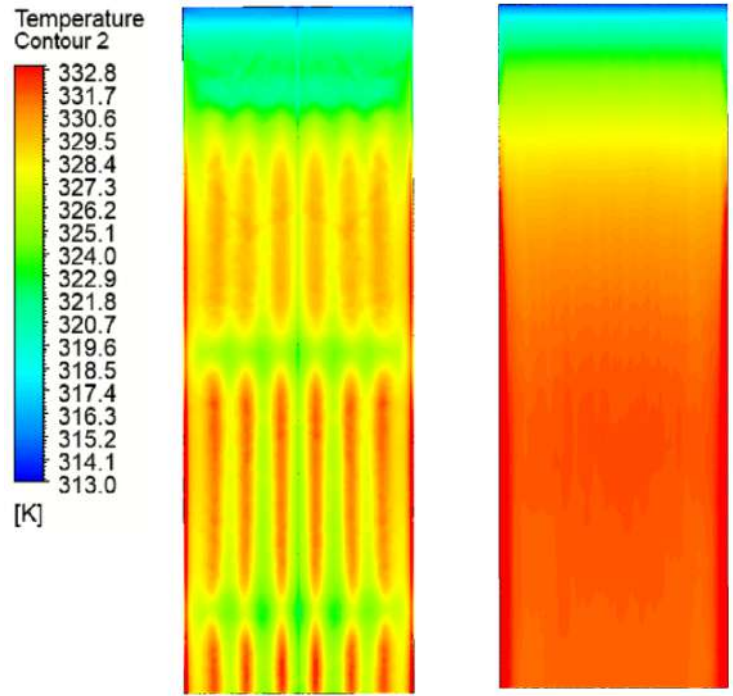
All the sectors geometries are initially modelled using Inventor, then processed using Ansys Fluent. The CFD set up steps and boundary conditions are the same as those presented in section 3.2 for the empty channel. Results of each configuration are summarised in the following sections.

3 mm high cells in 3 rows

The 3 mm cells arranged in 3 separated rows shown in Figure 3.10a is the starting point of this analysis. Each cell consists of three inclined struts with a 0.6 mm diameter. Starting from its results, the other configurations are introduced to further increase thermal performances. This geometry is suitable only for the 4,5 and 6 mm water channel, and will then be compared to the respective empty channel performances. For the numerical model, boundary conditions are again those expressed in section 3.2.

Figure 3.12 shows the temperature map on motor surface for the 4,5 mm channel with the 3 cells rows geometry, compared to the 4,5 mm thick empty water channel. From the thermal point of view, for the same channel thickness the beneficial influence of cells is evident. Flow accelerates over the cells and generates colder spots on motor surface. Due to cells shape, there is formation of faster flow lines between rows, having high heat transfer capabilities. However, between cells where there is less flow perturbation, motor

surface temperature tends to increase and becomes similar to that of the empty channel. This solution should be improved to avoid the formation of these linear hot spots.



(a) Temperature map for the 3 mm cells in 3 rows geometry. (b) Temperature map of 4,5 mm empty channel.

Figure 3.12: Influence of 3 cells rows on motor surface temperature map.

In Table 3.4 are reported the results for both channel thicknesses investigated with the 3 cells rows geometry.

Channel thickness [mm]	Water velocity [m/s]	Sector ΔP [Pa]	h [W/m^2K]
4,5	0.667	385.551	4657.12
6	0.5	172.147	3382.44

Table 3.4: Performances of 3 cells rows geometry.

Once again, a comparison in terms of performances with the respective empty channels is reported in Figure 3.13. For both channel thicknesses, the addition of cells is highly detrimental for the pressure losses due to flow distortion. However, CHTC increases due to better thermal exchange capabilities given by flow mixing and acceleration.

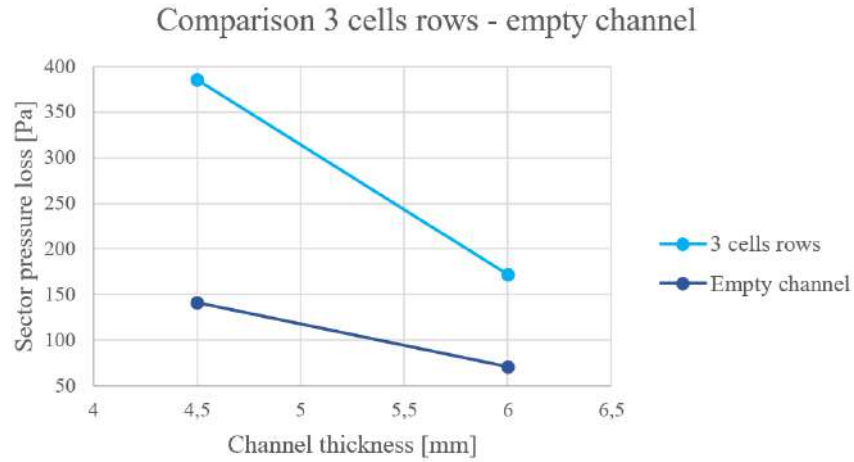
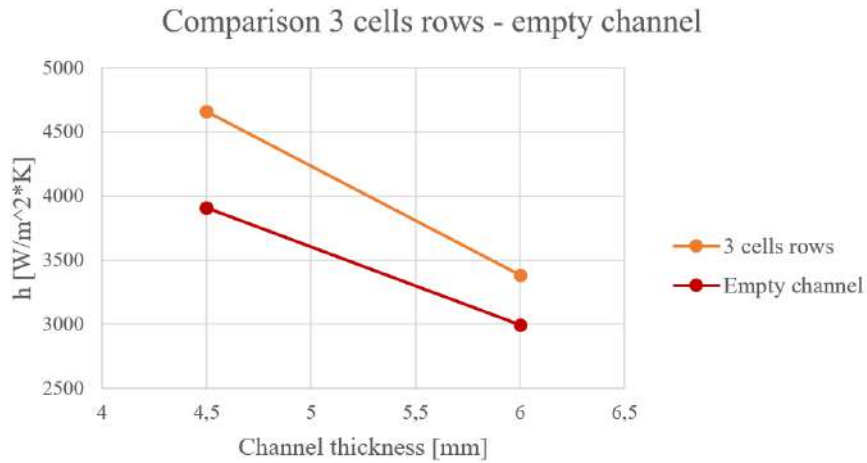
(a) ΔP - channel thickness.(b) h - channel thickness.

Figure 3.13: Comparison of empty channel and 3 cells rows geometry.

The 6 mm channel thickness with embedded cells still performs even worse than the 4,5 mm empty channel, both in terms of pressure drop and of convective heat transfer coefficient. Due to this reason, the 6 mm channel can be abandoned. From now on, 3 mm high cells will only be applied in the 4,5 mm water channel.

3 mm high cells in 6 rows

Compared to the empty 4,5 mm channel, the 3 cells rows configuration offers significant thermal management improvement. However, this solution leads to the formation of linear hot spots behind cells tips visible in Figure 3.14a. To limit this undesirable phenomenon, additional rows can be added in the channel, half cell offset from the original rows. These 3

new rows can be placed right behind the initial 3 rows as in Figure 3.10b or equally spaced from them as in Figure 3.10c. Cells in subsequent rows are not aligned to disturb fast flow lines and avoid the formation of linear hot spots. Figure 3.14 shows the temperature maps of these 3 geometries. It is immediately visible the beneficial effect on motor surface temperature of the additional rows. The linear hot spots are less severe, especially for the 6 rows paired two by two in Figure 3.14b.

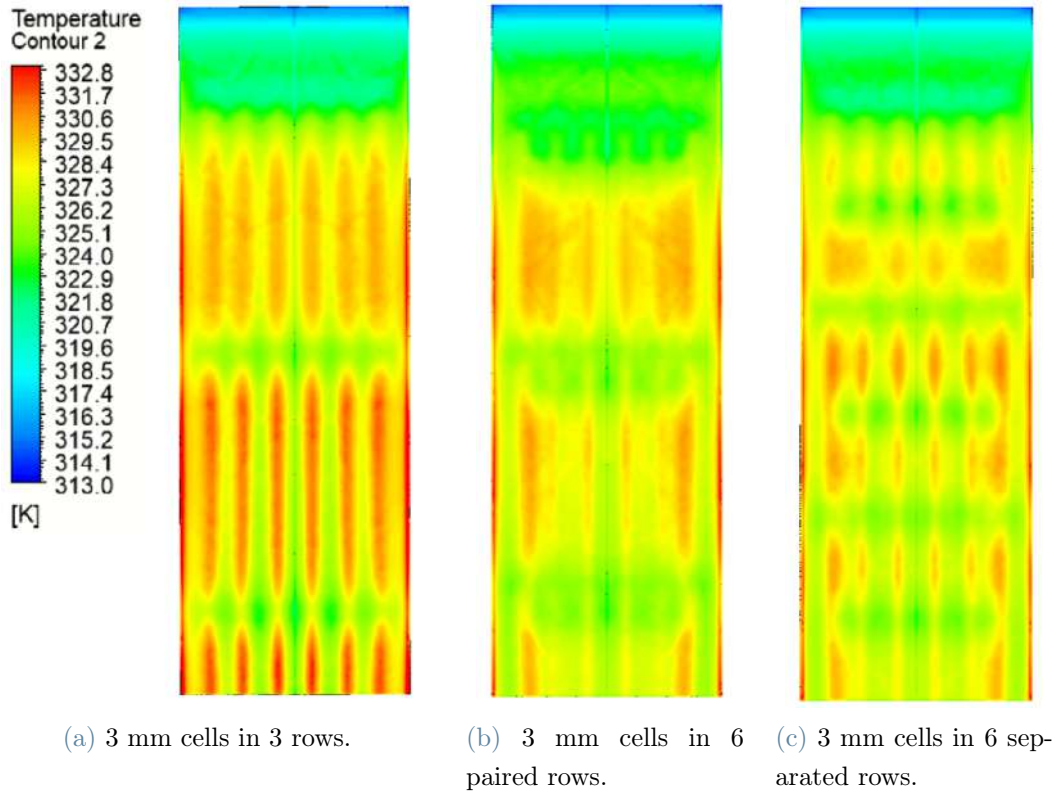


Figure 3.14: Motor surface temperature maps for the 3 mm high cells geometries.

Figure 3.15 shows the velocity profiles of the three geometries in the mid plane of the 4.5 mm thick channel. Every cell provides flow perturbation, generating vortexes behind it and flow acceleration on motor surface.

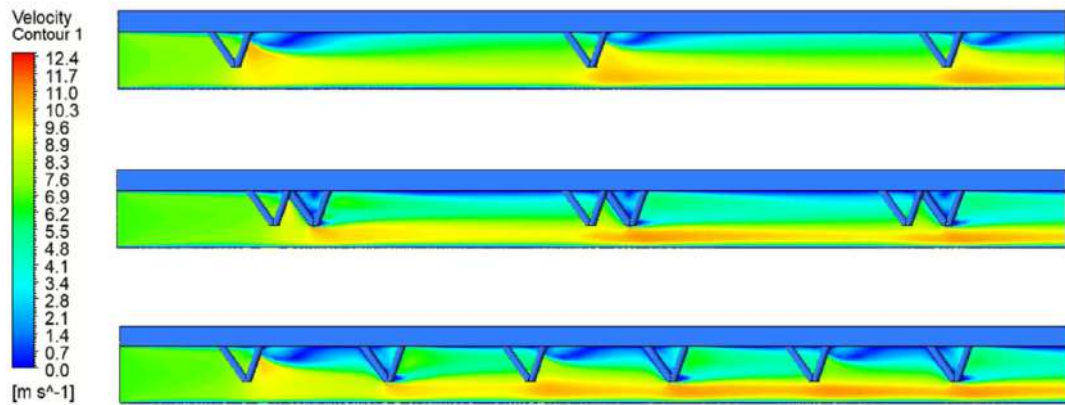


Figure 3.15: Water velocity profile in the middle of the channel for the 3 mm high cells configurations.

Table 3.5 reports results for these 3 geometries and the respective empty channel with same water thickness. The application of cells favours convective heat transfer, but increases pressure loss. In addition, the 6 cells rows provide improvements in terms of heat removal capabilities compared to the 3 rows solution, at the price of higher pressure drop due to important flow blockage.

Channel geometry	Sector ΔP [Pa]	h [W/m^2K]
4.5 mm empty channel	141.445	3906.16
3 mm cells in 3 rows	385.551	4657.12
3 mm cells in 6 paired rows	537.420	4955.56
3 mm cells in 6 separated rows	522.015	4946.32

Table 3.5: Comparison of 3 mm high cells geometries in 4.5 mm high water channel.

In conclusion, evaluating both qualitative and quantitative results, the solution with 6 rows of cells paired two by two gives the best compromise in terms of pressure loss, thermal performance and hot spot control for the 4.5 mm high water channel.

2 mm high cells in 6 rows

Being the 6 paired cells rows an interesting solution, it has been investigated also for the 3 mm high water channel with 2 mm high cells. Two different types of cell have been studied: one that keeps the previous strut diameter of 0.6 mm shown in Figure 3.11b and one that scales down the diameter to 0.4 mm reported in Figure 3.11a. Due to higher diameter, the first cell geometry is easier to manufacture but will give higher blockage to

the fluid flow. On the other hand, a lower diameter leaves more free frontal area to the incoming flow, but it will be more difficult to produce. This last cell geometry will have the same relative density of the 3 mm high cell with 0.6 mm strut diameter.

Figure 3.16 reports the motor surface temperature maps of the 2mm high cells geometries. It is clearly visible how the thicker struts cells can better promote the thermal exchange, even though there is formation of lateral hot spots, probably due to lateral wall boundary conditions.

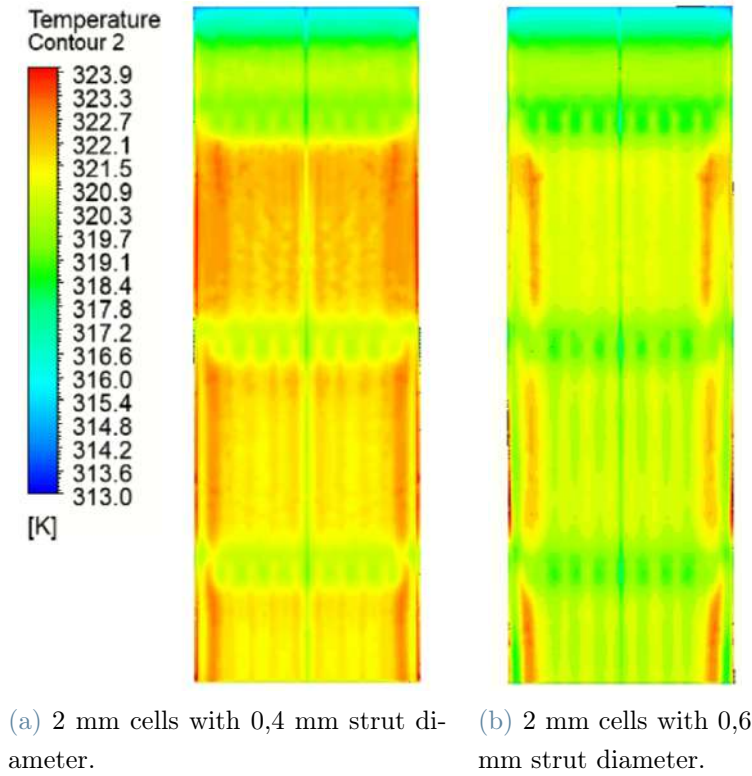


Figure 3.16: Motor surface temperature maps for the 2 mm high cell geometries.

Table 3.6 shows quantitative results for these two geometries, compared with the empty channel with same water thickness. Cells can indeed enhance heat convection from hot motor surface, but pressure losses deeply increase compared to the empty channel.

Channel geometry	Sector ΔP [Pa]	h [W/m ² K]
3 mm empty channel	392.845	5787.18
2 mm cells 0.4 strut diameter	1465.320	8008.45
2 mm cells 0.6 strut diameter	2069.790	9049.37

Table 3.6: Comparison of 3 mm high water channel with 2 mm high cells geometries.

3.6. Final comparison

The following graph in Figure 3.17 summarises the results of the most interesting studied solutions. The optimal area for performances in the comparison graph is in the bottom right-hand corner, where high heat transfer capability and low pressure loss solutions lay. As discussed in section 3.5.1, the effect of dimples is too marginal, no significant performances variations were observed, so they have not been reported. Moreover, all the 6 mm water channel geometries offered too low convective heat transfer coefficient and were therefore discarded.

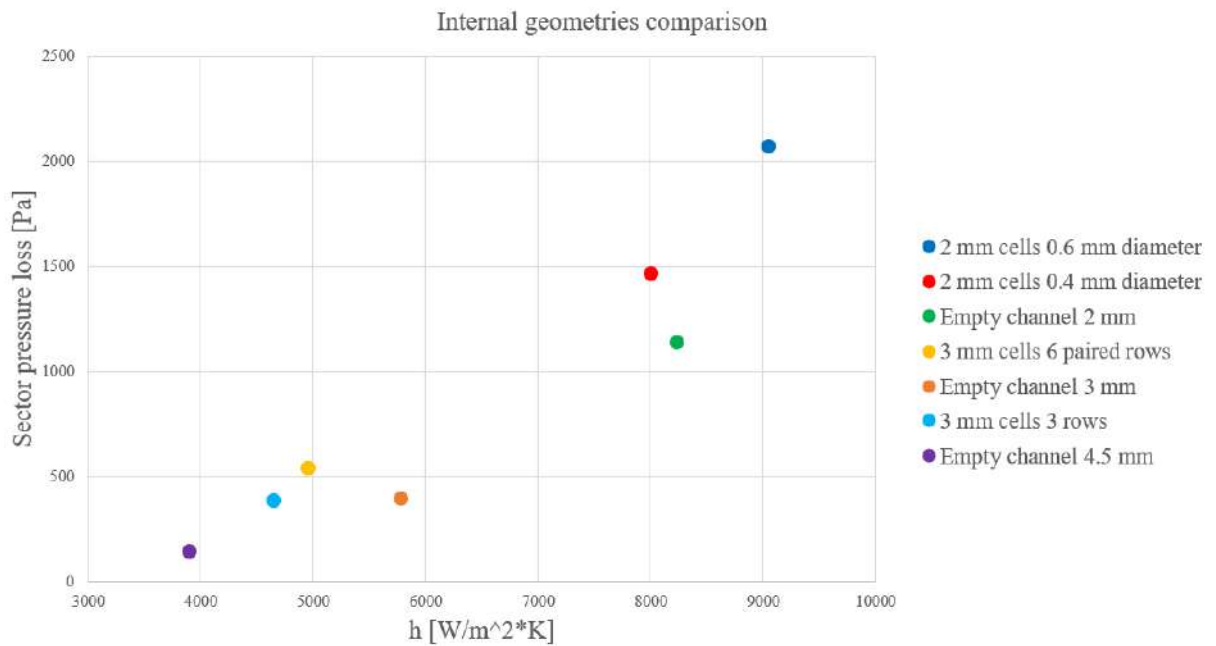


Figure 3.17: Comparison of internal water channel geometries.

The solutions that seem to offer the best compromise between the pressure drop of the flow in the channel and convective exchange with the motor wall are:

- 2 mm high empty channel.
- 3 mm high channel with 2 mm high tetrahedral cells with a strut diameter of 0.4 mm.

The overall best solution appears to be the first one, adopting a 2 mm high water channel. To obtain such channel, it would be necessary to manufacture on the internal side of the shell a separation wall protruded 2 mm from the internal wall of component single shell. This wall, initially represented in Figure 3.2, runs in an helical path in the gap between the single shell and the motor surface and confines the water flow.

The second best performing solution involves a 3 mm thick water channel with 2 mm high tetrahedral cells having $400\ \mu\text{m}$ struts diameter. Such low diameter cells would be difficult to produce and final result could differ from the modelled one in terms of geometry and thus performances. Moreover, as-designed cells presented in Figure 3.11a are not directly manufacturable due to exceeded 45° critical angle and would need a significant re-design.

Concluding, the internal channel configuration selected for the cooling jacket is the 2 mm high empty channel.

3.7. Re-design for LPBF

The 2 mm high empty channel that helically envelops the motor is guaranteed by a thin wall manufactured on the internal side of the component single shell, as represented in Figure 3.18a. The curved wall represents a section of the single shell, with separation walls running helically in the internal part. Considering the component axis as the build direction for the LPBF process, this separation wall protrudes almost horizontally, thus exceeding the 45° critical angle. It needs a slight re-design to be manufactured, for example adopting a chamfer on the lower face or a trapezoidal cross section wall. Figure 3.18b shows a possible wall cross section re-design.

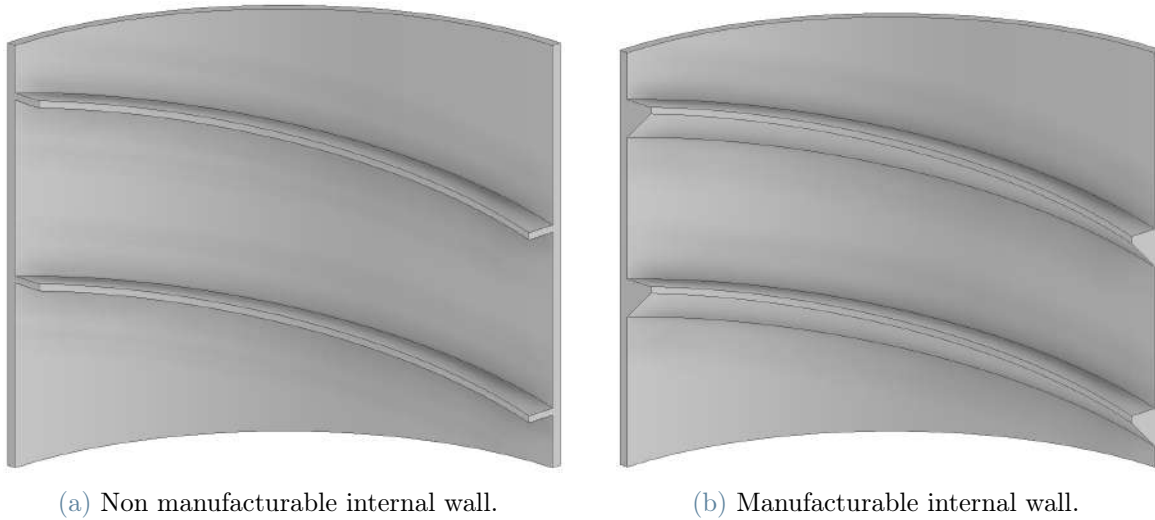


Figure 3.18: Re-design of internal cooling channel helical wall.

The local thickness variability of vertical walls produced by LPBF is usually limited between $+0$ and $50\ \mu\text{m}$ from the nominal desired value. The single shell wall could be affected by this variation which would locally affect the water channel thickness, leading to different unpredictable performances of the component. However, being the possible

thickness variation so small, this phenomenon is neglected.

4 | External geometry design

4.1. Introduction

After having studied the internal geometry, the second design objective is to develop an effective external fin arrangement to have a beneficial heat rejection from the cooling jacket to the external ambient air. In fact, all the four cooling jackets of the vehicle are not covered by the car body and are therefore subjected to ambient air flow. The external fin solution adopted by Dynamis is clearly visible in Figure 2.1. The Team numerically demonstrated the thermal benefits of fins compared to a basic solution with no fins. Fins confer a great enhancement of heat rejection at any relative external air velocity, at the cost of additional weight. From their velocity maps of air around the cooling jacket, it is visible how the component completely diverts the fluid flow generating very low velocity region behind itself. Rear fins interacting with almost stationary air contribute less to heat transfer than frontal fins impacted by fast air flow.

The following analyses want to first obtain results for the jacket with no fins to check model correctness in comparison to the Dynamis results. Then, four different external fins configurations have been obtained by applying again lattice structures. The idea is to take advantage of cells porosity to convey air flow and deliver it to rear part of the jacket. In this way, the rear fin contribution to heat transfer will be more effective. Solutions are tested at different relative air velocity and compared in terms of heat rejection capabilities and additional weight.

4.2. Numerical model

The numerical analyses relative to the external cooling jacket geometries consist of a fluid flow interacting with a heated cylindrical solid domain. The fluid domain surrounds the solid model in all directions to be able to simulate the diverted air around the component. Exploiting axial and radial symmetries, the whole cooling jacket and air behaviour can be described by studying only 1/4 of the whole domain. A representation of this reduced model with its boundary conditions is reported in Figure 4.1. The blue part represents

the single shell aluminium solid wall of the cooling jacket, which is 1.5 mm thick. It corresponds to the solid wall of the internal channel planar section shown in Figure 3.2. It separates the internal heated water channel from the environment. Heat is in fact introduced in the model at the water - solid interface. Following Dynamis advices, this interface is set at a constant temperature of 333 K. This temperature is different from those seen in the internal channel analyses. The goal of this simulations is not to combine internal and external behaviour, but to have a comparison between different external geometries. The heat will propagate by conduction in the solid and finally will be rejected to ambient by convection. Air enters the fluid domain at 303 K at varying velocities. This parameter is the relative velocity between ambient air and the cooling jacket. Since backflow can occur in the fluid domain, the outlet backflow temperature is set at 303 K. The top wall and the side wall have been set as symmetry planes to avoid the no slip condition, which is the zero velocity condition of a fluid against a solid wall. The external diameter of the aluminium shell, considering a 3 mm thick internal water channel, is 105 mm while the axial length, considering symmetry, is 60 mm. The fluid domain extends for 120 mm in axial direction, 150 mm in height and 300 mm along flow direction. These dimensions are those used by Dynamis to have a better comparison with their results.

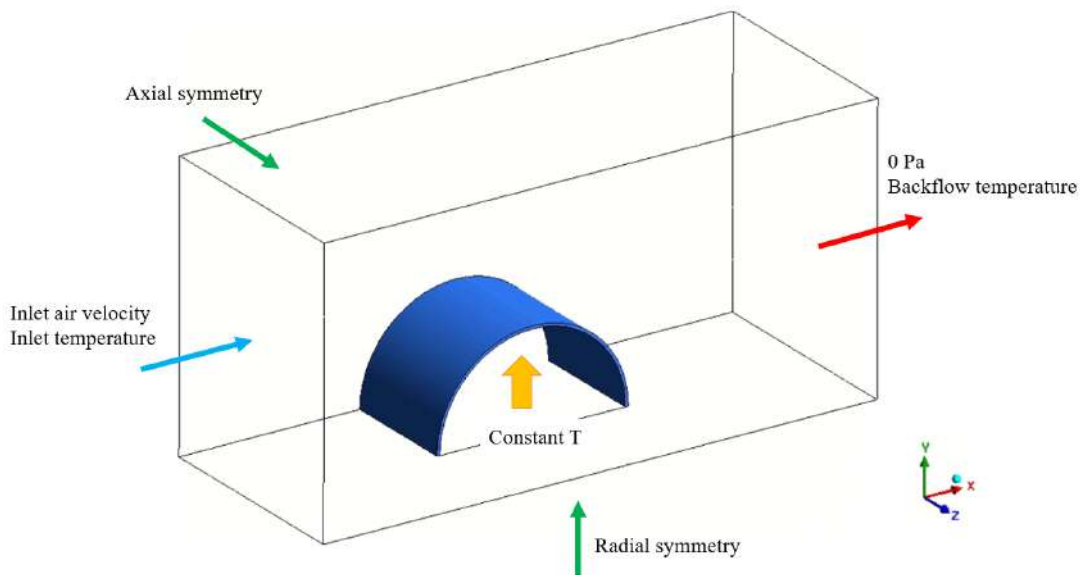


Figure 4.1: Numerical domains of jacket with no external fins.

The solid parts have been modelled using Inventor and exported as STEP files. The fluid domain was then added in SpaceClaim module on Ansys Fluent from Workbench. Once fluid and solid domains are defined, the meshing step is performed with Fluent Mesher using the Watertight workflow. For this geometries, this meshing procedure was

able to generate a higher quality mesh compared to the the mesher used for the internal channels. Also in this case it is important to have a fine mesh for the solid part to properly describe conduction. Mesh in the fluid domain instead must describe heat convection and interaction with the solid part. Inflation layers were used to capture the gradients of velocity, temperature and pressure of the fluid in contact with solid walls. As explained in section 3.2, mesh quality is checked also through the y^+ value and refined when needed trying not to exceed computational capabilities.

From this step, analyses are similar to those of the internal water channel. The mesh is uploaded to the same solver used before. The Energy model and SST k - ω model are activated. Material properties are assigned to air and aluminium domains. Boundary conditions for inlet, outlet, heat source wall, symmetry walls and air - solid interface are defined. The surface roughness is set at 10 μm for solid walls in contact with the fluid flow. The analyses are initialised and solution can be run. Results are obtained and visualised in the post processor software. The comparison of different solutions is made in terms of:

- Convective heat transfer coefficient from the heated solid to the air flow. It is defined as:

$$h = \frac{\dot{q}}{T_{surface} - T_{ref}} \quad (4.1)$$

It depends on the heat flux \dot{q} through the solid - air interface, which is the thermal power transferred to the fluid over the interface surface extension. It also depends on the temperature difference between unperturbed fluid flow T_{ref} and the interface temperature $T_{surface}$. In these analyses, the heat flux \dot{q} is now a variable of the problem. Since in these analyses it is imposed a constant temperature boundary condition on the solid - water interface and not a constant heat flux as before, the more a geometry is able to dissipate thermal power with the environment, the more heat must flow through the solid to keep the inner boundary temperature constant. The better a solution, the higher will be the needed \dot{q} and the higher will be h . $T_{surface}$ is again a variable of the problem which depends both on conduction and convection effects. A high average surface temperature means that there is good heat conduction in the external fins, but convective heat transfer capabilities are less effective. This is characteristic of thicker fins, where the heat propagation in fin core is less influenced by fluid - solid interface. On the other hand, a lower $T_{surface}$ means a convection heat transfer prevailing on conduction. The heat is not able to fully propagate for conduction in all the external fins since it is early transferred to

air for convection. This is typical of thin long fins. The convective heat transfer coefficient comparison tells which solution, for the same interface area, is the best one in promoting heat convection from the solid to ambient air. It can be seen as an effectiveness coefficient for the external fin geometry.

- Total thermal power rejected to environment. This is an absolute value for comparison of the different solutions. It is calculated as:

$$Q = \dot{q}A_{interface} \quad (4.2)$$

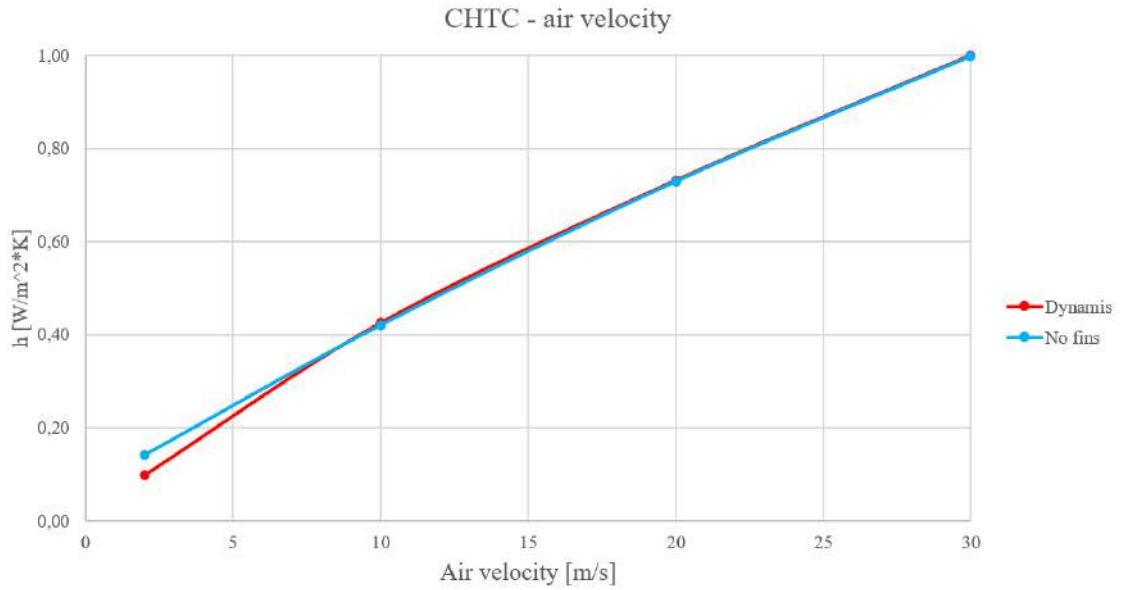
where \dot{q} is the heat flux through the solid - air interface and $A_{interface}$ is the solid - air interface area extension. The higher this value, the more heat is transferred from the cooling jacket to the environment.

- Additional mass of external fins compared to the smooth solution with no fins. The objective is to find a geometry that provides good thermal management with additional mass as low as possible.

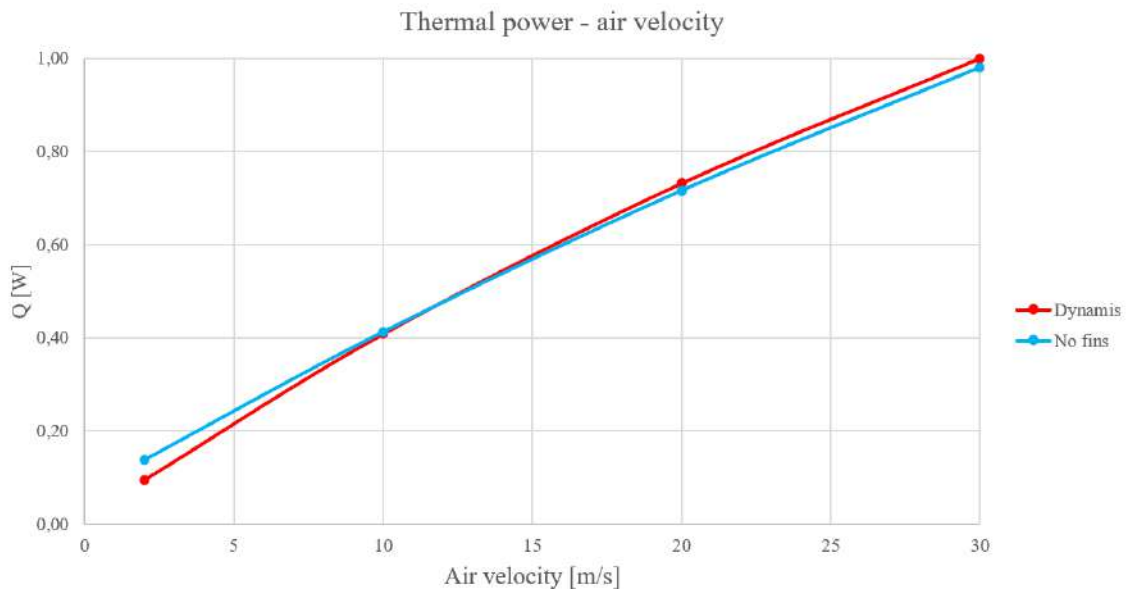
4.3. Jacket with no external fins

As a starting point, the smooth jacket with no external fins is studied at different relative air velocities. Input air velocity varies from 2 to 30 m/s to simulate the different operating conditions of the vehicle. The model used for these simulations is the one shown in Figure 4.1.

Results in terms of convective heat transfer coefficient and thermal power rejected to environment are respectively reported in Figure 4.2a and Figure 4.2b. Obtained values are compared with Dynamis simulations results of the cooling jacket with no external fins. As a matter of secrecy, quantitative results are not directly reported. The comparison is presented in relative terms, having normalised all the values by Dynamis maximum value. Both the convective heat transfer coefficient and the thermal power dissipated to environment have a linear trend with air velocity. As the results are very similar to those of the Dynamis Team, the model is considered reliable and correct.



(a) Convective heat transfer coefficient - air velocity.

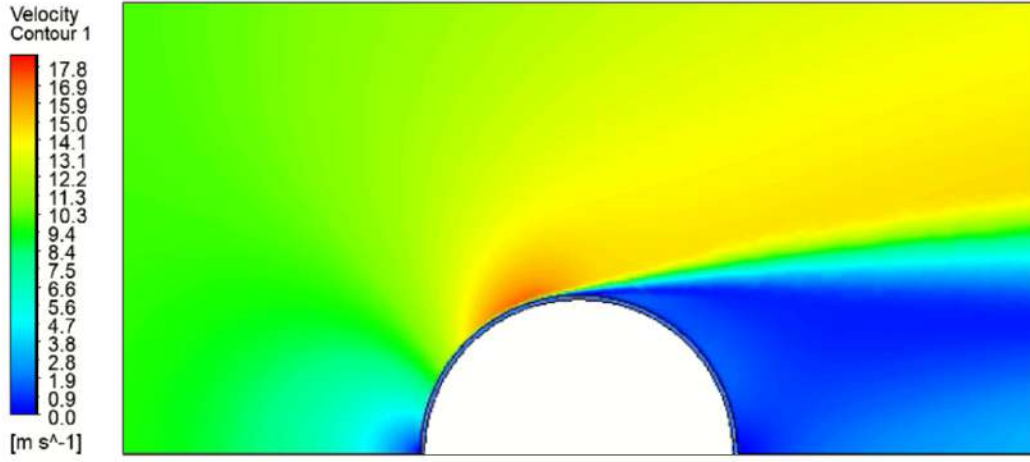


(b) Thermal power - air velocity.

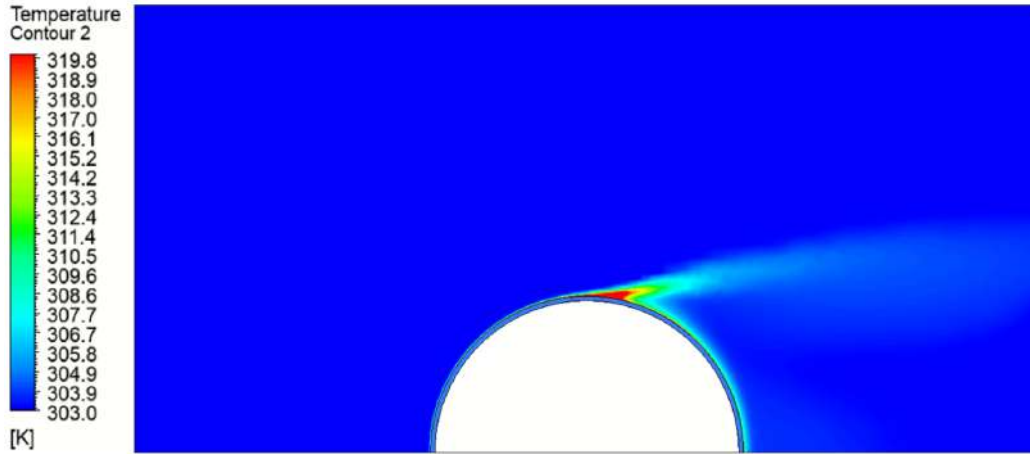
Figure 4.2: Performances of jacket with no fins at different air velocities.

Figure 4.3 shows the velocity and temperature maps at the axial symmetry plane for cooling jacket with no fins with a air velocity of 10 m/s. The white semi-circle in the figures is where the electric motor is positioned inside the cooling jacket. It is evident how the air in the rear part of the cooling jacket has extremely low velocity and there is formation of a vortex due to backflow. This extended low velocity limits the effectiveness of fins placed in the back part of the component. The temperature map shows the limited air volume that is heated by adopting a cooling jacket with no external fins. This is due

to low interface area extension and low interaction with the fluid flow.



(a) Velocity map.



(b) Temperature map.

Figure 4.3: Velocity and temperature maps for 10 m/s air velocity on jacket with no fins.

4.4. Implementation of enhancing techniques for the external geometry

The idea now is to apply lattice structure geometries on the external part of the jacket to increase the thermal power rejected to the environment. The more heat is dissipated at this stage, the less workload is entrusted to the liquid - air radiator downstream in the cooling circuit. The whole cooling system would be less stressed, could also be lighter and the electric motors would work more efficiently. By exploiting LPBF capabilities, it could be possible to design a fin system potentially more effective than the one shown in Figure 2.1, which adopts classical rectangular fins. Lattice structures in fact could

offer a high interaction with the fluid flow in terms of mixing, turbulence promotion and increased solid - air interface surface. These elements, as expressed in section 1.4, are responsible for better convective heat transfer performances. The adoption of performance enhancing structures for the external geometry is substantially different compared to their implementation for the internal channel described in section 3.5. In this case, the lattice structures are not only used as turbulence promoters, but they are directly in contact with the heat source. This is highly beneficial for thermal performance since structures can conduct the heat from the solid jacket shell to the outer part of cells and largely extend the heat transfer area. Moreover, porous structures would allow the fluid to directly flow through heated fins and possibly better interact with the rear part of the cooling jacket when coupled with a air diverter wing.

4.4.1. Tetrahedral cells

CFD analyses of entire model

The tetrahedral unit cell is once again studied due to its simple yet effective geometry. They have been designed radially all around the cooling jacket, placed according orientation B as shown in Figure 1.13. This cell positioning allows a cleaner and faster flow through the cells, which is beneficial for heat transfer. Kim et al. [31] suggest that the best cell porosity considering only heat transfer and neglecting pressure losses is 0.8. This value allows for a good compromise between flow acceleration and limitation of dead flow regions behind the struts. Imposing a cell height of 10 mm, the 0.8 porosity is obtained with a strut diameter of 2 mm. With these cell dimensions, it is possible to place 24 cells on the radial direction and 8 parallel rows in axial direction. However, cells by themselves are not enough to direct the flow in the rear part of the jacket so to involve the back fins in heat transfer. An additional 1 mm thick wing is designed to divert the air flow to the rear part of the jacket. The solid model of this component used for the simulation has been made with Inventor and it is reported in Figure 4.4. It already exploits both axial and radial symmetries.

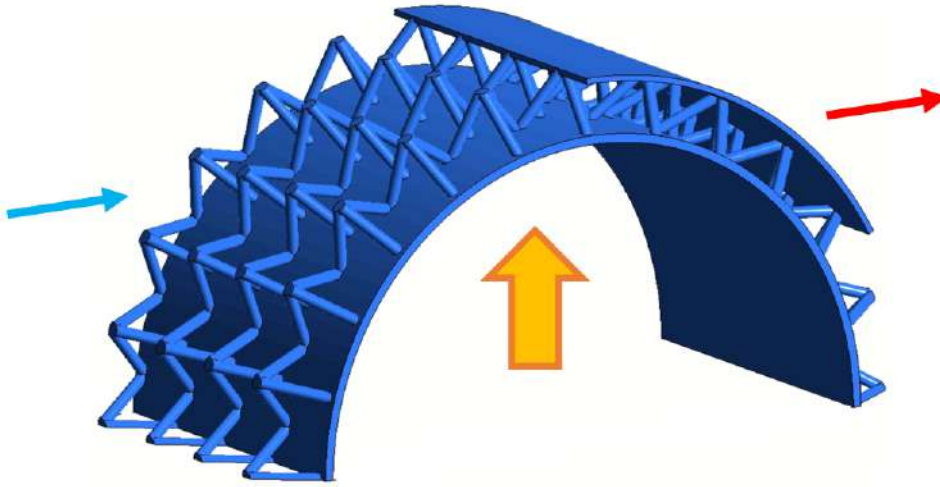


Figure 4.4: Tetrahedral cells fins with wing.

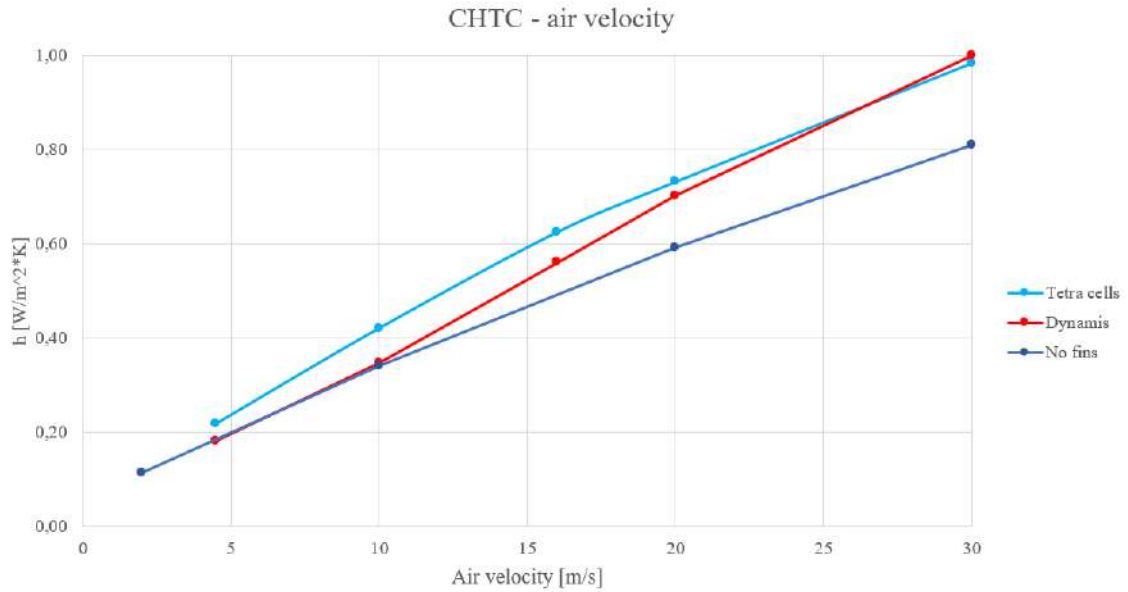
The numerical procedure followed for these analyses is the same as those for the cooling jacket with no fins explained in section 4.2. Simulations have been run for different velocities.

Comparison with Dynamis results

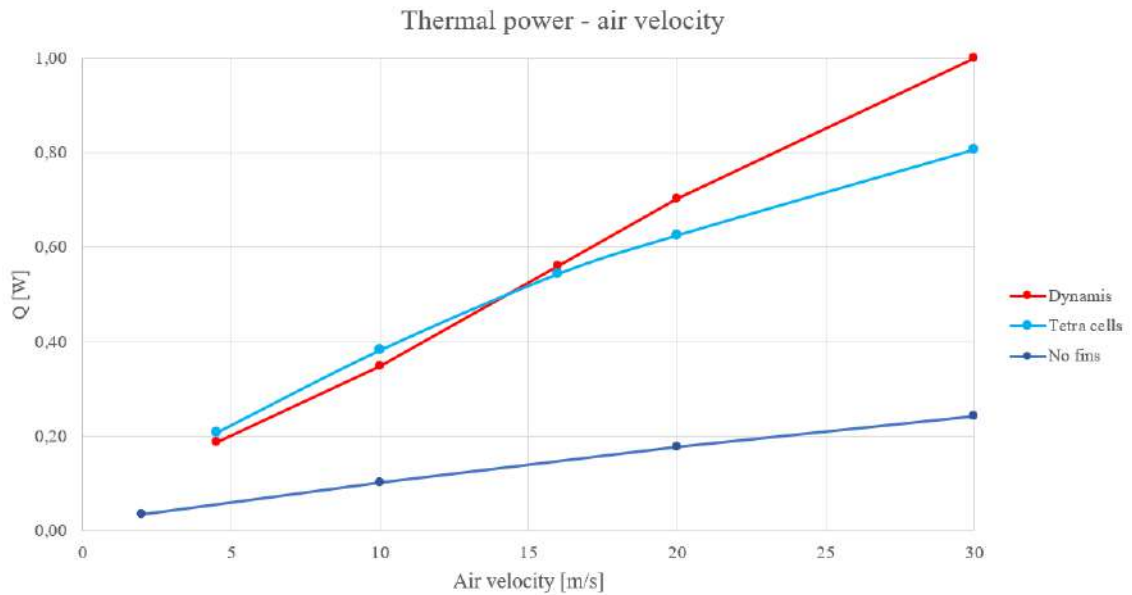
Figure 4.5 shows tetrahedral cells fins with wing results compared to Dynamis solution and to the smooth cooling jacket with no fins. As a matter of secrecy, quantitative results are again not directly reported. The comparison is presented in relative terms, having normalised all the values by Dynamis maximum value. The convective heat transfer coefficient provided by the tetrahedral cells geometry, expressing the effectiveness of promoting convection heat transfer at equal heat transfer area, results improved at any studied velocity compared to solution with no fins. Moreover, the rejected thermal power, which also depends on the air - solid interface extension, is much higher for the solution with cells. Tetrahedral cells with wing geometry proved to be highly beneficial for heat transfer performance enhancement from the component to the environment compared to the solution with no fins.

Comparing the tetrahedral cells solution to Dynamis results, the convective heat transfer coefficient appears higher at almost any velocity. However, the total thermal power rejected is lower at higher velocities. This is probably due to a Dynamis solution's heat transfer area which is 30% higher than that of tetrahedral cells geometry. For comparable thermal performances, the solution with tetrahedral cells and wing allows a significant fins weight reduction of 45.6%, beneficial for dynamic performances of the car. Therefore, these results show a promising perspective in adopting lattice structures as a replacement

of more classical fin arrangements.



(a) Convective heat transfer coefficient - air velocity.

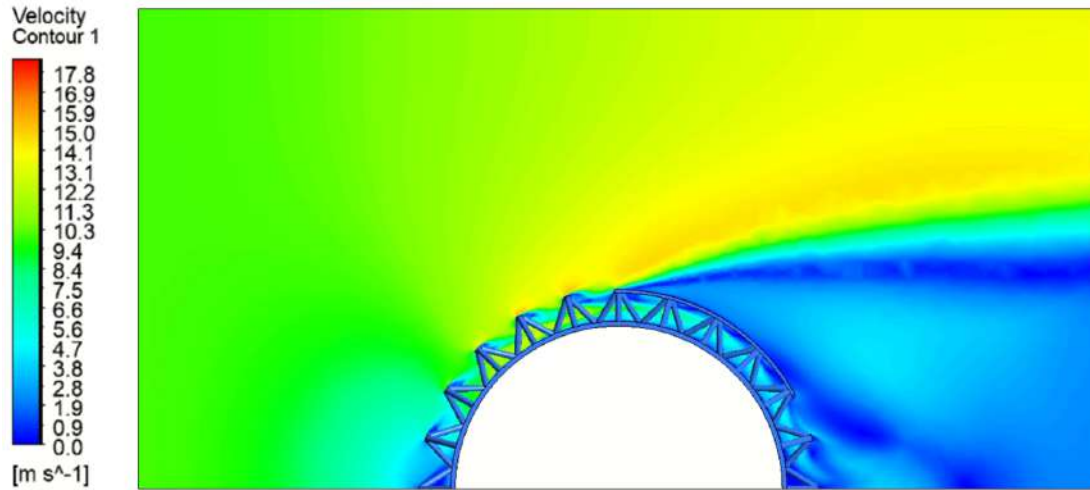


(b) Thermal power - air velocity

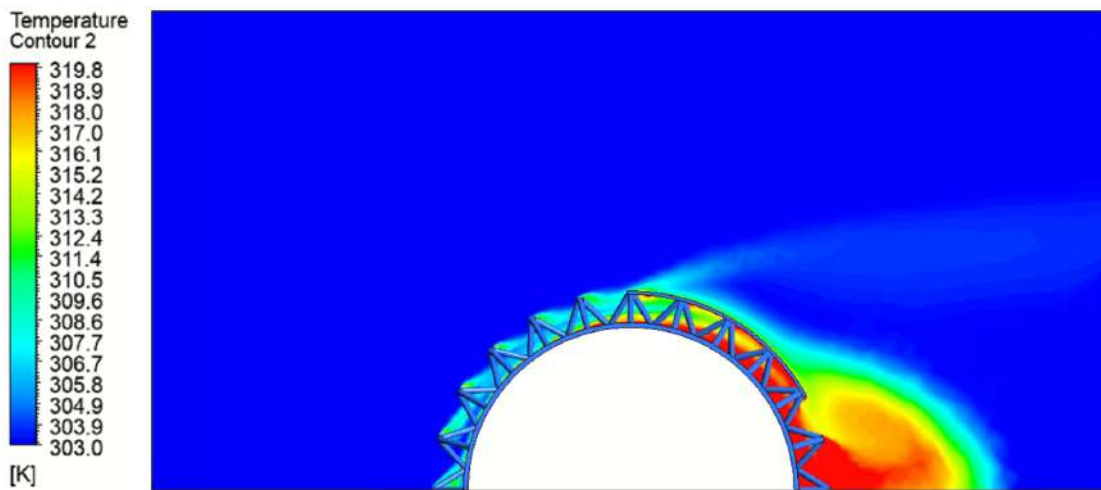
Figure 4.5: Performance comparison between tetrahedral cells and smooth jacket.

Figure 4.6 shows the velocity and temperature maps for 10 m/s air velocity on jacket with tetrahedral cells fins and wing. Both maps have the same scale ranges of those relative to the smooth cooling jacket with no fins in Figure 4.3 to allow a direct qualitative comparison of the two geometries. These maps are plotted on a plane parallel to axial symmetry plane, offset of 6 mm so that it crosses the center of the most internal row of

cells. The velocity map shows how the flow accelerates between the first cells encountered. Due to the wing, the flow is diverted and directed as desired to the rear part of the jacket. The temperature map shows the convection of heat from the solid heated parts to the air. With this geometry it is evident the increase in the amount of air that has been heated by the cells. The rear part of the jacket in this case is able to effectively take part of the heat transfer process.



(a) Velocity map.



(b) Temperature map.

Figure 4.6: Velocity and temperature maps for 10 m/s air velocity on jacket with tetrahedral cells fins and wing.

Fluid mechanic analysis

It is now possible to perform a fluid mechanic analysis of the component using the "Static structural" software in Workbench, setting as loads the pressure and temperature distribu-

tions found from the previous fluid dynamic analyses. This analysis allows to understand intensity and direction of stresses and deformations in the component during service condition, highlighting possible weak spots that should be improved. First the STEP model has been imported on the software, then the mesh, loads and boundary conditions are set. A fine volumetric mesh is defined to properly capture the component behaviour. The loads that have been used are relative to the most critical service condition, with the relative air velocity at 30 m/s. The pressure load is determined by the ambient air flow impacting the cooling jacket. From the "Solution" step in Ansys Fluent, it is extracted as a pressure map on the solid - air interface surface and directly linked to the mechanical analysis. The software recognizes the surface compatibility and applies the pressure load to the mechanical model. The pressure map on the solid is shown in Figure 4.7. The most solicited part is the frontal impact area, where there is stagnation and deflection of the incoming air flow.

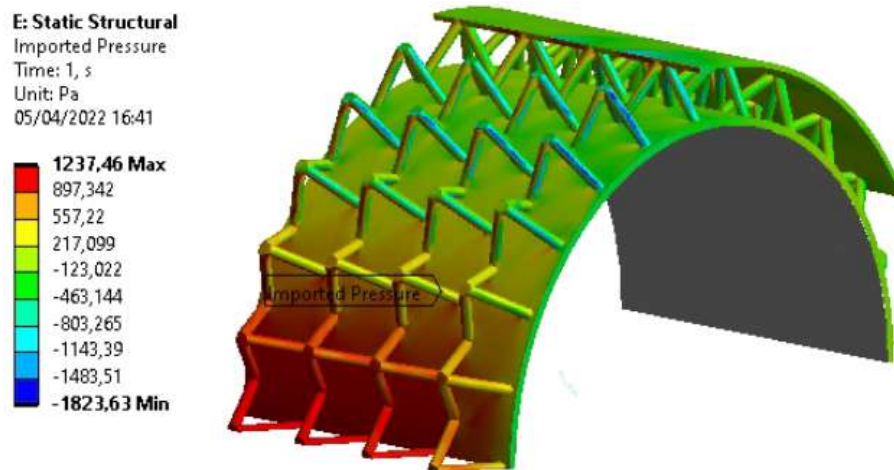


Figure 4.7: Pressure map on interface.

The thermal load instead has been exported from the Fluent post processor as a volumetric distribution of temperature. The file has been prepared using Excel and imported into the mechanical simulation. Once again, the software recognizes the volume compatibility and assigns the temperature distribution to the material points of the model. The temperature distribution in the solid is shown in Figure 4.8. The hottest part is the solid single shell, directly in contact with the heat source. Heat propagates by conduction in the cells struts and transfers to the air flow by convection.

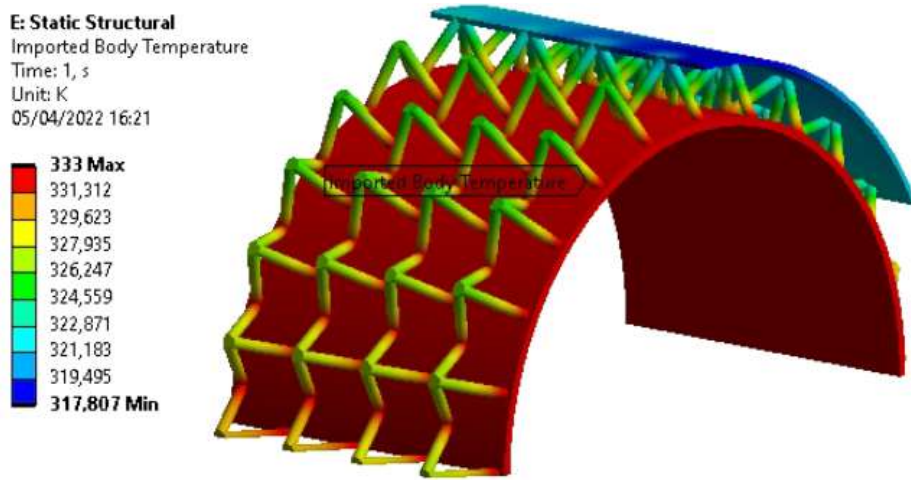


Figure 4.8: Temperature distribution in the solid.

Boundary conditions are shown in Figure 4.9 and consist of axial and radial symmetries as for the fluid dynamic analyses. The additional boundary condition is the shell face set as lateral guide to simulate the axial constraint of the jacket. The component cannot expand axially but it is free to expand radially. This boundary condition gives an overestimation of the axial confinement. In fact, on the wheel side the jacket is fixed to the motor group with a bolted flange, while on the other side it is slightly free to expand due to a plastic gasket connecting the motor with the jacket itself. This is not a rigid connection and allows limited axial movement of the jacket. However, it should be limited to avoid any possible water leakage. On the external side, the wing is free to expand axially. No boundary conditions are directly applied to the struts.

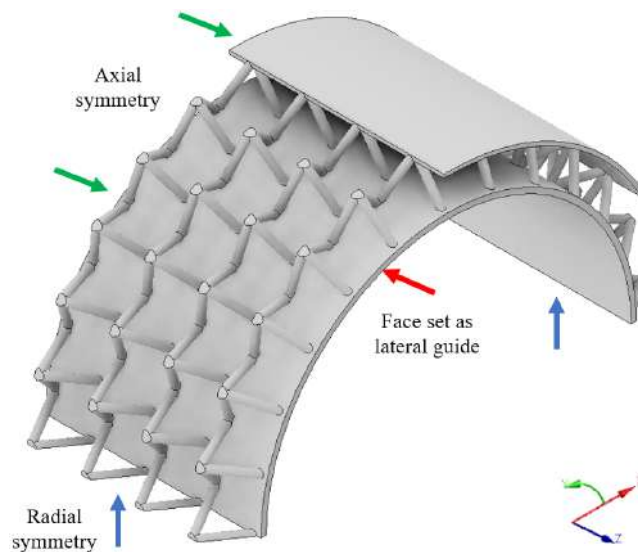


Figure 4.9: Boundary conditions for the fluid mechanic analysis.

Figure 4.11 shows the equivalent stress of Von Mises plotted for the component. The Von Mises equivalent stress is a combination of the stress tensor components and it is used for preliminar static assessments. For a general stress tensor, it is defined as:

$$\sigma_{VM} = \sqrt{\frac{(\sigma_{xx} - \sigma_{yy})^2 + (\sigma_{xx} - \sigma_{zz})^2 + (\sigma_{yy} - \sigma_{zz})^2 + 6(\tau_{xy}^2 + \tau_{xz}^2 + \tau_{yz}^2)}{2}} \quad (4.3)$$

While if the coordinate system coincides with the principal reference frame, the definition becomes:

$$\sigma_{VM} = \sqrt{\frac{(\sigma_I - \sigma_{II})^2 + (\sigma_I - \sigma_{III})^2 + (\sigma_{II} - \sigma_{III})^2}{2}} \quad (4.4)$$

The most stressed part is the shell due to its axial constraint, with an average equivalent Von Mises stress of 65 MPa. The wing appears to be more stressed at the centre of the component, where the axial symmetry boundary condition is imposed. The average equivalent stress there reaches a peak of 20 MPa and it decreases in the direction of its free end. No direct boundary conditions have been imposed to the struts, so they have more freedom to expand and deform. For this reason, they have the lowest value of Von Mises stress around 10 MPa. However, at the base of the central struts there are some highly stressed spots. This is both due to the influence of proximity to the boundary condition and to the absence of fillets. Round fillets were not designed to ease the CFD analyses, but they will be required in the final CAD design.

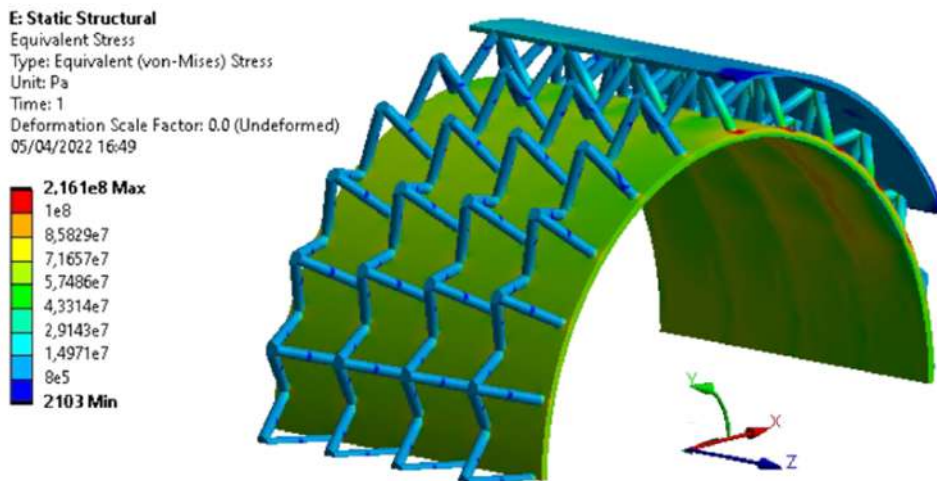


Figure 4.10: Von Mises stress of the tetrahedral cell cooling jacket.

Since the component is reacting in the elastic field, the effect of the two applied loads

can be separated and studied independently. It turns out the almost the totality of the equivalent Von Mises stress is due to the thermal expansion confinement. The pressure load is responsible for about the 0.8% of the total Von Mises stress.

However, the problem of the Von Mises stress is that it does not tell which are the prevailing stress components in the stress tensor and their direction. To understand this, the individual components of axial, radial and circumferential stress have been plotted according to a cylindrical reference frame. Figure shows the axial stress (along Z axis), which is the most intense stress component of the stress tensor. In the shell it reaches an absolute value close to 65 MPa in compression, which is coherent with what expected due the axial constraint. Looking at the radial stress, it seems that the struts are subject to bending. It could be due to how they are constrained to the shell and how they connect to each other at the top of the cell. The coldest parts of the component are cells tops and the wing

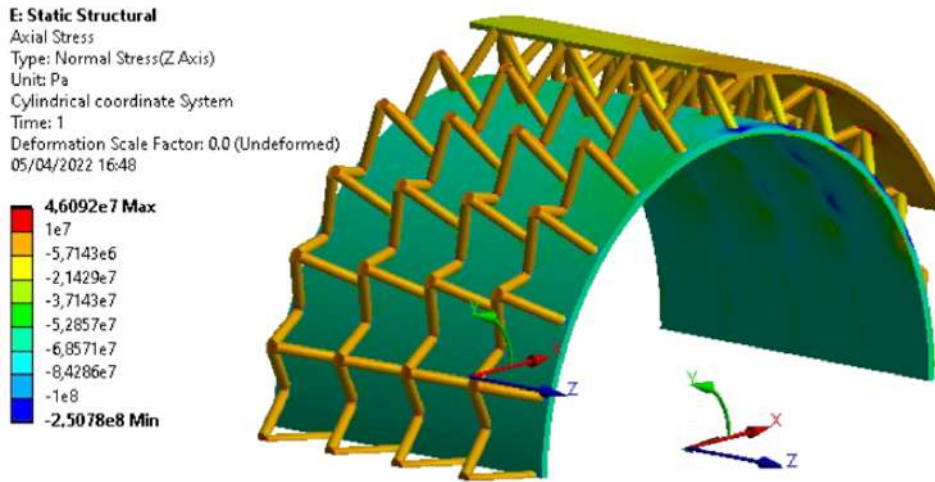


Figure 4.11: Axial stress of the tetrahedral cell cooling jacket.

Considering the mechanical properties of Aluminium presented in section 1.2, these stresses are not a problem for the static assessment of the component. The maximum Von Mises stress is in fact significantly lower than the material yield strength. However, further studies must be carried out to understand thermal fatigue of the component and the effect of vibrations during service conditions.

4.4.2. Octet cells

Geometry definition

The major concern of the solution with tetrahedral cells is that, having scaled the cells so large, they lost the concept behind a lattice structure and became an embedded truss or frame structure. The dimensions of the unit cell of lattice materials should be in the scale of millimeters if not micrometers [35]. To truly address the cooling jacket heat rejection problem with a proper lattice structure, a new geometry with smaller unit cells have been tested. The new structure unit cell is the combination of one Octet cell and eight simple cubic cells. A single cubic cell has an edge of 5 mm and a strut diameter of 0.6 mm. This combination of cells forms a 10 mm unit cell that can be repeated to form the whole lattice. An example of this unit cell geometry is reported in Figure 4.12. From now on, this new geometry will be simply referred as Octet cell.

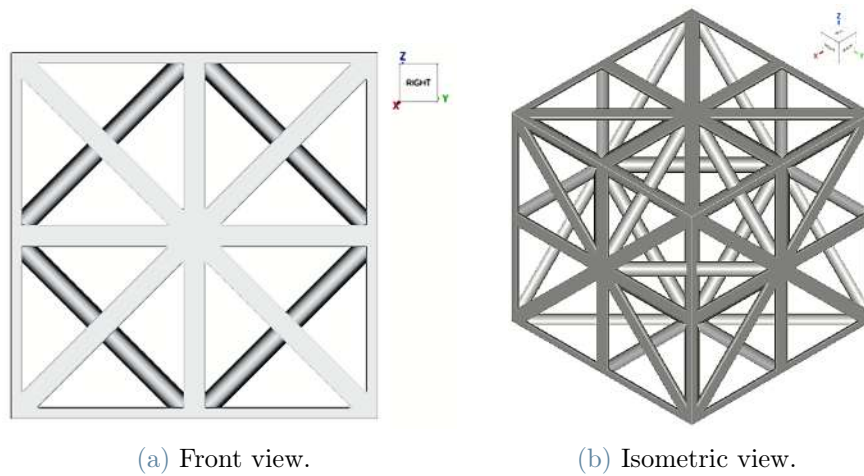


Figure 4.12: Octet unit cell.

Planar sector comparison with tetrahedral cells

Due to the high simulation complexity of the Octet cells, a first comparison with the tetrahedral cells have been made on a simpler planar sector to understand their performances and competitiveness. The models used for the simulations are reported in Figure 4.13. The Octet solid is composed of 3 cells in width, 2 in height and 10 in length. The tetrahedral cells solid is made of 4 cells in row, with the same dimensions and orientation to the flow seen in section 4.4.1. The bounding box occupied by the solid is 15 x 10 x 50 mm in both cases. The fluid domain crosses the cells sectors, leaving 5 mm of free flow before and after the cells. In this case, the fluid is forced to flow through the cells and cannot divert outside. The numerical modelling of the tetrahedral cells sectors follows the same procedure explained in section 4.4.1, while the Octet cells sector needs a slightly different

modelling technique. In this case, both solid and fluid domain have been modelled using nTopology and exported separately as STL files. They have been re-meshed separately using ICEM in Workbench. The criteria for a good mesh, in particular for the fluid one, are the same seen in section 4.2. Both meshes have been imported in Fluent solver and coupled through the common interface surface. A surface roughness of $10\text{ }\mu\text{m}$ is assigned to solid walls in contact with the air flow. The heat is provided from the bottom face with a constant temperature boundary condition set to 333 K. Heat will propagate by conduction through the struts and it will be rejected to air due to convection. Lateral and top faces are set as symmetries. The air enters the volume at 303 K with an inlet velocity of 10m/s.

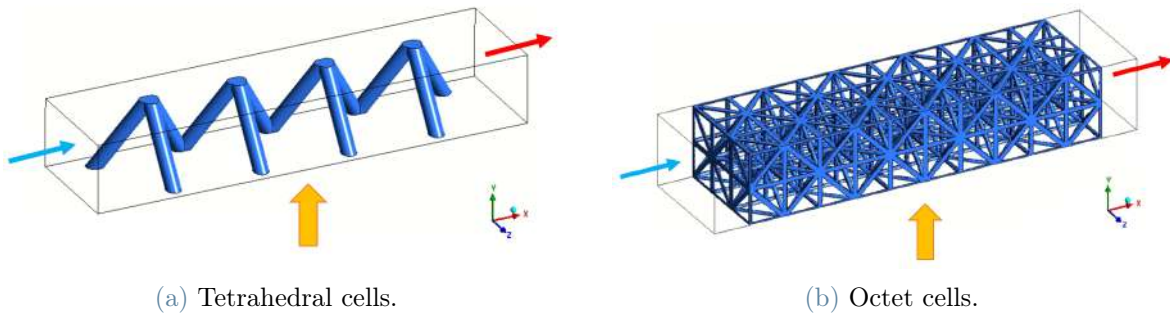


Figure 4.13: Domains for first Octet comparison.

The qualitative results of the first comparison of the two cells in terms of velocity and temperature with the same scale ranges are reported below. Figure 4.14a shows the velocity distributions in the mid place of the planar sector for the tetrahedral cells and for the Octet cells. The top map shows how the tetrahedral cells interact with the flow, accelerating it but with low fluid blockage. The bottom map instead shows how the higher flow restriction given by the Octet cells creates very fast flow lines through the cells. Figure 4.14b shows the temperature distributions on the solid - air interface for the tetrahedral cells and for the Octet cells. In the top map it is evident how the higher strut diameter of the tetrahedral cells allows an intense heat conduction to the cells top. In the bottom map instead the Octet cells reject quite soon the heat to the air flow, conduction is less effective due to the thinner struts.

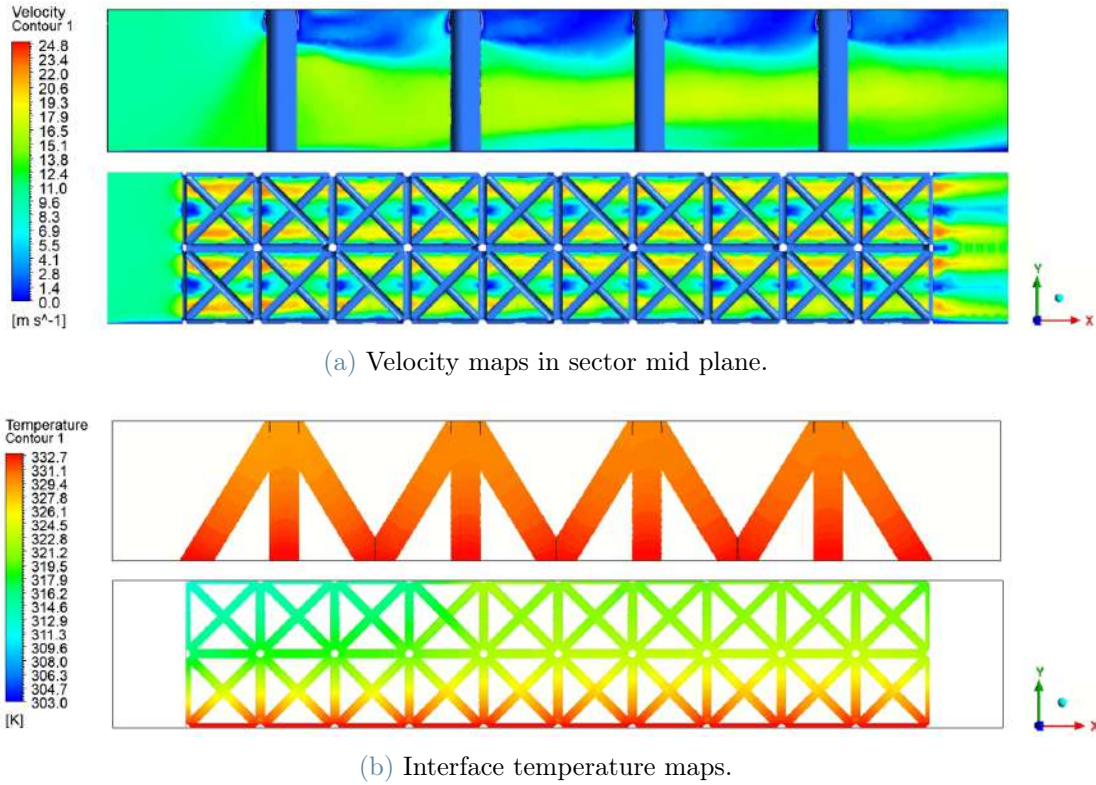


Figure 4.14: Qualitative comparison of Octet and tetrahedral cells planar sectors.

Quantitative results are reported in Table 4.1.

Model	T int [K]	\dot{q} int [W/m^2]	A int [m^2]	h [$\text{W}/\text{m}^2\text{K}$]	Q [W]	ΔP [Pa]
Tetra cells	331,9	4312,8	0,00165	148,95	7,10	121,05
Octet cells	324,4	3939,4	0,00409	184,03	16,12	573,70

Table 4.1: Performance comparison of Octet cells and tetrahedral cells planar sectors.

The first value in table is the temperature of solid - air interface. It depends on the combination of heat conduction from the bottom plate into the struts and heat convection from the struts to air flow. The tetrahedral cells struts have a much higher diameter and lower interface surface compared to Octet cells, which is beneficial for the conduction of heat till the cells top. Tetrahedral cells can then reach higher average temperature compared to Octet cells. This higher temperature is the driving force for a higher heat flux from the solid sector to the air flow. The convective heat transfer coefficient, expressing the effectiveness of stimulating convection from the solid to the fluid flow, is higher for the Octet cells since they largely promote fluid mixing and increase the interface surface. Moreover, since the Octet cells have an heat transfer area 2.5 times higher the one of tetrahedral

cells for the same occupied volume, the total thermal power rejected by the Octet cells to the air is much larger compared to tetrahedral cells. To complete this analysis, it is necessary to consider the pressure loss of the fluid flow. The higher flow blockage and perturbation given by the Octet cells translates in a pressure drop which is almost 5 times higher the one given by tetrahedral cells. A free flow not confined to pass through these channels would be highly diverted when interacting with the Octet structure and only a small fraction of the flow would actually cross through the cells. The lower mass flow in the structure would significantly decrease the thermal performance of the Octet cells. On the other hand, tetrahedral cells would allow more easily a faster flow through the cells due to lower flow blockage. The high potentiality in terms of thermal rejection of the Octet cells compared to the tetrahedral cells could then not be so evident when it is applied to the external part of the whole cooling jacket. In these simulations in fact air would be free to divert from the cells without forcibly pass through them, largely limiting their heat rejection capabilities.

Axial sector comparison with tetrahedral cells

Applying the Octet structure on the external of the whole cooling jacket would make the component extremely complicated and the computational demand would be too high to be analysed in its entirety. Hence, it has been decided to consider a single axial sector of the entire cooling jacket, obtained by cutting the jacket and the air domain with planes perpendicular to the motor axis and simulating only a central portion of the component. Unfortunately, a single axial sector will not be fully representative of the behaviour of the complete jacket since air movements are confined to be along flow direction, with minimal deflection along axial direction. Therefore, to compare the Octet cells axial sector with the tetrahedral cells model, it has been designed an axial sector also for the tetrahedral cells geometry. The two solid models used for the comparison are reported in Figure 4.15. The tetrahedral cells axial sector consists of a single row of cells while the Octet cells sector has 3 cubic cells in axial direction, 2 cubic cells in radial direction and 32 cubic cells along the sector circumference. The width of both jacket sectors is 15 mm. The volume infilled with lattice fins has the same dimensions in both cases. Notice that also the Octet cells solution needs a wing to divert the air flow to the rear cells.

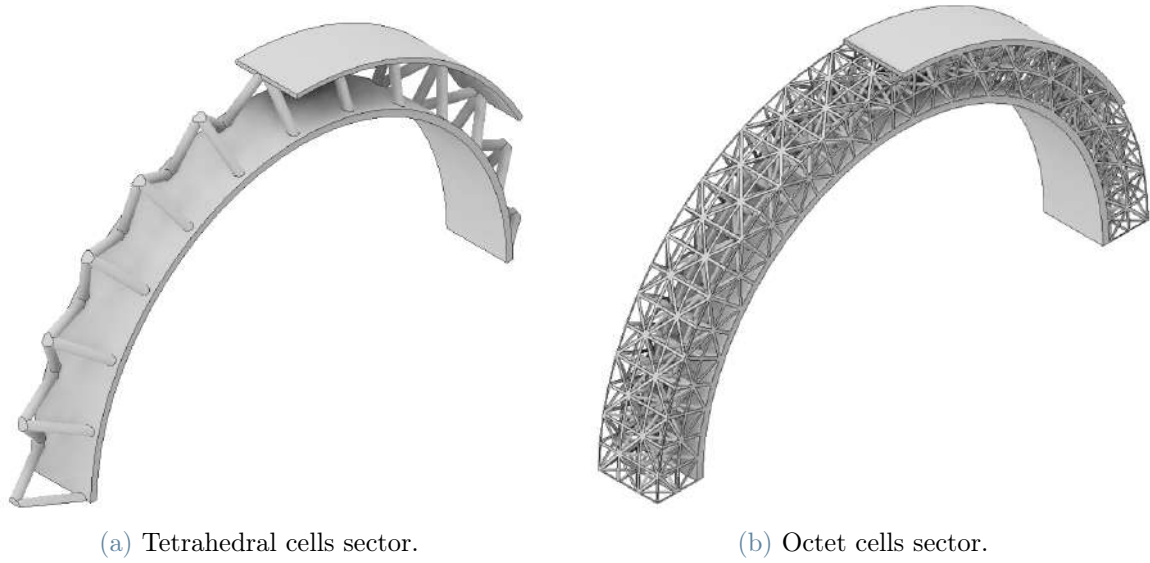
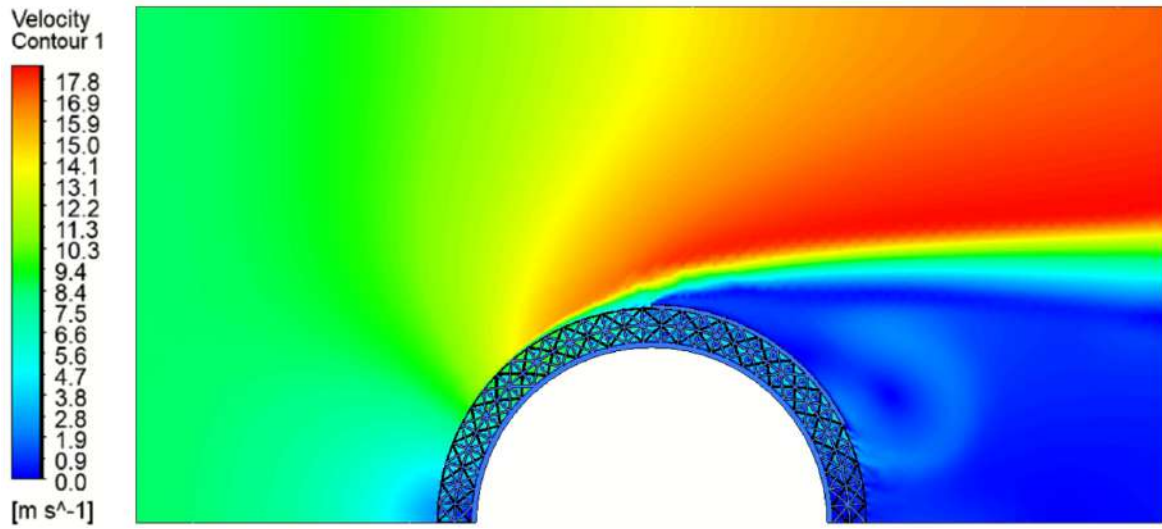


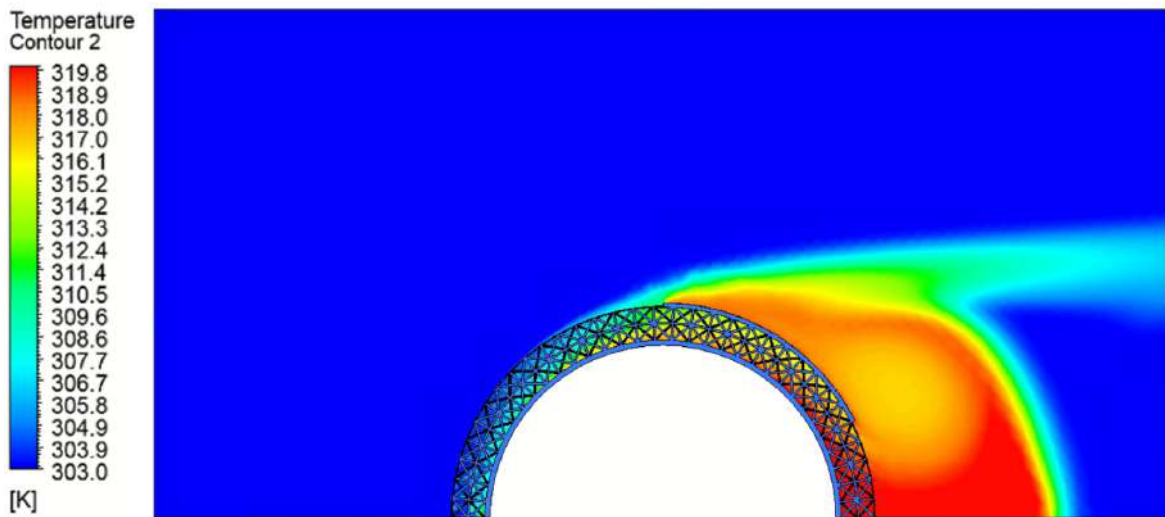
Figure 4.15: Cooling jacket sectors used for external fins comparison.

The modelling of the tetrahedral cells jacket axial sector follows the same procedure explained in section 4.4.1, while the modelling of the Octet axial sector is slightly different. Both solid and fluid domain have been modelled directly using Inventor and exported as independent STEP files. They have been meshed separately using ICEM in Workbench. As for the planar sector, both meshes have been imported in Fluent solver and coupled through the common interface surface. Lateral walls of solid and fluid domain have been set as symmetry since the axial sector simulates a central part of the cooling jacket. Radial symmetry has been imposed on the bottom walls and the top wall has been set as symmetry to avoid the no slip condition. The heat is introduced again from the solid - water interface which has been set at a constant temperature of 333 K. The unperturbed air flow enters the volume at 303 K. Both axial sectors models have been tested at 10 m/s inlet air velocity and results are reported below.

Figure 4.16 shows the velocity and temperature maps for 10 m/s air velocity on jacket with Octet cells fins and wing. They are plotted on the same scale ranges of tetrahedral cells maps in Figure 4.6 to allow a direct qualitative comparison. In the velocity map it is clear how the air flow has more obstruction to enter the Octet cells. Most of the air in fact diverts and accelerates outside the jacket. Only a portion is able to penetrate the Octet cells and interact with the rear part of the jacket. However, due to the strong interaction and perturbation between this limited air flow and the cells, the Octet cells solution offers high heat removal capabilities.



(a) Velocity map.



(b) Temperature map.

Figure 4.16: Velocity and temperature maps for 10 m/s air velocity on jacket with Octet cells fins and wing.

Quantitative results are summarized in Table 4.2.

Model	T int [K]	\dot{q} int [W/m ²]	A int [m ²]	h [W/m ² K]	Q [W]	Fins mass [g]
Tetra cells	330,936	2021,9	0,00689	72,38	223,05	99,20
Octet cells	326,844	1417,2	0,01490	59,44	337,81	111,42

Table 4.2: Performance comparison of Octet cells and tetrahedral cells sectors.

Initial considerations are similar compared to the shorter planar sectors seen before. The

average temperature of solid - air interface depends again on the combination of heat conduction from the shell into the struts and heat convection from the solid struts to the air. The higher strut diameter of the tetrahedral cells is beneficial for conduction of heat through the entire cell. This higher temperature, combined with a more consistent air flow through tetrahedral cells, is the driving force for a higher heat flux from the solid sector to the air flow. These considerations favour the tetrahedral cell in terms of convective heat transfer coefficient. In fact, for a fixed interface area, it has better convective heat transfer capabilities compared to the Octet cells solution. However, since the Octet cells have an heat transfer area more than twice the one of tetrahedral cells for the same occupied volume, the total thermal power rejected to environment is larger. This value of thermal power is an estimation of the amount of heat rejected by the whole model. It is calculated as the thermal power rejected by the single sector multiplied by 16, which is the amount of sectors needed to re-create the complete cooling jacket. Compared to results of the entire model obtained in section 4.4.1, the tetrahedral axial sector slightly underestimates the behaviour of the complete model. Even if the air flow is not forced to the lattice structure as for the planar sectors, the Octet cells still offer an advantage from the thermal management point of view. Lastly, even if the Octet cells solution would be heavier than the tetrahedral cells, it would still be 38.7% lighter than Dynamis fins solution.

To conclude, even if it was not possible to simulate the Octet structure on the complete cooling jacket model, the direct comparison between the Octet cells and the tetrahedral cells sectors shows the possible advantages of adopting this last solution for the external geometry of the cooling jacket.

4.4.3. Diamond cells

Geometry definition

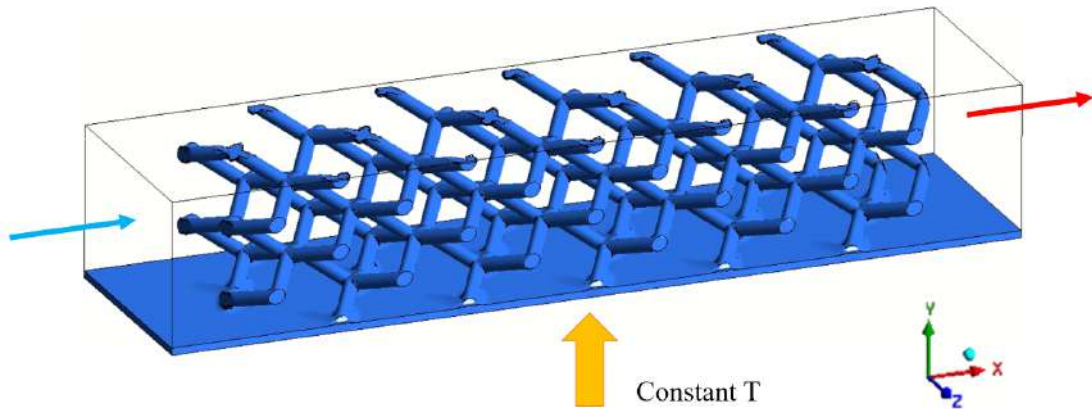
The idea now is to develop a new solution combining positive features from both the previous geometries. Referring to Figure 4.14, tetrahedral cells thicker struts promote heat conduction till the cells top, increasing average interface surface temperature and favouring heat flux from the solid body to the air flow. On the other hand, the Octet cells lattice structure highly increases heat transfer area, flow mixing and convection effectiveness.

The new solution keeps the idea of a proper lattice structure, having this time the Diamond geometry shown in Figure 1.12 as unit cell. The cells have been applied all around the external part of the cooling jacket, as it was done for both previous geometries in Figure

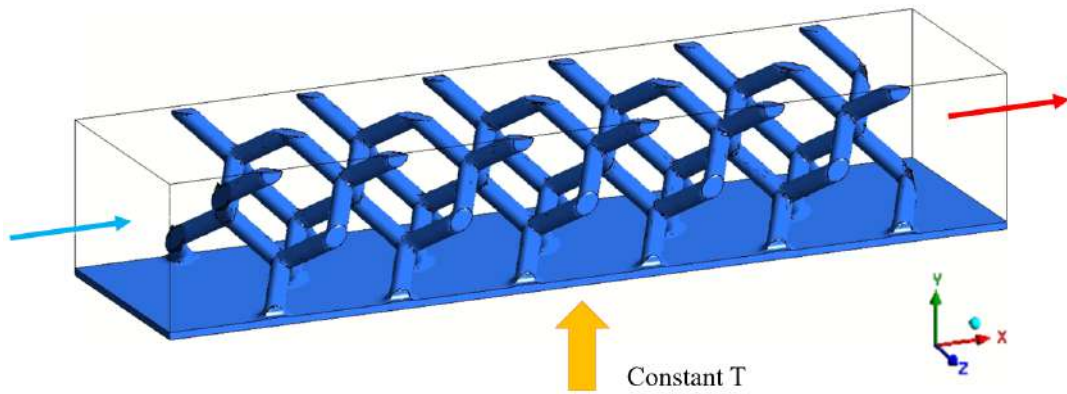
4.15. The total lattice height in radial direction is again 10 mm.

Planar sectors simulations

Due to computational complexity, the CFD studies of this new lattice structure have been performed on a short planar sector, representing a section of the externally applied lattice layer made planar. The sector has the same dimensions of that modelled for first Octet cells studies in section 4.4.2. Two different diamond cell dimensions have been designed using nTopology, meshed with Icem and studied with Ansys Fluent, following the same numerical set up procedure of the Octet cells sector explained in section 4.4.2. The first geometry involves a smaller cell, such that two equal cells are fitted in the 10 mm lattice structure layer around the component. It is identified as "5 mm Diamond cells". The second geometry applies a bigger cell, so to fit only one cell in the lattice layer. It is identified as "10 mm Diamond cells". Figure 4.17 represents both geometries computational domains, where the blue part is the solid aluminium material and the transparent volume defines the air domain. The yellow arrow indicates that heat is provided by the bottom planar face by setting a constant temperature boundary condition as before.



(a) 5 mm Diamond cells model.



(b) 10 mm Diamond cells model.

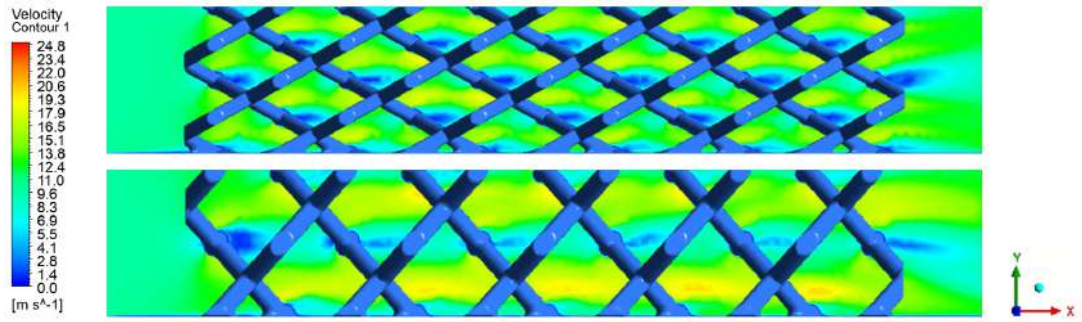
Figure 4.17: Domains for the Diamond cells analyses.

The relative density of both lattices, which determines the solution weight and influences overall performances, has been set equal to the one of Octet 5 mm cells solution. This new geometries will then have a mass very similar to the 5 mm Octet cells solution. Imposing a 7.3% relative density, the strut diameter is fixed for both solutions. The geometry involving one 10 mm cell in lattice thickness requires a strut diameter of 1.35 mm, while the solution with two 5 mm cells needs a strut diameter of 1 mm. Both single unit cells have been elongated along build direction to allow a cleaner air flow through the lattice and ease the manufacturing process. The build direction coincides again with the component axis, the Z axis in Figure 4.17.

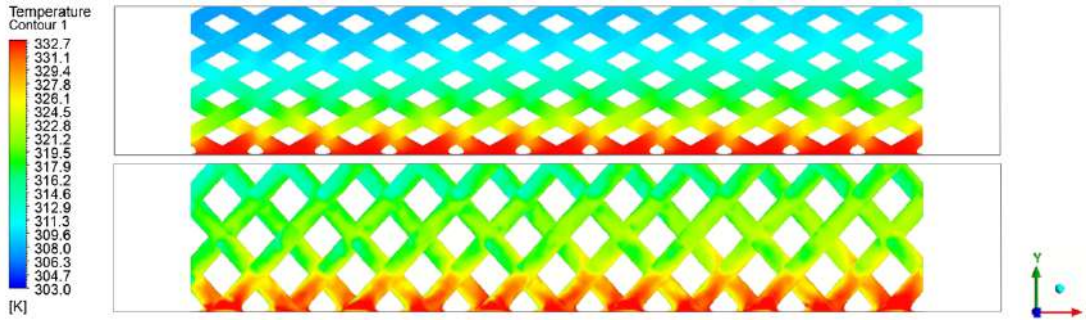
The CFD analyses have been set up in the same way as explained in section 4.4.2 for the Octet cells and tetrahedral cells planar sectors. Results have been analysed in the Post processing environment.

Results discussion and final comparison

Figure 4.18a shows the air velocity on the mid plane of the planar sector. The flow channels through the struts and accelerates, favouring convection heat transfer. Figure 4.18b shows the interface temperature of the two lattices. Both figures are in the same scale ranges of those in Figure 4.14 to allow a direct visual comparison with Octet cells and tetrahedral cells solutions.



(a) Velocity maps in sector mid plane.



(b) Interface temperature maps.

Figure 4.18: Qualitative comparison of the two diamond geometries planar sectors.

For clarity reasons, all the results for the investigated geometries in the planar sector are reported in Table 4.3.

Model	T int [K]	\dot{q} int [W/m^2]	A int [m^2]	h [$\text{W}/\text{m}^2\text{K}$]	Q [W]	ΔP [Pa]
Tetra cells	331,9	4312,8	0,00165	148,95	7,10	121,05
Octet cells	324,4	3939,4	0,00409	184,03	16,12	573,70
Diam. 5 mm	320,9	3927,2	0,00302	219,27	11,87	361,24
Diam. 10 mm	327,2	5522,4	0,00246	227,92	13,60	345,34

Table 4.3: Performance comparison of Diamond cells planar sectors.

The model "Diam. 5 mm" refers to the geometry presented in Figure 4.17a, while "Diam. 10 mm" refers to the geometry shown in Figure 4.17b. As discussed in section 4.4.2, the increase in strut diameter of the 10 mm diamond geometry is positive to have a good heat conduction through the lattice to the cells top. The improved conduction determines an higher interface surface temperature, which determines an higher surface heat flux \dot{q} from the component to the air flow. However, this solution leads to a decrease in total heat transfer area compared to the smaller cells of the 5 mm diamond solution, which is detrimental for total thermal power rejected. The convective heat transfer coefficient h , similar for the two diamond geometries, is higher compared to both tetrahedral unit cells and Octet cells results. The effectiveness of these geometries in promoting convection seems higher than previous solutions. The total thermal power rejected is slightly higher for the 10 mm diamond geometry. Regarding the sector pressure drop, it is important to remember that all these simulations on the planar sector consider an air flow confined to go through the lattice structure. In the real application, the ambient air flow that interacts with the lattice structure applied externally on the component is free to divert and only a fraction of it would actually enter and interact with the lattice structure. The sector pressure drop is an index of the ease for the air to enter and cross the planar sectors. Results are similar for both diamond geometries, showing a clear decrease compared to the Octet cells solution. This means that for the real application the air would enter more easily and in greater quantity in a diamond lattice structure compared to Octet cells structure. Total thermal power rejection to ambient highly depends also on the amount of air that interacts with the structure. The apparent advantage on thermal power rejected by Octet cells over the diamond cells could disappear in the real world application. From the point of view of additional weight, the lightest solution is the one involving tetrahedral cells. This geometry shows overall thermal performances comparable to Dynamis solution adopted in season 2019 - 2020, with a strong weight reduction of 45.6%. The remaining Octet a Diamond cells geometries are slightly heavier, but still 38.7% lighter than Dynamis fins solution.

In conclusion, diamond geometries offer a good compromise between heat transfer capabilities, lattice permeability to the air flow and lightness. These Diamond solutions appear to be interesting for the external component geometry.

4.5. Re-design for LPBF

The external geometry design stages until now did not systematically considered the manufacturability constraints imposed by LPBF process. These constraints, in particular the

45° critical angle and the maximum allowed overhang, could highly affect the lattice structure geometries and so their performances. The compliance with these manufacturability constraints have been verified importing and analysing all the lattice structures on Autodesk Netfabb. Netfabb is a software specific for AM applications which allows to study the imported geometry, to check its feasibility according to the desired build direction and to design support structures if needed.

The starting point of manufacturability constraints check is about the tetrahedral cells geometry presented in Figure 4.4 and reported in Figure 4.19a. These cells cannot be directly produced by LPBF without the addition of supports. In fact, if the build direction coincides with the axis of the component, the struts would exceed the 45° critical angle constraint presented in section 1.2.2. A possible cell re-design that follows manufacturability rules is reported in Figure 4.19b. In this representation, struts have been inclined to form a 45° angle with respect to the component axis, chosen as growth direction.

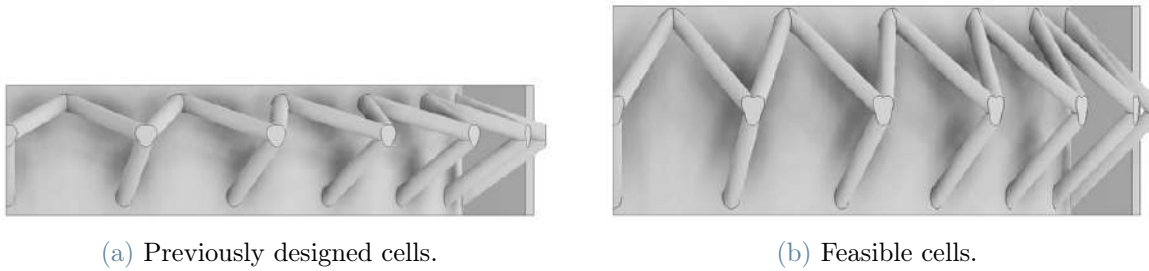


Figure 4.19: Manufacturability constraints for tetrahedral unit cells.

However, this new design would highly affect the overall geometry of the component since it would be possible to fit less cell rows along the axial direction of the part. The heat transfer surface area and interaction with the flow would be affected, leading to different thermal management performances.

The solution including Octet cells also needs re-design to be fully compliant with LPBF manufacturability constraints. Looking at Figure 4.12a, the only struts non compliant with manufacturability limits are the horizontal parts, those perpendicular to growth direction. In this case, the limiting factor is the maximum overhang that can be produced without the addition of supports. Supports would be extremely impractical in this case due to the complexity of removal from the single cells. The maximum overhang distance of horizontal parts depends on powder material, on process parameters and on the machine. In case of the Renishaw AM250 working station of Politecnico di Milano, a maximum suggested overhang for such thin struts is 3 mm to generally obtain good quality parts.

Cells would then need a redesign, lowering the cells edge from 5 to 3 mm but keeping the strut diameter to 600 μm . These two configuration are reported in Figure 4.20. The reported lattices are in the same scale to allow a direct qualitative comparison. The radial extension of the lattice structure on the external surface of the component was 10 mm for both tetrahedral cells and 5 mm Octet cells geometries. To keep a comparable lattice structure thickness around the component, the new Octet cells solution adopts 3 cells in height, leading to a lattice height of 9 mm.

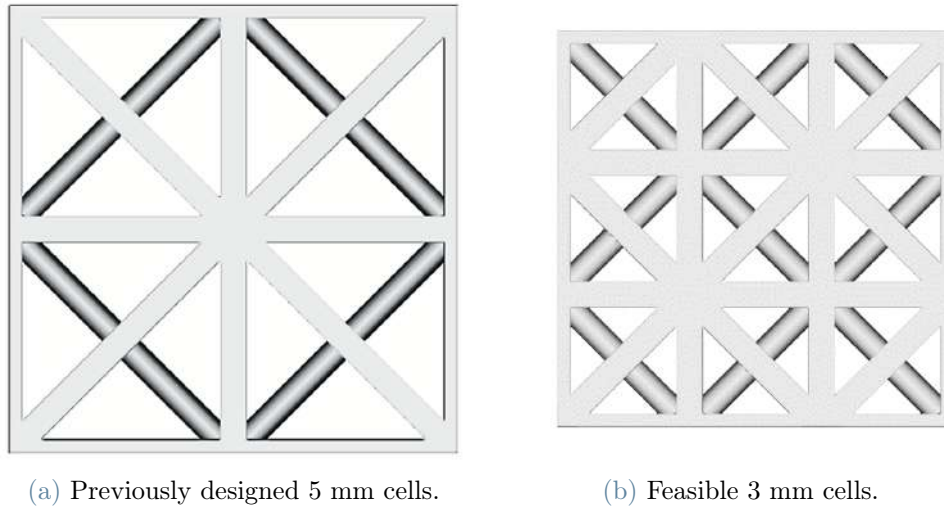


Figure 4.20: Manufacturability constraint for Octet unit cells.

It is evident how this change in cell dimension highly affects the lattice porosity. The initial value of relative density around 7.3% increases up to 18.4%. This leads to a drastic increase in component weight of 81.5%. Moreover, thermal performances would be affected as well since the air blockage of these less porous cells would be even higher than before. It would be more difficult for air to enter the lattice structure and reach the rear part of the component. Numerical results shown in Table 4.2 would be no more reliable.

Manufacturability constraints imposed a severe re-design to both previously studied geometries, which made them loose attractiveness in terms of thermal rejection capabilities and lightness. However, both Diamond lattice structures are already compliant with LPBF constraints and need no re-design. Their slightly elongated cells along build direction allow an easier manufacturing process since every strut is far from the 45° critical angle and no overhanging structure would be present. An example of a single 10 mm Diamond cell is reported in Figure 4.21.

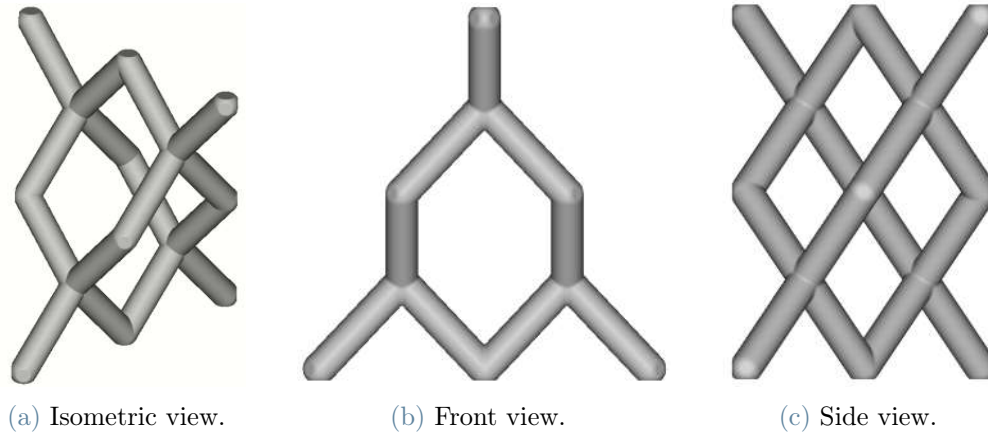


Figure 4.21: Single 10 mm elongated Diamond cell.

Having in mind these results and the considerations on manufacturability constraints, the most promising options for the external geometry of the cooling jacket are the two diamond cells lattice structures, which can be produced by LPBF without re-design.

4.6. Final component

The final component design is given by the combination of the best performing internal channel geometry and external fin arrangement. The most promising solutions emerged from this thesis work are the 2 mm empty channel geometry in helical configuration around motor axis for the internal part and the Diamond lattice structure with diverting wings for the external geometry. The 5 mm Diamond cells geometry has been preferred over the 10 mm Diamond cells since it is more in line with the concept of millimetric-scale cells lattice structure expressed in section 4.4.2.

The starting point of the final component modelling is the new Dynamis cooling jacket for season 2021 - 2022. A CAD version of the Team's final design where external fins have been removed is reported in Figure 4.22a. It consists of the cylindrical single shell, inlet and outlet water manifolds and a base flange to secure the cooling jacket to the motor block. An important difference compared to previous season component shown in Figure 2.1 is the arrangement of inlet and outlet water manifolds. The old inlet and outlet pipes required internal support structures to allow the production by LPBF since they extended perpendicular to the build direction, which coincided with component axial direction. These additional internal support structures needed to be removed by post-processing machining. The new version of the manifolds involves pipes aligned with growth direction, which are compliant with LPBF manufacturability constraints of critical

angle and maximum overhang and need no additional supports.

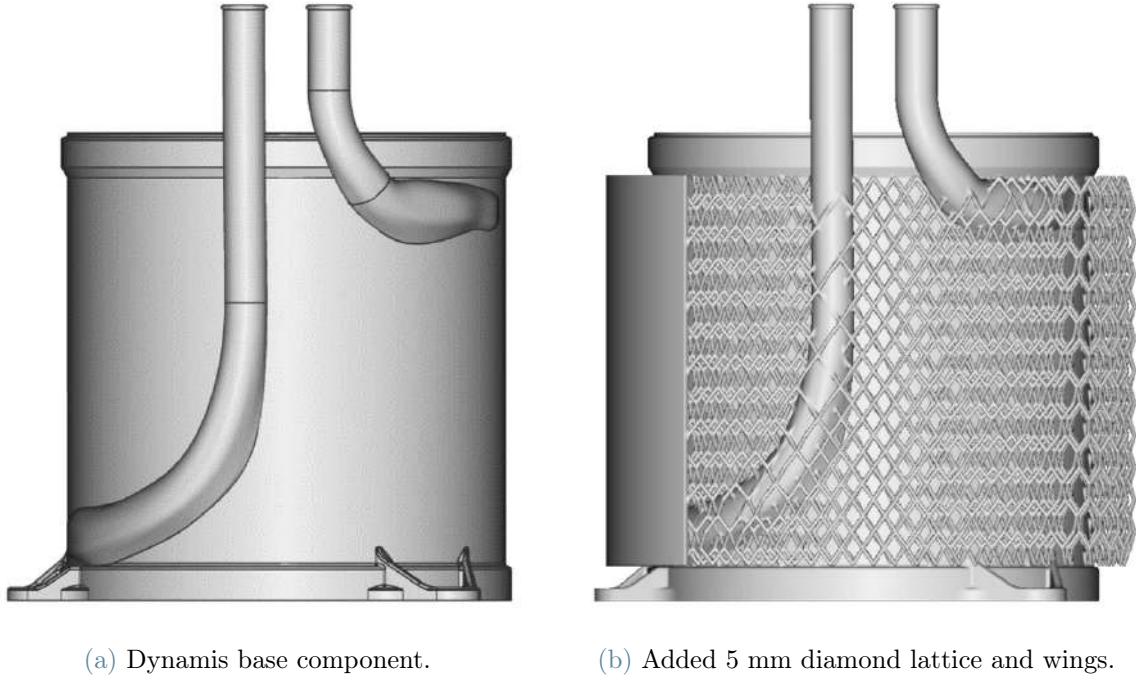
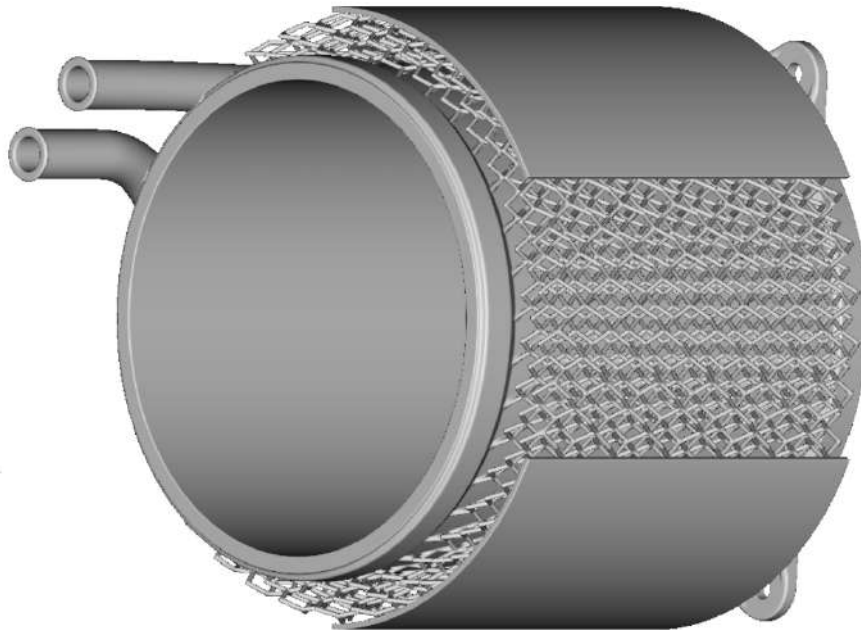
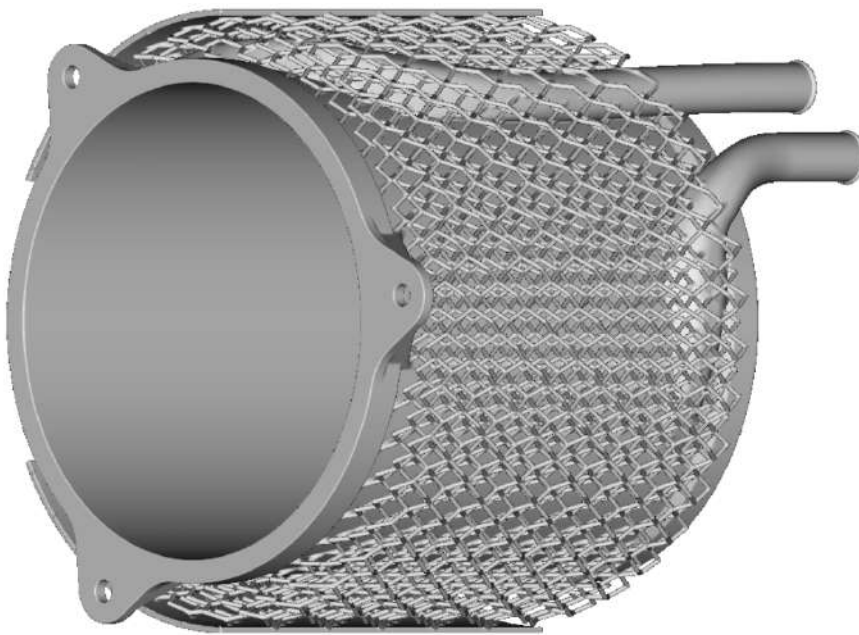


Figure 4.22: Integration of 5 mm cells Diamond lattice structure.

Figure 4.22b shows the integration of Diamond lattice structure as external fin system. In particular, the 5 mm diamond cells lattice and wings have been designed using nTopology and merged with the base component. The thickness of the lattice structure layer in radial direction around the component is 10 mm.



(a) Front view.



(b) Back view.

Figure 4.23: Final component views.

Figure 4.23 shows the final component in two different views. In the front view, the wings used to deflect air to the rear part of the component are clearly visible. They have been embedded on top of the lattice structure layer. In the back view, the base flange needed to secure the component to the motor block and the 5 mm Diamond cells lattice structure can be better appreciated. The internal geometry has been hidden as a matter of secrecy.

Figure 4.24 shows the side view of the component, interacting with the ambient air flow directed along the Z axis. Part of the air stream will penetrate in the lattice structure and divert to the rear part thanks to the additional wings. This deflected air stream will increase the thermal rejection effectiveness of the rear part of the component.



Figure 4.24: Final component side view.

5 | LPBF samples design

To understand and verify the processability of the externally applied Diamond structures studied in section 4.4.3, five different samples have been prepared for the LPBF process. Each sample was first created using nTopology. One of these samples only includes one diamond cell, elongated along the axial direction, to have a physical representation of the adopted cell. The cell is 15 mm high along build direction and 10 mm large along the other two direction. It is shown in Figure 5.1a. The other four modelled geometries refer to a round sector spacing 40° of the total component circumference. They are 15 mm high in axial direction, which coincides with the build direction. In particular, they consists of:

- 5 mm diamond cells geometry with a portion of the single shell on which they are embedded and a portion of the wing. It is reported in Figure 5.1b.
- 10 mm diamond cells geometry with a portion of the single shell on which they are embedded and a portion of the wing.
- 5 mm diamond cells geometry without the single shell portion.
- 10 mm diamond cells geometry without the single shell portion. It is reported in Figure 5.1c.

All the samples shown in Figure 5.2 share the same coordinate system, which has been reported only in Figure 5.1c. The Z axis, coinciding with component axis, is the build direction of this LPBF process.

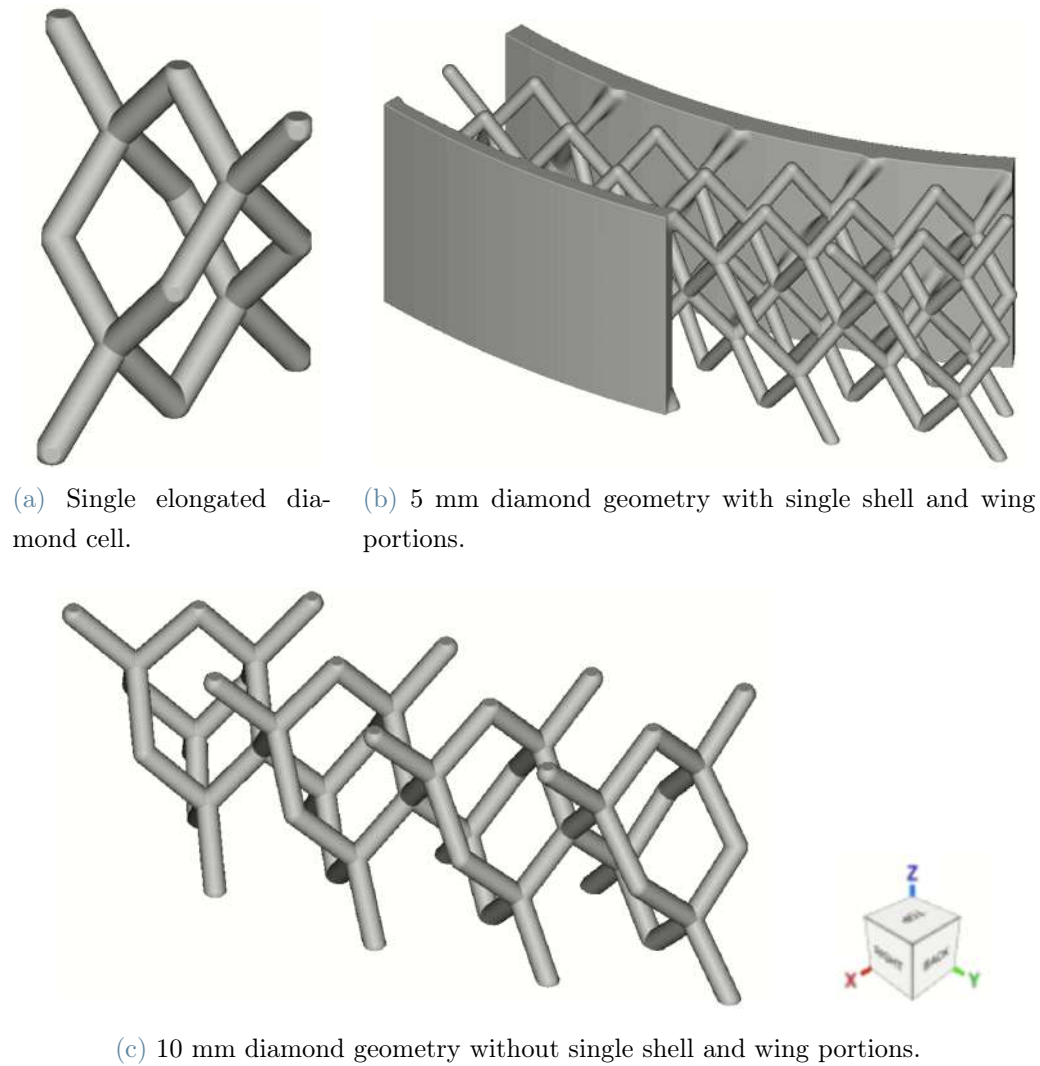
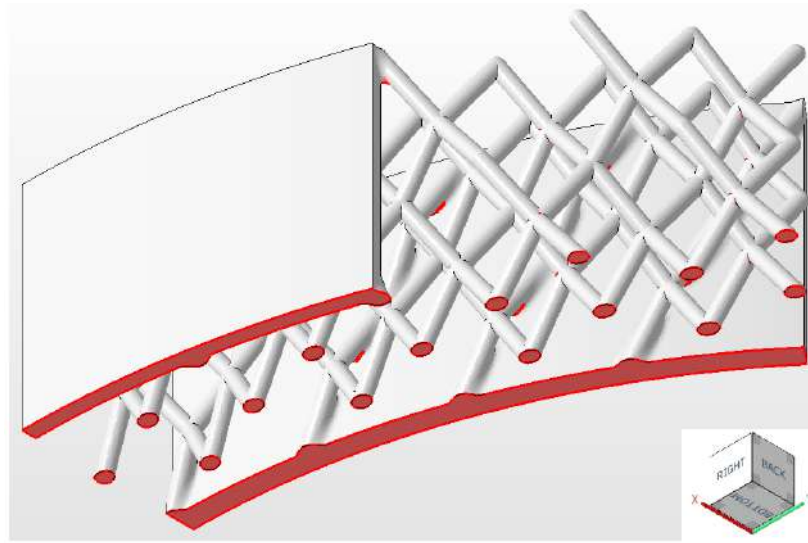


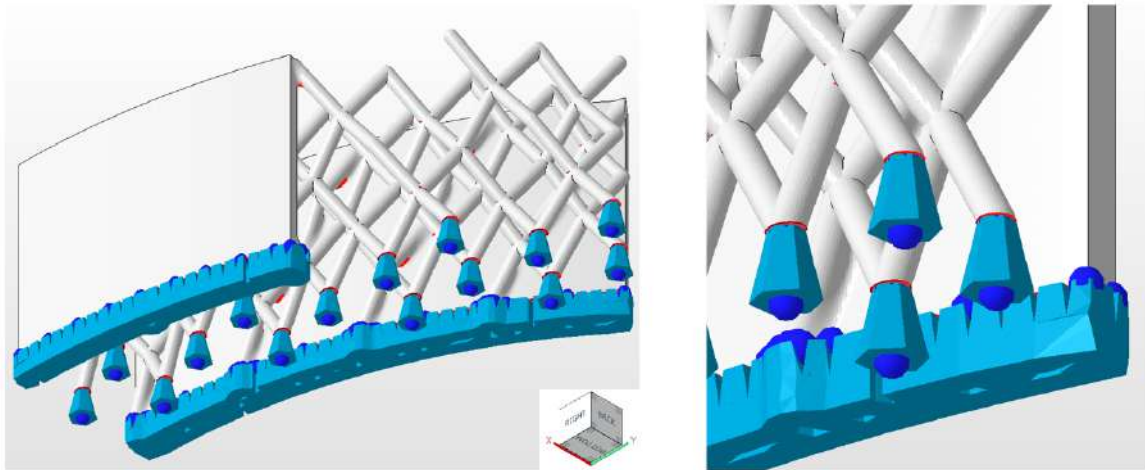
Figure 5.1: Diamond geometry samples for LPBF.

They have been meshed, exported as .stl file and imported on Netfabb. The geometries have been designed to be directly manufacturable, with no need for re-design or additional internal support structures difficult to remove.

First, the geometry is investigated to find possible inclined down-skin areas exceeding the 45° critical angle. The areas that need supports are highlighted in red by the software in the "Generate supports" environment. Figure 5.2a shows that, for the 5 mm diamond cells geometry with a portion of the single shell, only the planar bottom-facing surfaces need supports. No supports are needed inside the lattice structure. Figure 5.2b shows the modelled supports needed to produce the component. They will need to be removed in post-production to obtain the final part. Supports are finally merged to the solid imported part and exported as .stl, ready to be produced.



(a) Check for support need.



(b) Modelled supports.

Figure 5.2: Supports design for the 5 mm diamond cell geometry.

All the previously listed samples have been analysed in this way through Netfabb. For every part, supports have been added only on the planar bottom-facing surfaces, with no need for supports inside the lattice geometry.

5.1. Process parameters

The selection of proper process parameters, as studied in section 1.2, is necessary to obtain good quality of manufactured components. The optimal process parameters can strongly reduce part distortion, high surface roughness, non-complete fusion and adhesion of powder and the formation of hot cracks. A first guess of process parameters that should

guarantee good quality results for a continuous laser process are summarised in Table 5.1.

Process parameter	Value
Laser power	200 [W]
Scan speed	1000 [mm/s]
Layer thickness	25 [μm]
Hatch spacing	90 [μm]
Hatch angle	67° [rad]
Scanning pattern	Bi-directional

Table 5.1: LPBF process parameters.

Among these parameters, the hatch angle has not been mentioned yet. It indicates the angle difference between scanning directions of subsequent layers. Starting from a certain layer with a given laser scan direction, the following layer will have a scanning direction inclined 67° from the current one. This value has been found to give good layer by layer adhesion, structural strength and low porosity. The bi-directional scanning pattern indicates that adjacent scans in the same layer are parallel but are made in opposite directions, back and forth.

The optimization of these parameters would require time and many different tests, but would highly increase the overall quality of the final produced part.

6 | Conclusions and future developments

The objective of this thesis work has been the study of the behaviour of different strut-based lattice structures as a mean to enhance heat transfer capabilities of cooling jackets for in-wheel electric motors. A cooling jacket is a component of the vehicle cooling system. It envelops the motor, allowing a coolant fluid to flow on the external hot surface of the motor. The component is designed to be fabricated by Additive Manufacturing, hence following Laser Powder Bed Fusion manufacturability constraints. Initially, a research on the state of the art of strut-based lattice structures has been made to understand current solutions and performances of their applications in heat exchangers. The cooling jacket main design areas are the internal cooling channel for the coolant fluid and the external fins system. The internal cooling channel envelops the electric motor in an helical path around its axis. The coolant fluid flows directly in contact with the hot motor surface and subtracts the generated heat. Different channel thicknesses with embedded spherical dimples and tetrahedral unit cells have been analysed using CFD analyses and compared in terms of pressure loss and convective heat transfer coefficient. The overall best configuration is a 2 mm high empty water channel. The external fins system provides an additional heat dissipation to ambient air, useful to reduce the workload of the whole cooling system. The idea was to take advantage of lattice structure porosity and, with an additional wing, divert air on the rear part of the component to increase heat transfer effectiveness. Starting from a cooling jacket with no fins, four different lattice geometries have been tested at different air speed and compared to Dynamis rectangular fins results. The analysed geometries involve tetrahedral cells, octet cells and two diamond structures with 5 mm and 10 mm cells. Due to computational complexity, only the simpler tetrahedral cells have been tested on the complete jacket model, showing slightly lower thermal performances compared to Dynamis but with a significant fins weight loss of 45.6%. The other lattice structures were compared as planar sectors due to excessive computational requirements of complete jacket simulations. These new geometries show an increase in thermal performances compared to tetrahedral cells, but a lower permeability to the am-

bient air flow. Simulations on an axial sector of the jacket, which results are reported in Table 4.2, were possible only for the tetrahedral and Octet cell geometries. As expected from the planar sector comparison, the Octet cell geometry has higher thermal rejection performances than the Tetrahedral cells. However, the increase in thermal power rejected is not as evident as for the planar sectors results in Table 4.1. In fact, the axial sector simulations take into account the real lattice permeability since the air is free to divert from the flow-blocking lattice structure. Considering manufacturability constraints, the tetrahedral and octet cell geometries needed severe re-design and lost part of their attractiveness in terms of additional weight and varied performances. The two diamond geometries instead were compliant with LPBF process constraints and could be directly manufactured without re-design. Both 5 mm and 10 mm cells diamond geometries have good thermal rejection performances, flow permeability and lightness. The 5 mm cells diamond lattice structure was then selected for the external fins system. A model of the final component with the external diamond lattice structure layer and deflecting wing is reported in Figure 4.23. LPBF processability of the external lattice structure has been investigated by modelling and analysing different samples involving the diamond geometry.

Further developments of this work can be made on the simulation of more realistic working conditions for the octet and diamond cells by modelling the entire cooling jacket. The evaluations of the complete jacket performances will be more meaningful for a complete comparison with Dynamis results. Cell dimensions and relative density optimization can be performed to further increase performances and save more weight. Having the overall best geometry, it will be possible to design and manufacture the final component by LPBF.

Bibliography

- [1] Bonavita Matteo. Design of an innovative water jacket for formula sae electric in-wheel motors.
- [2] Junkui Huang, Shervin Shoai Naini, Richard Miller, Denise Rizzo, Katie Sebeck, Scott Shurin, and John Wagner. A hybrid electric vehicle motor cooling system—design, model, and control. 68(5):4467–4478.
- [3] Peixin Liang, Feng Chai, Ke Shen, and Weiguo Liu. Water jacket and slot optimization of a water-cooling permanent magnet synchronous in-wheel motor. 57(3):2431–2439.
- [4] Tobias Maconachie, Martin Leary, Bill Lozanovski, Xuezhe Zhang, Ma Qian, Omar Faruque, and Milan Brandt. SLM lattice structures: Properties, performance, applications and challenges. 183:108137.
- [5] Xing Zhang, Christopher J. Yocom, Bo Mao, and Yiliang Liao. Microstructure evolution during selective laser melting of metallic materials: A review. 31(3):031201.
- [6] Prashanth Konda Gokuldoss, Sri Kolla, and Jürgen Eckert. Additive manufacturing processes: Selective laser melting, electron beam melting and binder jetting—selection guidelines. 10(6):672.
- [7] Alexander Großmann, Julian Gosmann, and Christian Mittelstedt. Lightweight lattice structures in selective laser melting: Design, fabrication and mechanical properties. 766:138356.
- [8] Wei Pei, Wei Zhengying, Chen Zhen, Li Junfeng, Zhang Shuzhe, and Du Jun. Numerical simulation and parametric analysis of selective laser melting process of AlSi10mg powder. 123(8):540.
- [9] Zhonghua Li, David Zhengwen Zhang, Peng Dong, and Ibrahim Kucukkoc. A lightweight and support-free design method for selective laser melting. 90(9):2943–2953.

- [10] Di Wang, Yongqiang Yang, Ziheng Yi, and Xubin Su. Research on the fabricating quality optimization of the overhanging surface in SLM process. 65(9):1471–1484.
- [11] Di Wang, Yongqiang Yang, Ruicheng Liu, Dongming Xiao, and Jianfeng Sun. Study on the designing rules and processability of porous structure based on selective laser melting (SLM). 213(10):1734–1742.
- [12] Jingchao Jiang, Xun Xu, and Jonathan Stringer. Support structures for additive manufacturing: A review. 2(4):64.
- [13] Cassiopée Galy, Emilie Le Guen, Eric Lacoste, and Corinne Arvieu. Main defects observed in aluminum alloy parts produced by SLM: From causes to consequences. 22:165–175.
- [14] E.O. Olakanmi, R.F. Cochrane, and K.W. Dalgarno. A review on selective laser sintering/melting (SLS/SLM) of aluminium alloy powders: Processing, microstructure, and properties. 74:401–477.
- [15] Jinliang Zhang, Bo Song, Qingsong Wei, Dave Bourell, and Yusheng Shi. A review of selective laser melting of aluminum alloys: Processing, microstructure, property and developing trends. 35(2):270–284.
- [16] Pengda Niu, Ruidi Li, Shuya Zhu, Minbo Wang, Chao Chen, and Tiechui Yuan. Hot cracking, crystal orientation and compressive strength of an equimolar CoCrFeMnNi high-entropy alloy printed by selective laser melting. 127:106147.
- [17] A. Iturrioz, E. Gil, M. M. Petite, F. Garciandia, A. M. Mancisidor, and M. San Sebastian. Selective laser melting of AlSi10Mg alloy: influence of heat treatment condition on mechanical properties and microstructure. 62(4):885–892.
- [18] Inderjot Kaur and Prashant Singh. State-of-the-art in heat exchanger additive manufacturing. 178:121600.
- [19] Curtis K. Stimpson, Jacob C. Snyder, Karen A. Thole, and Dominic Mongillo. Roughness effects on flow and heat transfer for additively manufactured channels. 138(5):051008.
- [20] Tabish Alam and Man-Hoe Kim. A comprehensive review on single phase heat transfer enhancement techniques in heat exchanger applications. 81:813–839.
- [21] P. M. Ligrani, M. M. Oliveira, and T. Blaskovich. Comparison of heat transfer augmentation techniques. 41(3):337–362.
- [22] Beibei Shen, Yang Li, Hongbin Yan, Sandra K.S. Boetcher, and Gongnan Xie. Heat

- transfer enhancement of wedge-shaped channels by replacing pin fins with kagome lattice structures. 141:88–101.
- [23] Natthaporn Kaewchoothong, Kittinan Maliwan, Kenichiro Takeishi, and Chayut Nuntadusit. Effect of inclined ribs on heat transfer coefficient in stationary square channel. 7(6):344–350.
- [24] Gazi I. Mahmood, Mounir Z. Sabbagh, and Phillip M. Ligrani. Heat transfer in a channel with dimples and protrusions on opposite walls. 15(3):275–283.
- [25] Hamidreza Rastan, Amir Abdi, Bejan Hamawandi, Monika Ignatowicz, Josua P. Meyer, and Björn Palm. Heat transfer study of enhanced additively manufactured minichannel heat exchangers. 161:120271.
- [26] John Banhart. Manufacturing routes for metallic foams. 52(12):22–27.
- [27] David P. Haack, Kenneth R. Butcher, T. Kim, and T. J. Lu. Novel lightweight metal foam heat exchangers. In *Process Industries*, pages 141–147. American Society of Mechanical Engineers.
- [28] Rong Wang, Jianzhong Shang, Xin Li, Zirong Luo, and Wei Wu. Vibration and damping characteristics of 3d printed kagome lattice with viscoelastic material filling. 8(1):9604.
- [29] T Kim, H.P Hodson, and T.J Lu. Fluid-flow and endwall heat-transfer characteristics of an ultralight lattice-frame material. 47(6):1129–1140.
- [30] T. Kim, H.P. Hodson, and T.J. Lu. Contribution of vortex structures and flow separation to local and overall pressure and heat transfer characteristics in an ultralightweight lattice material. 48(19):4243–4264.
- [31] T Kim, H P Hodson, and T J Lu. Pressure loss and heat transfer mechanisms in a lattice-frame structured heat exchanger. 218(11):1321–1336.
- [32] T. Kim, C.Y. Zhao, T.J. Lu, and H.P. Hodson. Convective heat dissipation with lattice-frame materials. 36(8):767–780.
- [33] J. Tian, T. Kim, T.J. Lu, H.P. Hodson, D.T. Queheillalt, D.J. Sypeck, and H.N.G. Wadley. The effects of topology upon fluid-flow and heat-transfer within cellular copper structures. 47(14):3171–3186.
- [34] Inderjot Kaur and Prashant Singh. Critical evaluation of additively manufactured metal lattices for viability in advanced heat exchangers. 168:120858.
- [35] M.F Ashby. The properties of foams and lattices. 364(1838):15–30.

List of Figures

1	Dynamis cooling jacket for season 2019-2020 mounted on front left motor. .	2
1.1	Schematic representation of cooling circuit.	5
1.2	Velocity streamlines of the circumferential (left) and axial (right) water jackets [3].	6
1.3	LPBF process [5].	8
1.4	Effect of laser power and scan speed on lattice structure [7].	9
1.5	Hatch spacing of adjacent scan tracks.	9
1.6	Support structures in LPBF.	11
1.7	Geometrical discrepancies between desired and produced geometry. . . .	12
1.8	Staircase effect in LPBF.	13
1.9	Examples of metallurgical defects.	14
1.10	Examples of turbulence promoters.	16
1.11	Winglets in a narrow channel [25]	17
1.12	Strut-based lattice frame material.	18
1.13	Tetrahedral lattice frame material. [29]	19
1.14	Vortex structures around a cell. [30]	19
1.15	Anisotropy of the tetrahedral cell. [29]	20
1.16	Performance chart of different heat dissipation media [33].	21
2.1	2019 - 2020 design of Dynamis cooling jacket.	23
2.2	Conceptual map of studied solutions.	24
3.1	Model of the curved empty channel with 4.5 mm of water.	26
3.2	Model of the planar empty channel with 4.5 mm of water.	29
3.3	Performances trend for empty channel having different thicknesses.	31
3.4	Geometry of sectors with 4 mm dimples.	33
3.5	Influence of dimple diameter in 4.5 mm channel.	34
3.6	Water velocity profile in correspondence of dimples.	34
3.7	Effect of dimple diameter on performances.	35
3.8	Influence of dimples on temperature map.	36

3.9	Comparison of empty channel and dimple channel	38
3.10	3 mm cells geometries in 4.5 mm channel.	40
3.11	2 mm cells geometries in 3 mm channel.	41
3.12	Influence of 3 cells rows on motor surface temperature map.	42
3.13	Comparison of empty channel and 3 cells rows geometry.	43
3.14	Motor surface temperature maps for the 3 mm high cells geometries.	44
3.15	Water velocity profile in the middle of the channel for the 3 mm high cells configurations.	45
3.16	Motor surface temperature maps for the 2 mm high cell geometries.	46
3.17	Comparison of internal water channel geometries.	47
3.18	Re-design of internal cooling channel helical wall.	48
4.1	Numerical domains of jacket with no external fins.	52
4.2	Performances of jacket with no fins at different air velocities.	55
4.3	Velocity and temperature maps for 10 m/s air velocity on jacket with no fins.	56
4.4	Tetrahedral cells fins with wing.	58
4.5	Performance comparison between tetrahedral cells and smooth jacket.	59
4.6	Velocity and temperature maps for 10 m/s air velocity on jacket with tetra- hedral cells fins and wing.	60
4.7	Pressure map on interface.	61
4.8	Temperature distribution in the solid.	62
4.9	Boundary conditions for the fluid mechanic analysis.	62
4.10	Von Mises stress of the tetrahedral cell cooling jacket.	63
4.11	Axial stress of the tetrahedral cell cooling jacket.	64
4.12	Octet unit cell.	65
4.13	Domains for first Octet comparison.	66
4.14	Qualitative comparison of Octet and tetrahedral cells planar sectors.	67
4.15	Cooling jacket sectors used for external fins comparison.	69
4.16	Velocity and temperature maps for 10 m/s air velocity on jacket with Octet cells fins and wing.	70
4.17	Domains for the Diamond cells analyses.	73
4.18	Qualitative comparison of the two diamond geometries planar sectors.	74
4.19	Manufacturability constraints for tetrahedral unit cells.	76
4.20	Manufacturability constraint for Octet unit cells.	77
4.21	Single 10 mm elongated Diamond cell.	78
4.22	Integration of 5 mm cells Diamond lattice structure.	79

	List of Figures	95
4.23	Final component views.	80
4.24	Final component side view.	81
5.1	Diamond geometry samples for LPBF.	84
5.2	Supports design for the 5 mm diamond cell geometry.	85

List of Tables

1.1	Mechanical properties of Aluminium alloy.	15
3.1	Comparison of 3 mm curved and planar empty sectors.	29
3.2	Empty channel thickness effect.	30
3.3	Performances of channel with alternated dimples.	37
3.4	Performances of 3 cells rows geometry.	42
3.5	Comparison of 3 mm high cells geometries in 4.5 mm high water channel. .	45
3.6	Comparison of 3 mm high water channel with 2 mm high cells geometries.	46
4.1	Performance comparison of Octet cells and tetrahedral cells planar sectors.	67
4.2	Performance comparison of Octet cells and tetrahedral cells sectors. . . .	70
4.3	Performance comparison of Diamond cells planar sectors.	74
5.1	LPBF process parameters.	86

Acknowledgements

I would like to thank professors Foletti and Demir for the precious teachings and availability. Many thanks also to Fabio and Giovanni for the valuable advices and support.

